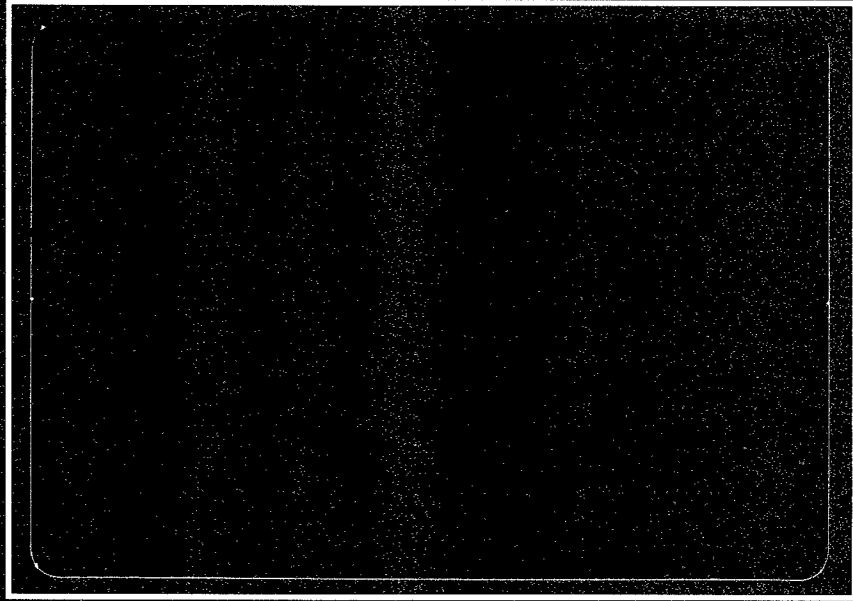
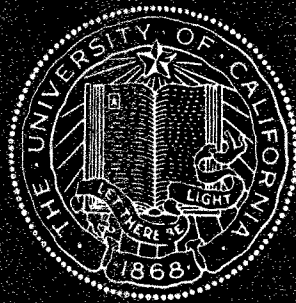


# Electrical and Computer Engineering



TECHNICAL REPORT



UNIVERSITY OF CALIFORNIA  
/ SANTA BARBARA, CA 93106

# **Research in Free-Space Interconnects Using Micro-Cavity Lasers**

Final Technical Report  
7/15/96 to 1/14/00

PI - L.A. Coldren

ECE Technical Report # 00-07

Air Force Office of Scientific Research  
Contract No. F49620-96-1-0354

**DISTRIBUTION STATEMENT A**  
Approved for Public Release  
Distribution Unlimited

Department of Electrical and Computer Engineering  
University of California at Santa Barbara, CA 93106-9560

20000627 111

RESEARCH (AFOSR)  
NOTICE OF TRANSMITTAL TO DTIC. THIS  
TECHNICAL REPORT HAS BEEN REVIEWED  
AND IS APPROVED FOR PUBLIC RELEASE  
IWA AFR 190-12. DISTRIBUTION IS  
UNLIMITED.  
YONNE MASON  
STINFO BRANCH MANAGER

**DTIC QUALITY INSPECTED 4**

## REPORT DOCUMENTATION PAGE

AFRL-SR-BL-TR-00-

Public reporting burden for this collection of information is estimated to average 1 hour per response, in gathering and maintaining the data needed, and completing and reviewing the collection of information. collection of information, including suggestions for reducing this burden, to Washington Headquarters S Davis Highway, Suite 1204, Arlington, VA 22202-4302, and to the Office of Management and Budget.

sources,  
ict of this  
Jefferson  
J.

0233

1. AGENCY USE ONLY (Leave blank)		2. REPORT DATE		3. REPORT TYPE AND DATES COVERED 15 Jul 96 to 14 Jan 00 Final	
4. TITLE AND SUBTITLE (ASSERT 96) RESEARCH IN FREE-SPACE INTERCONNECTS USING MICROCAVITY LASERS				5. FUNDING NUMBERS 61103D 3484/'TS	
6. AUTHOR(S) Professor Coldren					
7. PERFORMING ORGANIZATION NAME(S) AND ADDRESS(ES) Univ of California Cheadle Hall Santa Barbara CA 93106-6150				8. PERFORMING ORGANIZATION REPORT NUMBER	
9. SPONSORING/MONITORING AGENCY NAME(S) AND ADDRESS(ES) AFOSR/NE 801 North Randolph Street Rm 732 Arlington, VA 22203-1977				10. SPONSORING/MONITORING AGENCY REPORT NUMBER  F49620-96-1-0354	
11. SUPPLEMENTARY NOTES					
12a. DISTRIBUTION AVAILABILITY STATEMENT APPROVAL FOR PUBLIC RELEASED; DISTRIBUTION UNLIMITED				12b. DISTRIBUTION CODE	
13. ABSTRACT (Maximum 200 words)  With the end of the ASSERT program drawing near the focus of the effort has involved archiving the accomplishments of this work in the technical literature. This report will draw on the well documented results found in the technical literature.					
14. SUBJECT TERMS				15. NUMBER OF PAGES	
				16. PRICE CODE	
17. SECURITY CLASSIFICATION OF REPORT  UNCLASSIFIED		18. SECURITY CLASSIFICATION OF THIS PAGE  UNCLASSIFIED		19. SECURITY CLASSIFICATION OF ABSTRACT  UNCLASSIFIED	
				20. LIMITATION OF ABSTRACT  UL	

**Research in Free-Space Interconnects using Microcavity Lasers**

AFOSR Grant No. F49620-96-1-0354

Professor Larry A. Coldren, P. I.

Progress from July 15, 1996 to January 14, 2000

University of California, Santa Barbara  
Electrical and Computer Engineering Department  
Santa Barbara, CA 93106

ph: (805) 893-4486  
fax: (805) 893-4500  
e-mail: [coldren@ece.ucsb.edu](mailto:coldren@ece.ucsb.edu)

**Objective:**

The development of vertical cavity lasers (VCL) for the application to free-space interconnects has been proposed. The need for such free-space interconnects arises from the demand for high-speed data transmission between parallel signal planes.

Conventional methods for accomplishing high-speed data transmission suffers from the high power required to drive the transmitter laser array, and the lack of a 2-dimensional geometry leads to scalability problems for an in-plane laser array. In order to keep the laser power consumption low the threshold current of the lasers should be less than 100  $\mu$ A. Furthermore, the density of transmission elements must be increased in order to increase the transmission bandwidth.

In order to reduce the power requirement of the lasers, the size of the laser must be reduced. Unfortunately, several problems arise which prohibit the ideal scaling of the VCL size to small dimensions, these being, optical scattering loss and carrier diffusion loss. The optical and carrier based loss mechanisms can be addressed and the ideal VCL scaling can be approached. Through novel VCL design and processing, loss mechanisms can be reduced and the efficiency of the of the device can be greatly increased. This is essential for the application to VCL based interconnects.

The VCL is ideal for the application to free-space interconnects due to the natural 2-dimensional array formation. Furthermore, the VCL emission wavelength can be tailored to allow for wavelength division multiplexing (WDM) type transmission which will greatly increase the transmission bandwidth.

**Status of Effort:**

With the end of the AASERT program drawing near the focus of the effort has involved archiving the accomplishments of this work in the technical literature. With this in mind, this report will draw on the well documented results found in the technical literature. Four full length technical papers are included and referenced as appendices 1-4. The balance of this report will introduce the results of each of the included technical papers.

The first appendix involves the application of novel VCL design and processing achieve scaleable VCLs. That is, to reduce the size of the VCL to reduce power consumption and achieve dense 2-dimensional arrays. In order to achieve such small VCL dimensions it is necessary to eliminate carrier diffusion in the active region. A novel quantum well intermixing method has been successful in fabricating AlGaAs-GaAs VCLs. The goal is to achieve 100 meV of confinement in InGaAs-GaAs active regions while simultaneously adhering to a design that eliminates size-dependent optical losses and current spreading. Achieving this goal should result in significant improvement in the threshold current and efficiencies since the majority of the threshold currents a small VCL is lost to carrier diffusion.

The second appendix investigates the application of a novel multiple-wavelength optical data link. The link utilizes a monolithically integrated multiple-wavelength VCL array and a narrow-band resonant-cavity photodetector array to transmit multiple channels of information simultaneously. A detailed analysis on wavelength tuning and threshold characteristics of different laser cavity designs is presented. On the receiver part, both Schottky and p-i-n photodetectors with a single- or coupled-cavity structure are discussed. A novel p-i-n resonant-cavity photodetector design with a partially oxidized front mirror for linewidth control is proposed. Moreover, preliminary measurements of the optical link utilizing the multiple-wavelength VCL array and photodetector array have been performed.

Appendix three outlines a novel post growth processing technique to tune the cavity of the VCL thereby controlling the wavelength. The technique involves the combined lateral-vertical oxidation of AlGaAs as a means of tuning the resonant wavelength of the semiconductor microcavity after the epitaxial growth. It is shown that this technique can provide arrays with a wavelength spread equal to the cavity's free spectral range with a single postgrowth processing step. Design issues for multiple-wavelength VCL arrays using this postgrowth tuning technique are discussed. Experimental results are presented on arrays with a 48-nm lasing span around 970 nm are included.

The fourth appendix involves the crosstalk associated with multiple-wavelength VCL arrays under RF modulation. These arrays consist of eight bottom-emitting VCLs arranged with a "pie"-like configuration within a 60- $\mu\text{m}$  diameter circle with a 3- $\mu\text{m}$  spacing. The crosstalk is minimized by flip-chip mounting the array and introducing a proper bias condition. The crosstalk observed in the adjacent VCLs is less than -40 dB at the modulation frequency below 700 MHz and increases at 20 dB/decade above this frequency when both VCLs are biased at 5 mA.

## **Appendix 1**

# Interdiffused Quantum Wells for Lateral Carrier Confinement in VCSEL's

Ryan L. Naone, *Member, IEEE*, Philip D. Floyd, *Member, IEEE*, D. Bruce Young,  
Eric R. Hegblom, *Member, IEEE*, Timothy A. Strand,  
and Larry A. Coldren, *Fellow, IEEE*

(Invited Paper)

**Abstract**—We show that it is necessary to eliminate carrier diffusion in the active region for viable vertical-cavity lasers (VCL's) with small dimensions. However, methods that work well in reducing lateral carrier leakage in narrow ridge-waveguide lasers such as silicon induced disordering may be problematic in VCL structures. Encouraging results from novel methods for impurity free intermixing for VCL applications are presented.

**Index Terms**—Quantum-well intermixing, semiconductor device fabrication, surface emitting lasers.

## I. INTRODUCTION

VERTICAL-CAVITY laser (VCL) performance has improved by employing current confinement and optical waveguiding techniques. Early on, apertures defined by air [1] and oxide [2], [3] were shown to be very effective in constricting the current within the lasing mode. Furthermore, it was realized that the aperture provided optical confinement as well [4]–[7]. Devices originally using apertures formed in one of the  $\lambda/4$  ( $\approx 80$  nm) distributed Bragg reflector (DBR) layers could be scaled down to about  $8\text{ }\mu\text{m}$  in diameter before the threshold current density began to increase significantly. Excess size-dependent losses due to optical scattering off of these thick, abrupt apertures prevented the smaller devices from lasing [6]. Simple reduction of the aperture thickness reduced the optical scattering losses thereby significantly improving the scalability of the threshold current and wallplug efficiency [8]–[10]. As shown in Fig. 1, by tapering the edge of the aperture [11] a more lens-like element is created which virtually eliminates the scattering losses [12].

Having passed through the aperture, the current is free to spread before reaching the active region, and once in the active region, injected carriers are free to diffuse radially. Both mechanisms result in more current required to attain threshold. In devices with negligible scattering losses, more

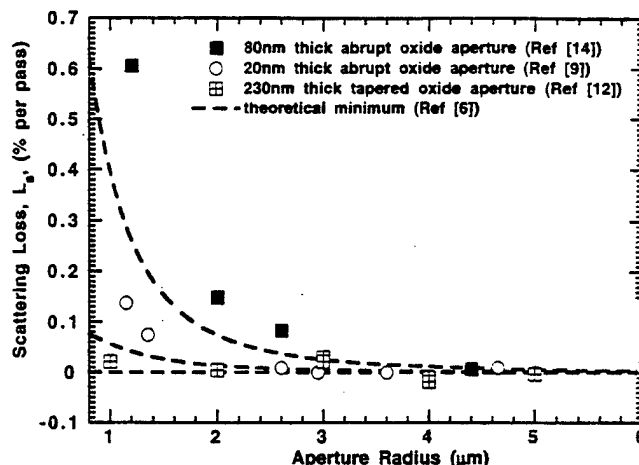


Fig. 1. Excess optical loss versus radius comparing  $\lambda/4$  abrupt oxide aperture, 200-Å abrupt oxide aperture, tapered oxide aperture at null. The values extracted from measured external differential efficiencies show that optical scattering and diffraction losses have been virtually eliminated for the tapered aperture device.

than half of the threshold current is lost to current leakage even at diameters of  $8\text{ }\mu\text{m}$  [13]. When the aperture is moved to a low doped region closer to the active region ( $\approx 20$  nm), current spreading can be reduced, and carrier leakage due to lateral diffusion dominates with more than half of the current wasted to carrier leakage at diameters of  $6\text{ }\mu\text{m}$  as shown in Fig. 2.

In this paper, we summarize the magnitude of these current loss mechanisms and suggest that QW intermixing can be used to reduce such losses. Various approaches of allowing QW intermixing are reviewed, and new results are presented for use in VCL structures.

## II. SIGNIFICANCE OF CARRIER LEAKAGE

Excess threshold currents due to current spreading under the oxide and radial diffusion of carriers in the active region both scale linearly with device radius in the range of sizes considered here [13], [15]. Thus, in the absence of optical losses it is difficult to determine the dominate current leakage mechanism by finding the size dependence of the threshold current alone.

Manuscript received February 6, 1998; revised May 6, 1998.

R. L. Naone is with the Materials Department, University of California at Santa Barbara, Santa Barbara, CA 93106 USA.

P. D. Floyd is with Xerox-PARC, Palo Alto, CA 94302 USA.

D. B. Young is with the Rockwell Science Center, Thousand Oaks, CA 91360 USA.

E. R. Hegblom, T. A. Strand, and L. A. Coldren are with the Department of Electrical and Computer Engineering, University of California at Santa Barbara, Santa Barbara, CA 93106 USA.

Publisher Item Identifier S 1077-260X(98)05848-1.



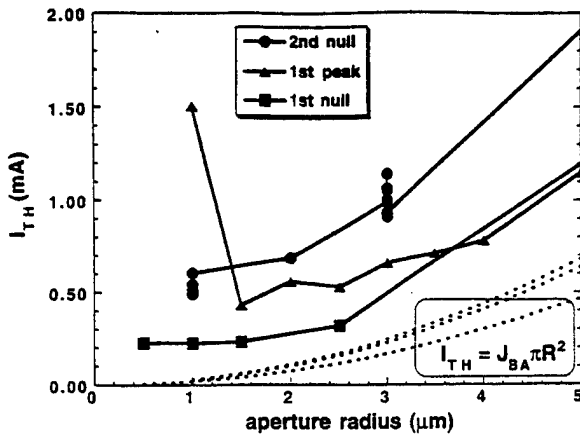


Fig. 2. The squares denote experimental threshold currents for the tapered oxide aperture devices. Assuming that optical losses have been eliminated from the tapered oxide aperture devices, the dashed curve shows the theoretical minimum threshold current extrapolated from the value of the 17- $\mu\text{m}$  radius device. However, the excess threshold currents shown are attributed mainly to carrier leakage.

The radial dependence of 2-D current density in a VCL can be written by  $\vec{J}(r) = -J_z(r)\hat{z} + J_r(r)\hat{r}$ . Under the aperture we assume that the current distribution is uniform along the  $\hat{z}$  direction so we can replace all the quantum-well (QW) and undoped separate confinement heterostructure (SCH) layers by a single carrier channel of thickness  $\zeta$ . Thus, the sheet carrier density distribution,  $N_s(r)$ , in the active region is found by solving the ambipolar carrier transport equation.

$$D \frac{1}{r} \frac{d}{dr} \left( r \frac{dN_s}{dr} \right) - \frac{N_s}{\tau} = -\frac{\eta_{inj} J_z(r)}{q} \quad (1)$$

where we have assumed an injection efficiency  $\eta_{inj}$ , an ambipolar diffusivity  $D$ , and a constant carrier lifetime  $\tau$ , set  $\approx 2$  ns, the value at threshold [16]. Then, the radial diffusion current out of an active region of radius  $R$  is given by  $I_r(R) = 2\pi R D q (dN_s/dr)|_{r=R}$ .

Given a total current  $I_{total}$  into the aperture, an analysis by Dutta gives an approximate radial current density profile,  $J_z(r)$ , which includes current spreading in a resistive layer under the aperture before the diffusive layer of thickness  $\zeta$  [17]

$$J_z(r) = I_{total}/\pi R^2 \times \begin{cases} 1, & r \leq R \\ \exp[-(r-R)/r_0], & r > R \end{cases} \quad (2)$$

where  $r_0$  is a characteristic radius of current spreading dependent on the square root of the conductivity-thickness product of the resistive layer. If an annular, intracavity contact is used [8], [18]–[20], as is done when it is undesirable to pass current through the DBR, the current injected at the aperture is no longer uniform because of undesirable current crowding at the edge of the aperture [18], and  $J_z(r)$  assumes a modified Bessel function form [19]. Substituting (2) into (1),  $N_s(r)$  can be solved [17].

With current spreading, the solution to (1) gives a relatively flat sheet carrier density profile at the edge of the active region resulting in small diffusion currents. Conversely, if current is

uniformly injected in the center of the device,  $r_0 \rightarrow 0$ , a relatively steep gradient in the carrier density at the aperture edge develops, creating a proportionally high-diffusion current out of the active volume defined by the aperture radius. This uniform injection regime is closely realized in devices where a tapered oxide aperture is only 300 Å from the active region [21].

As optical losses and current spreading are reduced, a larger fraction of the threshold current in small devices are due to carrier diffusion. Eliminating carrier diffusion will allow devices to be scaled down to smaller sizes with a corresponding decrease in threshold current. A buried heterostructure is a straightforward approach of providing a lateral barrier to diffusion, but the etch and regrowth process in the AlGaAs–GaAs system is ineffective because the surface recombination at the regrowth interface is nearly as bad as at a free surface unless regrowth is done *in situ* [22]. Other efforts aimed at creating structures which inhibit the lateral diffusion of carrier during growth include growth on patterned substrates, segmented QW's by thermal desorption [23], and self-assembled InGaAs islands [24]. Lateral confinement is also possible by intermixing the laser structure around the active region, creating a buried heterostructure without regrowth. This latter approach shall be the primary topic of discussion in this paper.

### III. DIFFUSION IN GROUP-III ARSENIDES

Intermixing involves the diffusion of point defects in the zinc-blende lattice and their interaction with the atoms in the crystal. Disorder of heterostructures of the group-III arsenides occurs primarily through lattice exchange interactions of Al, Ga, and In with group-III vacancies and interstitials [25]. Diffusivity of the group-III atom is proportional to the local concentration of vacancies and interstitials so any environment or process which introduces point defects serves to enhance the intermixing such as doping and arsenic overpressure [25], ion-implantation [26], impurity free vacancy disordering (IFVD) [27], and laser induced disordering [28]. It will be shown in Section IV-A that impurity induced disordering (IID) may be undesirable since the performance of VCL's are very sensitive to the free carrier absorption of high doping and the current leakage through parasitic junctions created by this approach. As such, IFVD approaches using various capping material such as SiO<sub>2</sub> [27], [29], [30], low-temperature GaAs [31], spin-on-glass [32], steam oxidized AlAs [33], and, possibly, low energy neutral ion-implantation [34] should be explored.

In a typical InGaAs–GaAs QW 120 meV deep, the electron ground state is already a third of the way up from the InGaAs conduction band edge. Even complete intermixing of the QW's cannot provide the  $4k_B T$  (100 meV) of lateral bandgap difference desired. Thus, disordering of typical InGaAs–GaAs–AlGaAs active regions needs to diffuse in Al, possibly from the SCH, to create a larger bandgap difference. In the temperature range of interest, the interdiffusion coefficient of Ga and In are known to be about an order of magnitude lower than that of Al and Ga [31], [35] presumably due to an

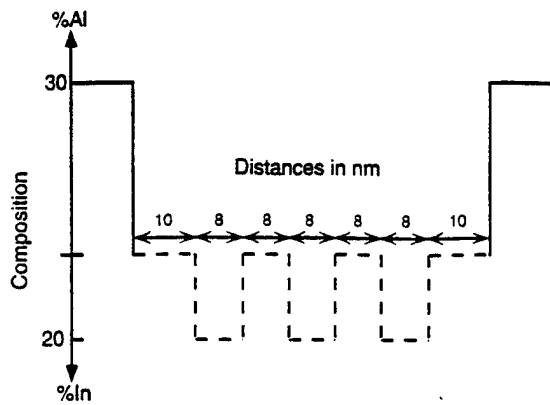


Fig. 3. A schematic of the MQW structure consisting of three 80-Å  $\text{In}_{0.20}\text{Ga}_{0.80}\text{As}$  QW's (dashed) and the  $\text{Al}_{0.30}\text{Ga}_{0.70}\text{As}$  SCH (solid).

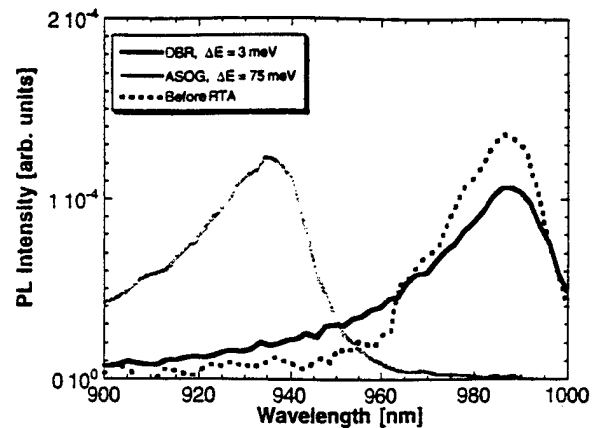
TABLE I  
EFFECT OF ALAs ON THE PHOTOLUMINESCENCE BLUESHIFT OF  $\text{InGaAs}$  QW's

Al in the barrier?	950 °C, 40" RTA?	PL Peak $\lambda$ (nm)	PL Intensity (arb. units)
no	no	988	1.0
no	yes	934	0.5
yes	no	986	0.3
yes	yes	900	0.2

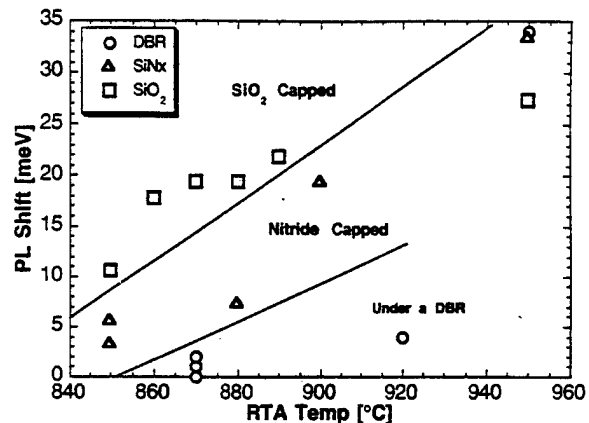
inverse relation between the self-diffusivity of the group III metals and their bond strength [36]. Thus, Al can be added to the QW barriers to facilitate Al diffusion into the  $\text{InGaAs}$  wells.

To illustrate the magnitude of the bandgap shift using this approach we grew two MQW samples by molecular beam epitaxy (MBE) having a structure similar to Fig. 3 with the  $\text{In}_{0.18}\text{Ga}_{0.82}\text{As}$  QW's 600 Å from the surface. In one sample we substituted two monolayers of GaAs in the center of the barriers with AlAs. We coated both samples with 800 Å of  $\text{SiO}_2$  by plasma-enhanced chemical vapor deposition (PECVD) at 250 °C. Then, we induced intermixing with a 950 °C 40-s rapid thermal anneal (RTA). The extent to which diffusion has occurred is most easily determined by photoluminescence (PL), and measurements of the blueshift of the QW peak due to disordering during RTA are summarized in Table I. The sample with Al in the barriers showed an 86-nm blueshift, while there was only a 54-nm blueshift in the QW PL peak without Al nearby. However, as expected, there was lower PL intensity from the samples with Al in the barriers.

It is widely observed that the amount of disordering is highly dependent on the type of capping material used. Fig. 4 shows the results of samples disordered by RTA using different capping materials. The structure of the samples used for this set of data is similar to Fig. 3 in which the top most QW is 600 Å from the surface. In our studies the silicon dioxide ( $\text{SiO}_2$ ) and silicon nitride ( $\text{SiN}_x$ ) films were deposited 600–800 Å thick by PECVD at 300 °C. The spin-on-glass (SOG), obtained from the Emulstone Company, is a liquid which can be applied to a sample like photoresist and cured to



(a)



(b)

Fig. 4. (a) The PL of a VCL sample disordered at 920 °C for 2 min using spin-on-glass shows a large blueshift of the QW peak while the area underneath the DBR remains intact. (b) The PL shift after a 3-min anneal at different temperatures for  $\text{SiO}_2$ ,  $\text{SiN}_x$ , and under a DBR are shown. SOG results are not plotted since the PL shifts were  $\geq 50$  meV.

form an amorphous silica glass doped 5% by weight with arsenic. Trends shown in Fig. 4 show that the SOG disorders the most for any given temperature. Fig. 4 also includes the intermixing intrinsic to the material by showing the amount of blueshift measured from an annealed VCL in which the top DBR was removed after the thermal treatment. The result is encouraging since without intentionally trying to disorder the material, the active region remains intact for temperatures below about 920 °C.

#### IV. DIFFERENT APPROACHES TO LATERAL CARRIER CONFINEMENT

##### A. Impurity-Induced Disordering (IID)

Hu *et al.* used silicon impurity-induced disordering (IID) to successfully reduce the threshold current in ridge-waveguide lasers to 0.9 mA [37]. They used a self-aligned process which diffuses Si in from the sides of an etched ridge at 850 °C for  $\approx 1$  h. They were able to confine the carriers to a width of about a quarter-micrometer using this technique.

Subjecting a VCL to the same thermal treatment will severely degrade the reflectivity of the DBR as the interface

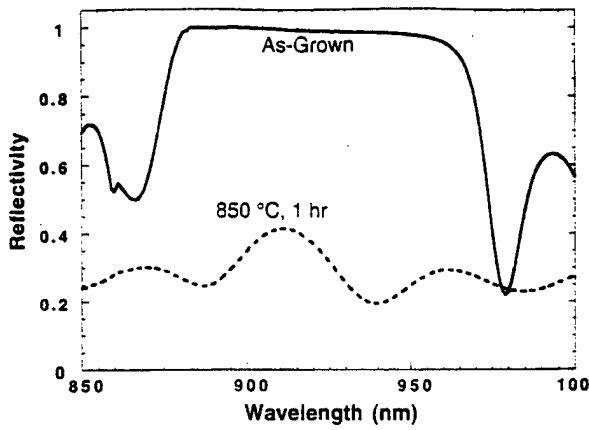


Fig. 5. Measured reflectivity for a greater than  $10^{18} \text{ cm}^{-3}$  Si-doped DBR before and after an  $850^\circ\text{C}$  furnace anneal for 1 h [40].

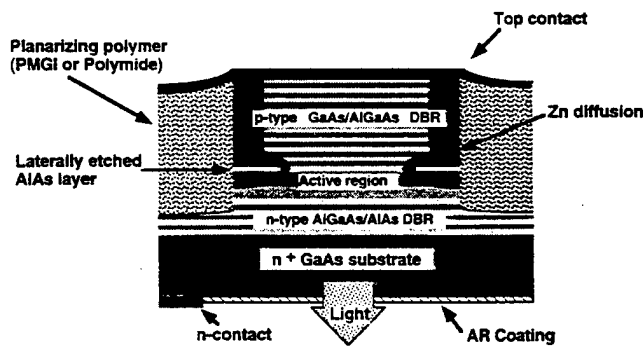


Fig. 6. Schematic of IID-VCL [40].

composition is blurred by IID (see Fig. 5) unless the Si doping level in the n-DBR is kept below about  $1 \times 10^{18} \text{ cm}^{-3}$  [38]. In one approach to avoid this degradation, Floyd *et al.* [39], [40] used the lower temperatures of Zn IID to confine carriers in VCL's. Zn diffusions were performed on VCL pillars with undercut air-apertures,  $\lambda/4$  thick, in a sealed ampoule at  $600^\circ\text{C}$  for 25 min, and after further processing the completed VCL is shown schematically in Fig. 6.

Threshold current in a  $4.6\text{-}\mu\text{m}$  diameter device was  $670 \mu\text{A}$  ( $680 \mu\text{A}$ ) with an external efficiency of 41% (44%) for the IID (nondisordered, air-gap) VCL. The size dependence of the external efficiency,  $\eta_{\text{ext}}$ , was analyzed to determine the excess optical losses,  $L_S$ , using,

$$L_S = T(\eta_{\text{inj}}/\eta_{\text{ext}} - 1) - L_{BA} \quad (3)$$

where  $T$  is the mirror transmission,  $L_{BA}$  is the one-dimensional (1-D) round-trip cavity loss, and  $\eta_{\text{inj}}$  is the injection efficiency above threshold. Fig. 7 compares the size-dependent optical losses between IID-VCL's and VCL's of the same structure without the Zn diffusion. We see that the optical losses, due only to scattering off the aperture, are similar in the two structures, indicating that the high p-doping of the diffusion did not contribute to free carrier absorption.

Once the optical losses have been extracted from the external efficiency measurements, a threshold current was calculated taking into account only these losses [41]. As shown in

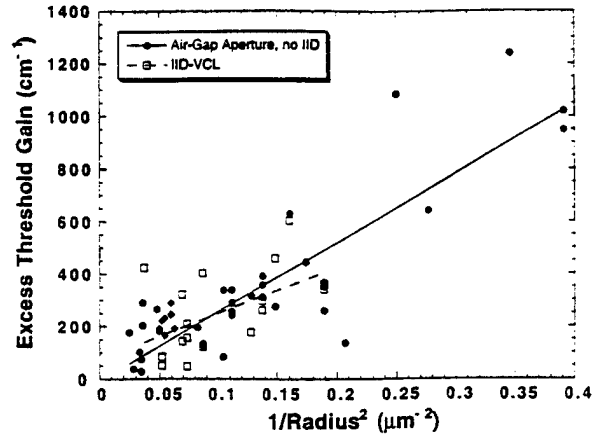


Fig. 7. Excess threshold gain versus  $1/(\text{rad})^2$  obtained from external differential efficiency measurements on Zn-IID and air-gap apertured VCL's [40]. This shows similar optical losses for both structures from the air-gap present in both designs, indicating that the Zn diffusion does not incur significant free carrier absorption.

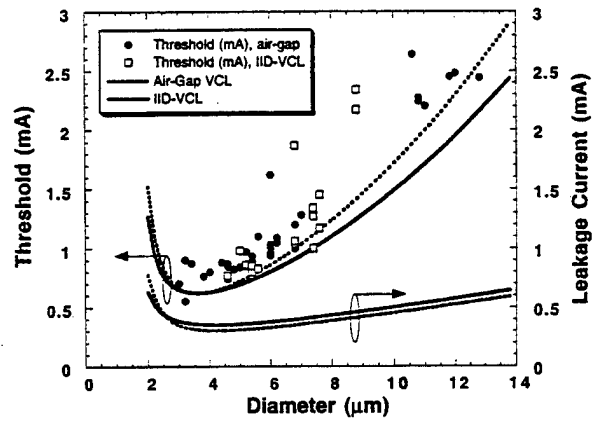


Fig. 8. A comparison between the leakage current of the air-gap only (circles) and IID (squares) VCL's [40]. The dotted line shows the calculated threshold current including size-dependent optical scattering losses. The data show similar magnitudes of leakage current (see text).

Fig. 8, the measured threshold currents were higher, and the excess current above the calculated values represent current leakage. The excess current in the air-gap VCL data is due to current spreading and carrier diffusion [13]. Earlier attempts at using Zn IID resulted in large current leakage through a p-Zn-(GaAs-AlAs) n-DBR parasitic p-n junction, but the data presented here resulted from a VCL structure with an AlGaAs-AlAs n-DBR serving as a termination layer for the parasitic junction. Still, slightly higher leakage currents in IID devices larger than  $2.5 \mu\text{m}$  are evident. Perhaps lateral oxidation of the AlAs could have prevented Zn diffusion from forming a continuous p-type path around the current aperture where, shown in Fig. 6, significant Zn diffusion occurred around the undercut.

The optical losses of the thick air-gap and current leakage through the parasitic junction obscured any effects of lateral confinement the Zn IID provided. The intermixing process must be compatible with the methods of eliminating the optical scattering losses mentioned previously lest the benefits of carrier confinement be unobservable.

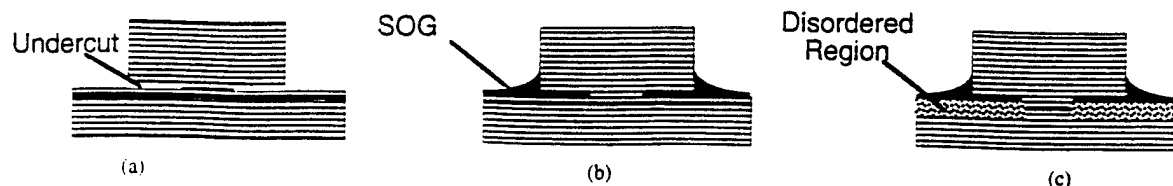


Fig. 9. Self-aligned process for IVFD by flowing SOG into an undercut layer. (a) Etch mesas and (b) form undercut. Flow SOG into undercut. (c) RTA to disorder.

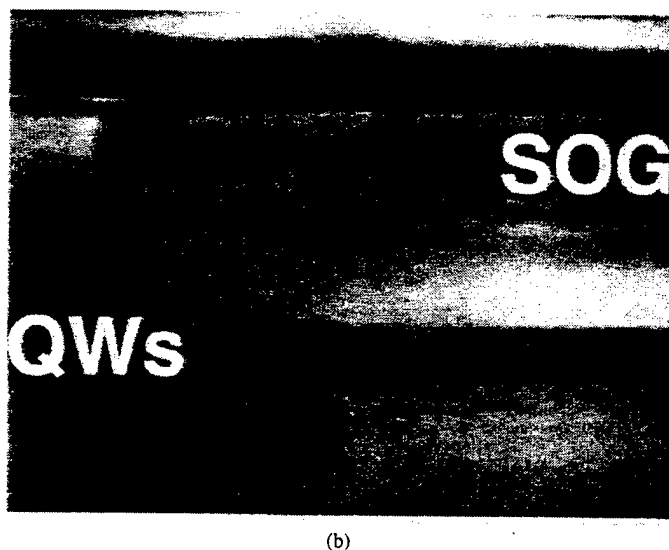
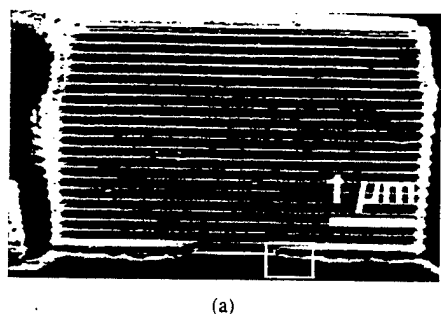


Fig. 10. (a) Cross-sectional scanning electron micrograph showing the top, p-DBR of a VCL structure undercut to form a 1-μm diameter aperture. (b) Transmission electron micrograph closeup of the boxed region at the tip of the undercut filled with SOG.

### B. Buried Vacancy Sources: A Self-Aligned Process

A process that applies the excellent IFVD properties of SOG is outlined in Fig. 9, in which we flow a 1:2 by volume dilution of SOG and ethanol into an undercut layer of a VCL mesa. This provides a self-aligned process which would disorder the active region where it is needed, directly under the current aperture. Fig. 10 shows cross-section electron micrographs of the structure after a 920 °C, 3 min RTA, showing that the SOG did wick into the undercut layer and that the structure is intact after RTA. Efforts are underway to reduce the optical scattering losses of the  $\lambda/4$ -thick undercut layer used in this preliminary experiment so that we can observe any benefits from the carrier confinement.

Researchers at the University of Southern California reported promising initial results on a novel source for IVFD using steam oxidized AlAs [33]. The MOCVD grown structure

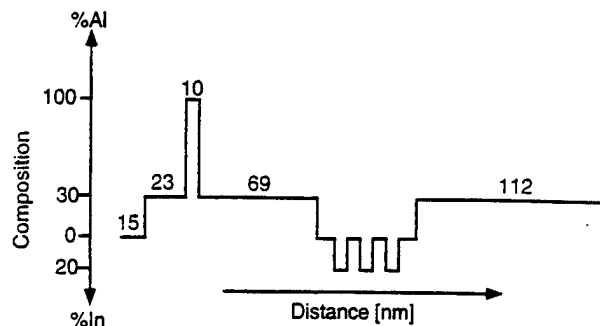


Fig. 11. A schematic of the undoped MBE grown structure used for IFVD using laterally oxidized AlAs. The QW region is the same as in Fig. 3. The surface is on the left.

used consisted of a 50-Å  $\text{In}_{0.27}\text{Ga}_{0.73}\text{As}$ -GaAs QW structure with a 1000-Å AlAs oxidation layer about 1000 Å above it. After lateral steam oxidation of AlAs, the entire structure underwent RTA for 30 s at temperatures ranging from 800 °C to 900 °C. The researchers showed that Al-oxide can enhance the intermixing of the underlying material creating an active region surrounded laterally by a ring of higher bandgap material. Cathodoluminescence (CL) spectra of the region under the oxide showed a blueshift of 64 meV with respect to the as-grown QW peak while the apertured region showed only a 19-meV blueshift.

However, the oxidation layer used would introduce excessive optical scattering loss, nullifying much of the benefits of carrier confinement this method may offer. In order to observe the effects of lateral carrier confinement, the optical losses need to be minimized with apertures defined by thin or tapered oxides as mentioned previously. In doing so, there is some concern as to whether the disordering properties of the thinner oxide are compromised since it has been observed that thinner PECVD deposited dielectric films show a decreased intermixing capacity.

We observed comparable magnitudes of blueshift in samples which had a 100-Å AlAs oxidation layer slightly closer,  $\approx 700$  Å to the 3 InGaAs QW active region, a structure which would provide low optical loss with optical confinement (see Fig. 11). We blanket deposited 600 Å of silicon nitride ( $\text{SiN}_x$ ) by PECVD at a substrate temperature of 350 °C. Next we patterned 50-μm-diameter mesas using standard photolithography and transferred this pattern to the  $\text{SiN}_x$  with a  $\text{CF}_4$  plasma etch. After removing the photoresist, the mesas were wet etched through the AlAs oxidation layer but before going through the quantum wells. Oxide-defined apertures were formed by lateral wet oxidation in an open quartz tube furnace with  $\text{N}_2$  gas flowing at 1 l/min through a water bubbler at 90 °C.

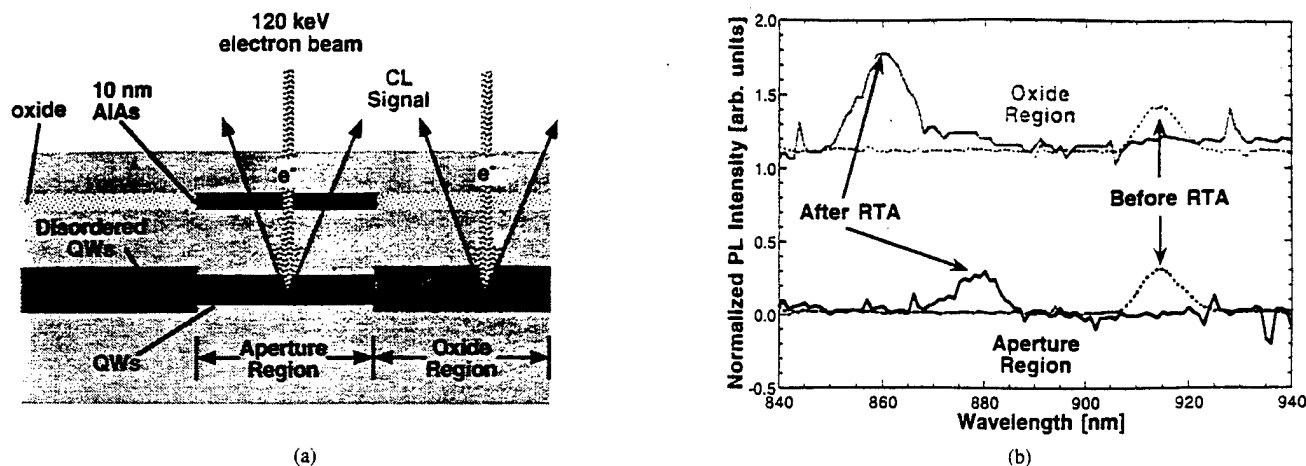


Fig. 12. (a) Schematic of the CL experiment for the AlAs-oxide experiment. (b) 10-K CL spectra showing the QW peak of the sample before (dashed line) and after (solid line) a 950 °C, 3-min anneal. Region under the oxide is represented by the grey curve. Region under the aperture by the black.

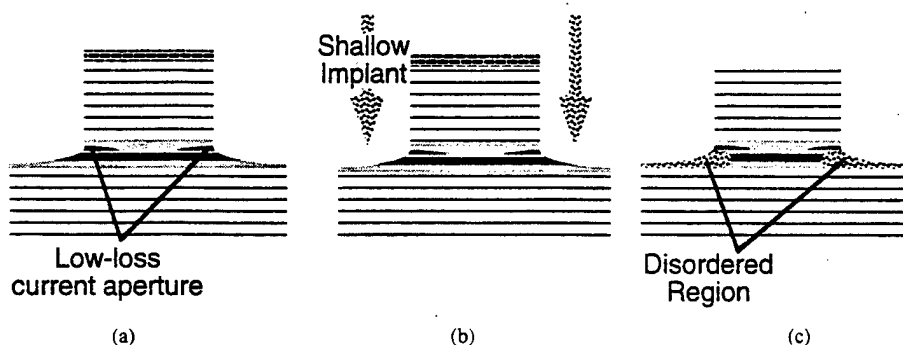


Fig. 13. Process flow for ion-implant assisted disordering. (a) Etch a small ( $\leq 6 \mu\text{m}$  diameter) VCL mesa, and form an oxide-defined aperture to ensure current and optical confinement with a brief steam oxidation step. (b) Expose to a large dose, 100–200-keV implant using the RIE etch mask as an implant mask. (c) Completed structure after the implanted regions are disordered with a  $\approx 900^\circ\text{C}$  1-min RTA.

The oxidations were performed at furnace temperatures of 450 °C and 470 °C for 30 and 10 min, respectively, to give approximately the same aperture size of 7  $\mu\text{m}$ .

Thermal treatment of the samples were performed in the AG Associates Heatpulse RTA. With the  $\text{SiN}_x$  still on the mesa tops, they were heated, top down on a GaAs wafer to prevent As desorption from the surface while the temperature was ramped at 80 °C/min to 950 °C for 3 min before cooling. It is known that thermal cycling can cause mesas to peel off at the oxide, presumably due to thermal mismatch stresses, unless measures such as grading the interface [19] or adding some Ga to the AlAs [42] are taken. In this structure, cracking of the ungraded AlAs-oxide did not occur, probably due to the fact that it was very thin. The remaining  $\text{SiN}_x$  was removed with a  $\text{CF}_4$  plasma etch. CL measurements were used to achieve the spatial resolution needed to acquire luminescence spectra from different areas in the mesa.

CL was performed in a JEOL 1200EX transmission electron microscope modified to collect light from the sample using a high numerical aperture mirror which focuses it into a large-diameter silica fiber. The luminescence was coupled into a monochromator with a liquid nitrogen cooled Ge detector at the output. A 120-keV electron beam was used to generate electron-hole pairs in the sample which was cooled with liquid He to a temperature of about 10 K. The CL spectra under two different regions, under the oxide and under the aperture, are

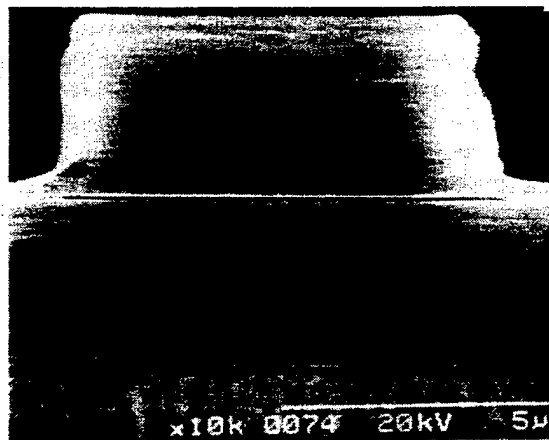


Fig. 14. Cross-sectional SEM of an implant assisted disordered VCL structure showing the dark contrast of the QW's highlighted with a 1:1 IM acetic acid: 30%  $\text{H}_2\text{O}_2$  stain etch [43]. The implant/RTA process has intermixed the active region not underneath the VCL pillar.

shown in Fig. 12. We observed a blueshift of 55.6 meV under the aperture region and about 85.1 meV under the oxide. The blueshifts under both regions are more than those reported previously because of the higher annealing temperatures used, but the difference in energy shifts (29.5 meV) shows that annealing at 950 °C causes the apertured region to disorder significantly as well, an undesirable consequence.

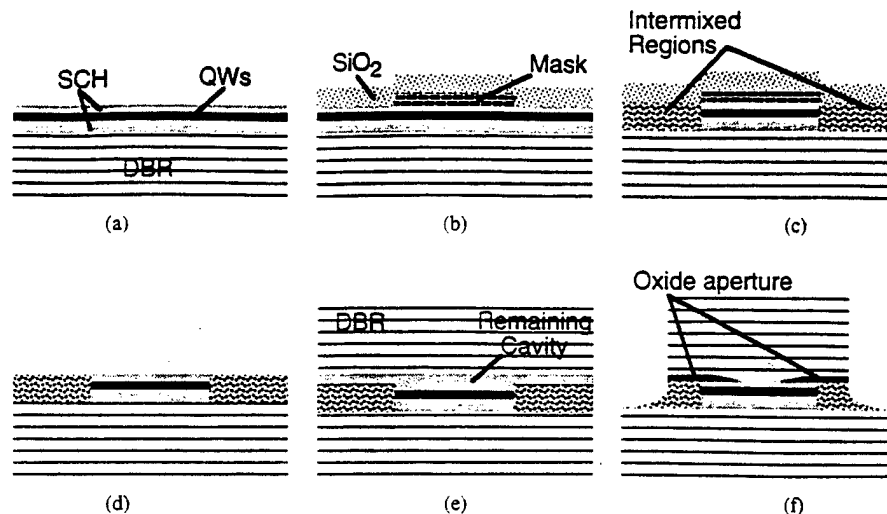


Fig. 15. Planar process flow for disordering and regrowth. (a) Grow the VCL up to the active region and part of the cavity. (b) Pattern a suitable masking material and cover with the disordering dielectric. (c) RTA to disorder. (d) Remove the dielectrics and clean the surface. (e) Regrow the remainder of the VCL. (f) Etch mesas over the nondisordered regions and finish the processing.

The prospects for this process are encouraging. A 920 °C anneal should give better contrast between the intermixed and nonintentionally intermixed regions. Also, in a full VCL structure the aperture region would be buried under an entire DBR which should protect that region from intermixing better than the  $\text{SiN}_x$  cap used in this experiment.

### C. Implant-Assisted Disordering

The IFVD techniques described previously do not increase free carrier losses and current leakage through parasitic junctions as in the IID cases, but perhaps using ion-implantation can produce an even higher concentration of the point defects needed for enhanced disordering. Consequently, the reduced annealing temperatures and times may make this a more attractive approach, and the proposed process shown in Fig. 13 requires only a near-surface, i.e., low-energy, implant that allows precise positioning of the damage profile. It is convenient to use a double layer Ni- $\text{SiN}_x$  reactive ion etching (RIE) mesa etch mask, in which the Ni serves as a sacrificial RIE etch mask, leaving behind the  $\text{SiN}_x$  ion-implant mask.

Using a similar process flow, initial efforts at the University of California at Santa Barbara [43] used a deep oxygen implant to provide a current leakage barrier from the highly doped n-type region created by a subsequent silicon implant. The implantation dose and energies were chosen to create a silicon concentration of  $10^{19} \text{ cm}^{-3}$  at the QW's. A 900 °C 30-s RTA was sufficient to observe intermixing in the implanted regions as shown in Fig. 14. A straightforward modification of this process would include a low scattering loss current aperture, such as a tapered oxide-defined aperture, before the ion-implant step.

### D. Planar Processing and Regrowth

It may be desirable to perform the disordering process on a planar surface for the inherent mechanical stability of the technique. The process outlined in Fig. 15 begins with the growth of the VCL structure up to and including the cavity.

A disordering mask such as  $\text{SiN}_x$  can be patterned on the surface followed by a blanket deposition of the disordering material, e.g.,  $\text{SiO}_2$  and SOG. After thermal treatment, the dielectrics are removed, and the flat surface that remains is conducive to a thorough surface cleaning processes. Regrowth of a semiconductor or dielectric DBR is performed to complete the VCL structure followed by processing of devices over the underlying nondisordered regions.

Due to the proximity of the QW's to the surface, it is difficult to suppress disordering where it is not desired in the annealing conditions required to create a sufficient lateral barrier. As shown in Fig. 4(b), the active region is highly blueshifted under the  $\text{SiN}_x$  mask.  $\text{SrF}_2$  has exhibited excellent performance as a disordering mask [44], but initial attempts at this planar approach had problems with the quality of the DBR regrowth by molecular beam epitaxy. We attribute the poor regrowth to the difficulty in obtaining a pristine surface after the intense thermal treatments.

## V. CONCLUSION

Numerous techniques of QW intermixing have been successful in fabricating AlGaAs-GaAs photonic integrated devices. The challenge is to push the limits of these techniques to create 100 meV of confinement in InGaAs-GaAs active regions while simultaneously adhering to a design that eliminates size-dependent optical losses and current spreading. Achieving this goal should result in significant improvement in the threshold current and efficiencies since the majority of the threshold current in a small VCL is lost to carrier diffusion.

## REFERENCES

- [1] J. W. Scott, B. J. Thibault, D. B. Young, and L. A. Coldren, "High efficiency submilliwatt vertical cavity lasers with intracavity contacts," *IEEE Photon. Technol. Lett.*, vol. 6, pp. 678-680, 1994.
- [2] D. L. Huffaker, D. G. Deppe, K. Kumar, and T. J. Rogers, "Native-oxide defined ring contact for low threshold vertical-cavity lasers," *Appl. Phys. Lett.*, vol. 65, pp. 97-99, 1994.

- [3] K. D. Choquette, R. P. Schneider, Jr., K. L. Lear, and K. M. Geib, "Low threshold voltage vertical-cavity lasers fabricated by selective oxidation," *Electron. Lett.*, vol. 30, pp. 2043-2044, 1994.
- [4] K. L. Lear, K. D. Choquette, R. P. Schneider, Jr., and S. P. Kilcoyne, "Modal analysis of small surface emitting laser with a selectively oxidized waveguide," *Appl. Phys. Lett.*, vol. 66, pp. 2616-2619, 1995.
- [5] L. A. Coldren, B. J. Thibeault, E. R. Hegblom, G. B. Thompson, and J. W. Scott, "Dielectric apertures as intracavity lenses in vertical cavity lasers," *Appl. Phys. Lett.*, vol. 68, pp. 313-315, 1996.
- [6] E. R. Hegblom, D. I. Babic, B. J. Thibeault, and L. A. Coldren, "Scattering losses from dielectric apertures in vertical cavity lasers," *IEEE J. Select. Topics Quantum Electron.*, vol. 3, pp. 379-389, Mar./Apr. 1997.
- [7] D. G. Deppe, D. L. Huffaker, T. Oh, H. Deng, and Q. Deng, "Low-threshold vertical-cavity surface-emitting lasers based on oxide-confinement and high contrast distributed Bragg reflectors," *IEEE J. Select. Topics Quantum Electron.*, vol. 3, pp. 893-904, May/June 1997.
- [8] D. L. Huffaker and D. G. Deppe, "Low threshold vertical-cavity surface-emitting lasers based on high contrast distributed Bragg reflectors," *Appl. Phys. Lett.*, vol. 70, pp. 1781-1783, 1997.
- [9] B. J. Thibeault, E. R. Hegblom, P. D. Floyd, R. L. Naone, Y. Akulova, and L. A. Coldren, "Reduced optical scattering loss in vertical-cavity lasers using a thin (300 Å) oxide aperture," *IEEE Photon. Technol. Lett.*, vol. 8, pp. 593-596, 1996.
- [10] R. Jager, M. Grabherr, C. Jung, R. Michalzik, G. Reiner, B. Weigl, and K. J. Ebling, "57% wallplug efficiency oxide-confined 850 nm wavelength GaAs VCSEL's," *Electron. Lett.*, vol. 33, pp. 330-331, 1997.
- [11] R. L. Naone, E. R. Hegblom, B. J. Thibeault, and L. A. Coldren, "Oxidation of AlGaAs layers for tapered apertures in vertical-cavity lasers," *Electron. Lett.*, vol. 33, pp. 300-301, 1997.
- [12] E. R. Hegblom, B. J. Thibeault, R. L. Naone, and L. A. Coldren, "Vertical cavity lasers with tapered oxide apertures for low scattering loss," *Electron. Lett.*, vol. 33, pp. 869-870, 1997.
- [13] E. R. Hegblom, N. M. Margalit, B. J. Thibeault, L. A. Coldren, and J. E. Bowers, "Current spreading in vertical-cavity lasers," in *Proc. SPIE Photonics West'97*, 1997, pp. 176-180.
- [14] P. D. Floyd, B. J. Thibeault, E. R. Hegblom, J. Ko, and L. A. Coldren, "Comparison of optical losses in dielectric apertured vertical-cavity lasers," *IEEE Photon. Technol. Lett.*, vol. 8, pp. 590-592, 1996.
- [15] L. A. Coldren and B. J. Thibeault, "Vertical-cavity surface-emitting lasers for free space interconnects," in *Proc. SPIE Photonics West'96*, 1996, pp. 3-34.
- [16] T. A. Strand, B. J. Thibeault, and L. A. Coldren, "Reduced lateral carrier diffusion for improved miniature semiconductor lasers," *J. Appl. Phys.*, vol. 81, pp. 3377-3381, 1997.
- [17] N. K. Dutta, "Analysis of current spreading, carrier diffusion, and transverse mode guiding in surface emitting lasers," *J. Appl. Phys.*, vol. 68, no. 5, pp. 1961-1963, 1990.
- [18] J. W. Scott, R. S. Geels, S. W. Corzine, and L. A. Coldren, "Modeling temperature effects and spatial hole burning to optimize vertical-cavity surface-emitting laser performance," *IEEE J. Quantum Electron.*, vol. 29, pp. 1295-1308, 1993.
- [19] M. H. MacDougal, P. D. Dapkus, A. E. Bond, C.-K. Lin, and J. Geske, "Design and fabrication of VCSEL's with  $\text{Al}_x\text{O}_y$ -GaAs DBR's," *IEEE J. Select. Topics Quantum Electron.*, vol. 3, pp. 905-915, May/June 1997.
- [20] J. C. Ko, E. R. Hegblom, Y. Akulova, N. M. Margalit, and L. A. Coldren, "AllInGaAs/AlGaAs strained-layer 850 nm vertical-cavity lasers with very low thresholds," *Electron. Lett.*, vol. 33, pp. 1550-1552, 1997.
- [21] E. R. Hegblom, R. L. Naone, N. M. Margalit, and L. A. Coldren, "Comparison of tapered apertures in vertical cavity lasers," presented at the IEEE LEOS'97 Conf., San Francisco, CA, Nov. 1997, paper Th13.
- [22] T. A. Strand, B. J. Thibeault, D. S. L. Mui, L. A. Coldren, P. M. Petroff, and E. L. Hu, "Low regrowth-interface recombination rates in InGaAs-GaAs buried ridge lasers fabricated by *in situ* processing," *Appl. Phys. Lett.*, vol. 66, pp. 1966-1968, 1995.
- [23] T. A. Strand, R. L. Naone, L. A. Coldren, and E. L. Hu, "Formation of GaAs quantum well islands by thermal desorption using an *al* mask," *Surf. Sci. Lett.*, vol. 359, pp. L456-L460, 1996.
- [24] J. K. Kim, unpublished results, jkkim@ecil.ucsb.edu.
- [25] D. G. Deppe and N. Holonyak, Jr., "Atom diffusion and impurity-induced layer diffusion disordering in quantum well III-V semiconductor heterostructures," *J. Appl. Phys.*, vol. 64, pp. R93-R113, 1988.
- [26] P. K. Haff and Z. E. Switkowski, "Ion-beam-induced atomic mixing," *J. Appl. Phys.*, vol. 48, pp. 3383-3386, 1977.
- [27] D. G. Deppe, L. J. Guido, N. Holonyak, Jr., K. C. Hsieh, R. D. Burnham, R. L. Thorton, and T. L. Paoli, "Stripe-geometry quantum well heterostructure  $\text{Al}_x\text{Ga}_{1-x}\text{As}$ -GaAs lasers defined by defect diffusion," *Appl. Phys. Lett.*, vol. 49, pp. 510-512, 1986.
- [28] J. E. Epler, R. D. Burnham, R. L. Thornton, T. L. Paoli, and M. C. Bashaw, "Low-threshold disorder-defined buried-heterostructure AlGaAs diode lasers by anisotropic diffusion of laser-incorporated Si," *Appl. Phys. Lett.*, vol. 51, pp. 731-733, 1986.
- [29] B. S. Ooi, S. G. Ayling, A. C. Bryce, and J. H. Marsh, "Fabrication of multiple wavelength lasers in GaAs-AlGaAs structures using a one-step spatially controlled quantum-well intermixing technique," *IEEE Photon. Technol. Lett.*, vol. 7, pp. 944-946, 1995.
- [30] Y. Suzuki, H. Iwamura, and O. Mikami, "TE/TM mode selective channel waveguides in GaAs/AlAs superlattice fabricated by  $\text{SiO}_2$  cap disordering," *Appl. Phys. Lett.*, vol. 56, pp. 19-20, 1990.
- [31] J. S. Tsang, C. P. Lee, S. H. Lee, K. L. Tsai, and H. R. Chen, "Kinetics of compositional disordering of AlGaAs/GaAs quantum wells induced by low-temperature grown GaAs," *J. Appl. Phys.*, vol. 77, pp. 4302-4306, 1995.
- [32] N. Arnold, R. Schmitt, and K. Heime, "Diffusion in III-V semiconductors from spin-on film sources," *J. Phys. D: Appl. Phys.*, vol. 17, pp. 443-474, 1984.
- [33] C. Lin, X. Zhang, P. D. Dapkus, and D. H. Rich, "Spatially selective disordering of InGaAs/GaAs quantum wells using an AlAs native oxide and thermal annealing technique," *Appl. Phys. Lett.*, vol. 71, pp. 3108-3110, 1997.
- [34] I. V. Bradley, W. P. Gillin, K. P. Homewood, and R. P. Webb, "The effects of ion implantation on the interdiffusion coefficients in  $\text{In}_x\text{Ga}_{1-x}\text{As}$ /GaAs quantum well structures," *J. Appl. Phys.*, vol. 73, pp. 1686-1692, 1993.
- [35] J. S. Tsang, C. P. Lee, S. H. Lee, K. L. Tsai, C. M. Tsai, and J. C. Fan, "Compositional disordering of InGaAs/GaAs heterostructures by low-temperature grown GaAs," *J. Appl. Phys.*, vol. 79, pp. 664-670, 1996.
- [36] R. J. Baird, T. J. Potter, G. P. Kothiyal, and P. K. Bhattacharya, "Indium diffusion in the chemical potential gradient at an  $\text{In}_{0.53}\text{Ga}_{0.47}\text{As}/\text{In}_{0.52}\text{Ga}_{0.48}\text{As}$  interface," *Appl. Phys. Lett.*, vol. 52, pp. 2055-2057, 1988.
- [37] S. Y. Hu, M. G. Peters, D. B. Young, A. C. Gossard, and L. A. Coldren, "Submilliampere-threshold InGaAs-GaAs quantum-well ridge-waveguide lasers with lateral confinement provided by impurity-induced disordering," *IEEE Photon. Technol. Lett.*, vol. 7, pp. 712-714, 1995.
- [38] K. J. Beernik, R. L. Thornton, G. B. Anderson, and M. A. Emanuel, "Si diffusion and intermixing in AlGaAs/GaAs structures using buried impurity sources," *Appl. Phys. Lett.*, vol. 66, pp. 2522-2524, 1995.
- [39] P. D. Floyd, B. J. Thibeault, J. Ko, D. B. Young, L. A. Coldren, and J. L. Merz, "Vertical cavity lasers with Zn impurity-induced disordering (IID) defined active regions," presented at the IEEE LEOS'96 Conf., Boston, MA, Nov. 1996, paper TuJ3.
- [40] P. D. Floyd, "Vertical cavity lasers fabricated using impurity induced disordering," Ph.D. dissertation, Univ. of California, Santa Barbara, CA, 1996, ECE Tech. Rep. #96-05.
- [41] B. J. Thibeault, T. A. Strand, T. Wipiejewski, M. G. Peters, D. B. Young, S. W. Corzine, and L. A. Coldren, "Evaluating the effects of optical and carrier losses in etched-post vertical cavity lasers," *J. Appl. Phys.*, vol. 78, pp. 5871-5875, 1995.
- [42] K. D. Choquette, K. M. Geib, C. I. H. Ashby, R. D. Twiston, O. Blum, H. Q. Hou, D. M. Follstaedt, B. E. Hammons, D. Mathes, and R. Hull, "Advances in selective wet oxidation of AlGaAs alloys," *IEEE J. Select. Topics Quantum Electron.*, vol. 3, pp. 916-926, June 1997.
- [43] D. B. Young, "Molecular beam epitaxy and fabrication techniques for advanced vertical cavity lasers," Ph.D. dissertation, Univ. of California, Santa Barbara, CA, 1996, ECE Tech. Rep. #96-17.
- [44] J. Beauvais, J. H. Marsh, A. H. Kean, A. C. Bryce, and C. Button, "Suppression of bandgap shifts in GaAs/AlGaAs quantum wells using strontium fluoride caps," *Electron. Lett.*, vol. 28, pp. 670-672, 1992.



Ryan L. Naone (M'98) was born on July 2, 1972, in Honolulu, HI. He received the B.S. degree in engineering and applied science from the California Institute of Technology, Pasadena, CA, in 1994, and is currently working toward the Ph.D. degree in material science at the University of California, Santa Barbara.

His current research interests include molecular beam epitaxy growth of VCL's and IFVD for optoelectronic applications.

**Philip D. Floyd** (S'87-M'95), photograph and biography not available at the time of publication.

**D. Bruce Young**, photograph and biography not available at the time of publication.

**Eric R. Hegblom** (S'95), photograph and biography not available at the time of publication.

**Timothy A. Strand**, photograph and biography not available at the time of publication.



**Larry A. Coldren** (S'67-M'72-SM'77-F'82) received the Ph.D. degree in electrical engineering from Stanford University, Stanford, CA, in 1972.

After 13 years in the research area at Bell Laboratories, he was appointed Professor of Electrical and Computer Engineering (ECE) at the University of California at Santa Barbara (UCSB) in 1984. In 1986, he assumed a joint appointment with Materials and ECE. At UCSB, his efforts have included work on novel guided-wave and vertical-cavity modulators and lasers as well as the underlying materials growth and dry-etching technology. He is currently investigating the integration of various high-speed optoelectronic devices, including optical modulators, tunable lasers, and surface-emitting lasers. He is also heavily involved in new materials growth and fabrication technology essential to the fabrication of such integrated optoelectronic components. His group has made many seminal contributions in these areas, including recent contributions in ultrawide tuning-range lasers with good spurious mode suppression, VCL's with high-efficiency high power and temperature insensitivity, and UHV *in situ* etching and regrowth. He has authored or coauthored over 300 papers, three book chapters and one textbook, and has been issued 26 patents. He is currently Director of the multicampus ARPA-supported Optoelectronics Technology Center.

Dr. Coldren is a fellow of the Optical Society of America, a past Vice-President of IEEE Lasers and Electro-Optics Society, and has been active in technical meetings.



## **Appendix 2**

# Multimode WDM Optical Data Links with Monolithically Integrated Multiple-Channel VCSEL and Photodetector Arrays

Syn-Yem Hu, Jack Ko, Eric R. Hegblom, and Larry A. Coldren

**Abstract**—We report on the design and implementation of a novel multiple-wavelength optical data link for low-cost multimode wavelength-division multiplexing (WDM) local-area network applications. This link utilizes a monolithically integrated multiple-wavelength vertical-cavity laser array and a narrow-band resonant-cavity photodetector array to transmit multiple channels of information simultaneously via a single multimode fiber. A detailed analysis on wavelength tuning and threshold characteristics of different laser cavity designs is presented. Theoretical results are compared to our experimental data. On the receiver part, both Schottky and p-i-n photodetectors with a single- or coupled-cavity structure are discussed. A novel p-i-n resonant-cavity photodetector design with a partially oxidized front mirror for linewidth control is proposed. Moreover, we also demonstrate preliminary measurements on the optical link built with our multiple-wavelength vertical-cavity laser array and photodetector array. Finally, the feasibility of constructing a multiwavelength optical data link with a single dual-core multimode fiber and an integrated laser/detector array is evaluated.

**Index Terms**— Integrated optoelectronics, laser arrays, optical interconnections, photodetectors, surface-emitting lasers, wavelength-division multiplexing.

## I. INTRODUCTION

THE DEMAND for ever faster data transmission rates (a few Gb/s up to 100 Gb/s) [1] has attracted considerable interest in the development of high-capacity optical data links for short-haul local-area network (LAN) and fiber-to-the-desktop applications. Most of the research so far has been focused on the one-dimensional (1-D) parallel optical data links [2]–[11]. For example, multiple-Gb/s aggregate data transmission rates have been demonstrated at transmission distances of about 300 m [6]–[11]. These 1-D configurations utilize multimode fiber ribbons with the one-data-channel-per-fiber arrangement. At the same time, many researchers [12]–[17] are also looking for a definitive solution to utilize the extra-wide bandwidth of optical fibers by wavelength-division multiplexing (WDM). This WDM configuration can significantly expand the transmission capacity by having multiple data channels in each fiber. However, the transmitter and receiver modules must be low in cost for the emerging “gigabit-to-the-desktop” applications. Any additional complexity in the

device fabrication and packaging technology can dramatically increase the manufacturing cost. Therefore, it is important to take these considerations into account when developing such WDM systems.

In this paper, we will introduce a WDM optical data link for low-cost LAN applications. This link utilizes a monolithically integrated multiple-wavelength vertical-cavity surface-emitting laser (VCSEL) array and a narrow-band resonant-cavity photodetector array to transmit multiple channels of information simultaneously via a single multimode fiber. First, we will focus on the transmitter designs. A detailed analysis on the wavelength tuning and threshold characteristics of different laser cavity designs will be given. Factors that limit the maximum lasing wavelength span are discussed and the theoretical results are compared to our experimental VCSEL data. In the WDM receiver section, we will emphasize designs of narrow-band resonant-cavity photodetectors. Both Schottky and p-i-n photodetectors with a single- or coupled-cavity structure are presented. In particular, a novel p-i-n resonant-cavity photodetector design with a partially oxidized front mirror for bandwidth control is proposed. Moreover, we also demonstrate some preliminary measurements on the optical link built with our multiple-wavelength VCSEL array and Schottky photodetector array. Lastly, the feasibility of constructing an optical data link with a single dual-core multimode fiber and a single-chip integrated laser-detector array is evaluated.

Fig. 1 shows the first of the two multimode WDM optical data links proposed in this paper. In this schematic diagram, wavelength-encoded optical signals are transmitted from a monolithically integrated multiple-wavelength VCSEL array to a channel-matched wavelength-selective narrow-band photodetector array via a single multimode fiber. Generally speaking, both laser and detector arrays should have planar-surface device structures to facilitate further device packaging, and they also need to be fabricated by a manufacturable processing technique. Having these basic considerations in mind, we will give a detailed description on the transmitter and receiver designs, separately, in Sections II and III.

## II. WDM TRANSMITTER DESIGN AND FABRICATION

For a low-cost WDM transmitter, we need to have a compact monolithically integrated multiple-wavelength emitter array to bring many channels of information into a single multimode

Manuscript received February 13, 1998; revised April 23, 1998. This work was supported by BMDO via the Army Research Office.

The authors are with the Department of Electrical and Computer Engineering, University of California at Santa Barbara, Santa Barbara, CA 93106 USA. Publisher Item Identifier S 0018-9197(98)05417-7.

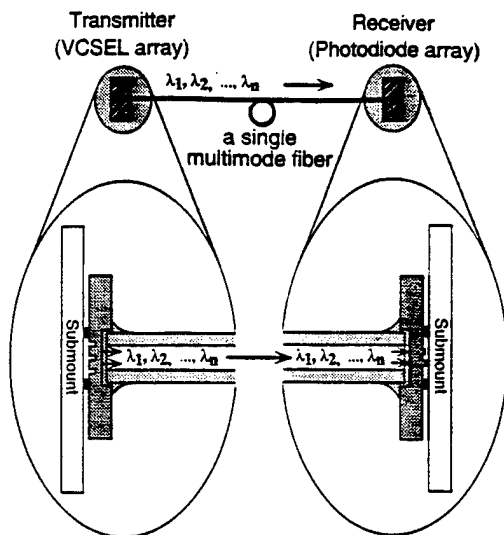


Fig. 1. Schematic diagram of the multimode WDM optical data link studied in this paper.

fiber. The availability of such low-cost multiple-wavelength emitter arrays is also a key issue for the realization of ultra-high-density multiple-layer digital versatile disk (DVD) technology [18]. The VCSEL structure is the ideal candidate because the lasing wavelength can be easily varied and its fiber packaging is potentially low-cost. In the past few years, micromechanically tunable VCSEL's [19] and monolithically integrated multiple-wavelength VCSEL arrays [12]–[13], [20]–[23] have been reported by various groups for free-space or fiber communications. However, only the anodic oxidation scheme [12] can provide the required device density and arbitrary wavelength variation within a small region. It also allows us to perform very flexible and accurate cavity-mode adjustment. Recently, we have demonstrated both multiple-wavelength top-emitting [16] and bottom-emitting [17] photonic integrated emitter (PIE) arrays designed to be coupled into a single 62.5- $\mu\text{m}$ -core multimode fiber. Unlike other techniques for making multiple-wavelength laser arrays, our photolithographically defined approach allows one to package a multiple-channel VCSEL link in the same manner as a single-channel VCSEL data link without resorting to complicated coupling optics. The simplicity in packaging this direct-coupled WDM transmitter will reduce much of the manufacturing cost.

From the system point of view, the bottom-emitting VCSEL PIE scheme is preferred, over the top-emitting version, for the WDM link shown in Fig. 1. The reason is that the former allows a larger emitting area for each array element which will, in turn, enhance the multimode operation that is recommended for multimode fiber systems [24]—an issue to be discussed later. Moreover, the bottom-emitting configuration is also compatible with the flip-chip bonding scheme to provide sufficient heat sinking for reducing thermal crosstalk between channels. Fig. 2(a) shows a schematic cross section for the bottom-emitting VCSEL PIE array with the Burrus-type [25] fiber-coupling configuration. A manufacturable planar-surface processing technique has been developed to facilitate further packaging of these VCSEL PIE arrays. In order to attain

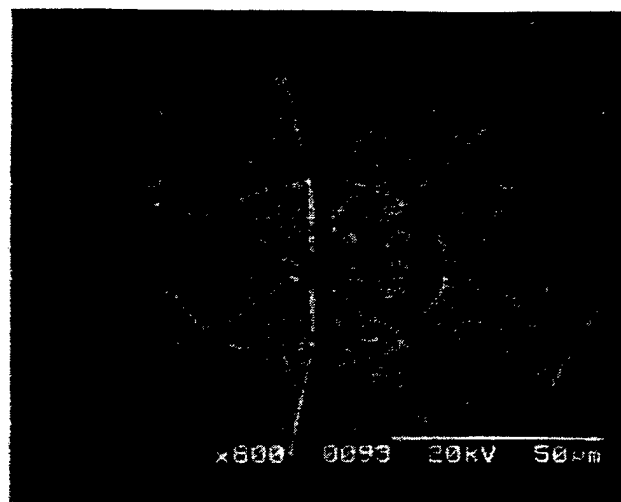
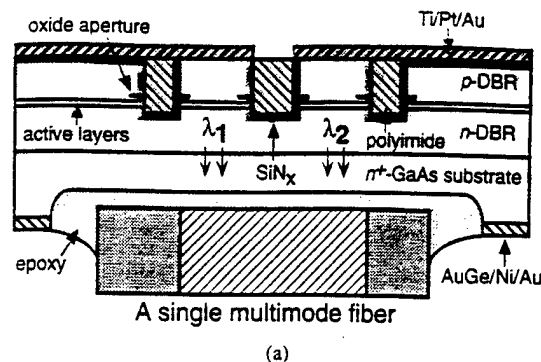


Fig. 2. (a) Schematic cross section of our bottom-emitting VCSEL PIE array with the Burrus-type fiber-coupling configuration. (b) SEM of a finished eight-channel bottom-emitting VCSEL PIE array.

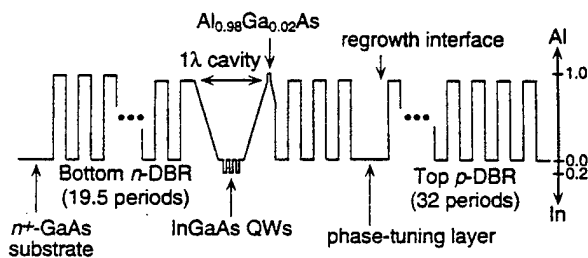


Fig. 3. An example of the aluminum and indium composition profiles for our bottom-emitting VCSEL designs. In this drawing, the phase-tuning layer is the fourth GaAs layer ( $m = 4$ ) above the  $1\text{-}\lambda$  cavity.

multiple lateral-mode operation, an oxide aperture extending only 1.0  $\mu\text{m}$  from the edge is created around the pie-shaped VCSEL mesas. Moreover, the eight bottom-emitting VCSEL's are arranged in a "pie"-like configuration (each with an area of  $88\pi \mu\text{m}^2$ ) within a 60- $\mu\text{m}$ -diameter circular area for coupling into a multimode fiber. Fig. 2(b) shows a scanning electron micrograph (SEM) of a finished eight-channel bottom-emitting VCSEL PIE array. A detailed description of the processing technique has been reported elsewhere [17]. In this paper, we will focus on the physics of wavelength tuning and threshold characteristics of different laser cavity designs.

Fig. 3 shows an example of the aluminum and indium composition profiles for our multiple-wavelength bottom-emitting

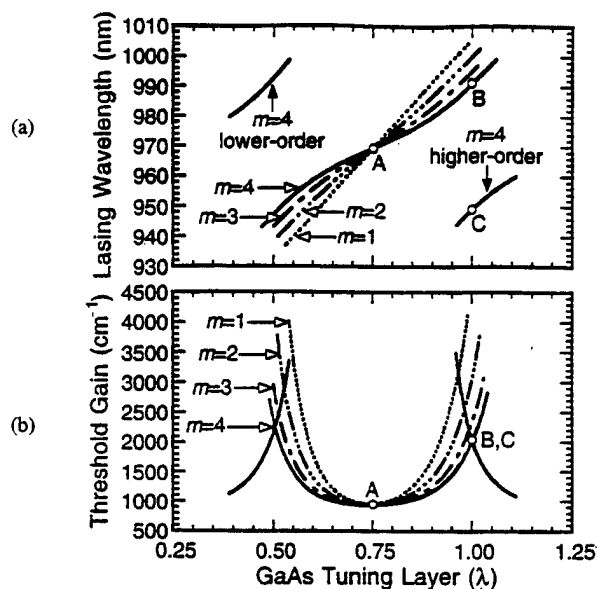


Fig. 4. The calculated (a) lasing wavelength and (b) threshold gain per QW as a function of the location and thickness of the GaAs phase-tuning layer. The number  $m$  shown beside each curve denotes that the tuning layer is the  $m$ th GaAs layer above the  $1-\lambda$  cavity. For the  $m = 4$  case (solid lines), the threshold characteristics of the adjacent cavity modes are also shown to illustrate the mode-coupling effect at the two ends of the free spectral range.

VCSEL's. The  $0.98\text{-}\mu\text{m}$  VCSEL design with InGaAs–GaAs quantum wells (QW's) and AlGaAs–GaAs distributed Bragg reflectors (DBR's) grown by molecular beam epitaxy (MBE) has been used in this study. The laser structure consists of a 32-period top p-mirror and a 19.5-period output n-mirror. The compositions for the AlGaAs quarter-wave layers are pure AlAs for the first 18 periods of the n-DBR and  $\text{Al}_{0.9}\text{Ga}_{0.1}\text{As}$  for the rest of the structure, except for the oxide-aperturing layer which is located in the first AlGaAs quarter-wave layer above the active region and has a  $400\text{-}\text{\AA}$   $\text{Al}_{0.98}\text{Ga}_{0.02}\text{As}$  layer in the middle for selective lateral oxidation. The active region consists of three  $80\text{-}\text{\AA}$  InGaAs QW's with  $120\text{-}\text{\AA}$  GaAs barriers in between. To achieve multiwavelength, VCSEL PIE arrays require two MBE growths. The first growth stops at the GaAs tuning layer and cavity modes for the individual channels are adjusted by performing anodic oxidation on the GaAs phase-tuning layer prior to the growth of the rest of the top DBR mirror [12]. In Fig. 3, the phase-tuning layer is the fourth GaAs layer above the  $1-\lambda$  cavity, where  $\lambda$  is the Bragg wavelength of the DBR's. The effects of choosing different tuning layer locations will be analyzed in the following.

Fig. 4 shows the calculated (a) lasing wavelength and (b) threshold gain per QW as a function of the location and thickness of the GaAs phase-tuning layer. The number  $m$  shown beside each curve denotes that the tuning layer is the  $m$ th GaAs layer above the  $1-\lambda$  cavity. When the GaAs tuning layer is  $0.75-\lambda$ , it behaves just like a normal quarter-wave layer and the device will lase at the Bragg wavelength  $\lambda$ . However, when the GaAs tuning layer is  $0.5-\lambda$  or  $1.0-\lambda$ , this layer itself becomes a second cavity in the whole structure with the same cavity mode as the original  $1-\lambda$  cavity. As a result, there will be a splitting in energy levels due to the mode-coupling effect. The amount of splitting decreases as the cavity separation

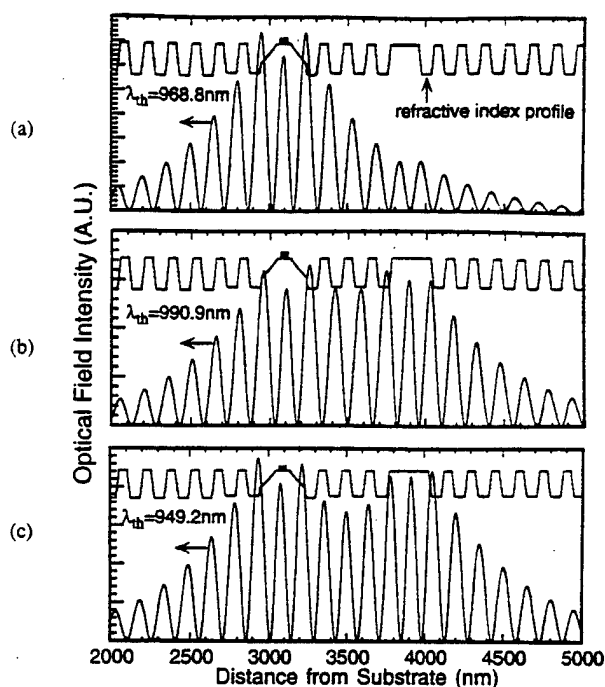


Fig. 5. The refractive index and optical field intensity profiles for the  $m = 4$  design shown in Fig. 3 and when the tuning layer thickness is (a)  $0.75-\lambda$ , lasing at  $968.8\text{ nm}$ , (b)  $1.0-\lambda$ , lasing at  $990.9\text{ nm}$ , and (c) also  $1.0-\lambda$  but for the next higher order mode lasing at  $949.2\text{ nm}$ . The corresponding lasing wavelengths are also shown in Fig. 4(a) with the notations of A, B, and C, respectively.

increases but the wavelength-tuning curve becomes more and more nonlinear. Theoretically, the tuning curve will gradually change from a straight line of slope  $2\lambda/n_s^2$  to a straight line of zero slope when  $m$  increases from 0 to  $\infty$ . Here  $n_s$  is the refractive index of the cavity. In order to achieve equidistant wavelength separation, a small  $m$  value, such as  $m = 0$  or at most  $m = 1$ , should be used. Under this circumstance, however, the overall variation in device threshold currents will be much wider than the design with a larger  $m$ , as shown in Fig. 4(b). Moreover, the tolerance in process control of the anodic oxidation also becomes tighter because of the steeper wavelength tuning rates shown in Fig. 4(a). For current short-distance coarse WDM applications, it is possible to use the  $m = 3$  or even  $m = 4$  design because the channel spacing is still much wider than  $4\text{ nm}$ , which is mainly limited by the receiver bandwidth [15].

In both Fig. 4(a) and (b), the threshold characteristics of the adjacent higher order and lower order modes for the  $m = 4$  case (solid lines) are shown to illustrate the mode-coupling effect at the two ends of the free spectral range. This coupling effect caused not only nonlinearity but also abrupt switch in device threshold and lasing wavelength. To understand this phenomenon, we need to examine the optical field profiles inside the cavity. Fig. 5 shows the refractive index and optical field intensity profiles for the  $m = 4$  design shown in Fig. 3, when the tuning layer thickness is (a)  $0.75-\lambda$ , lasing at  $968.8\text{ nm}$ , (b)  $1.0-\lambda$ , lasing at  $990.9\text{ nm}$ , and (c) also  $1.0-\lambda$  but for the next higher order mode lasing at  $949.2\text{ nm}$ . The corresponding lasing wavelengths are also shown in Fig. 4(a) with the notations of A, B, and C, respectively.

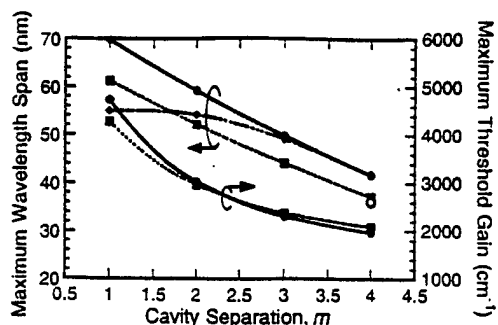
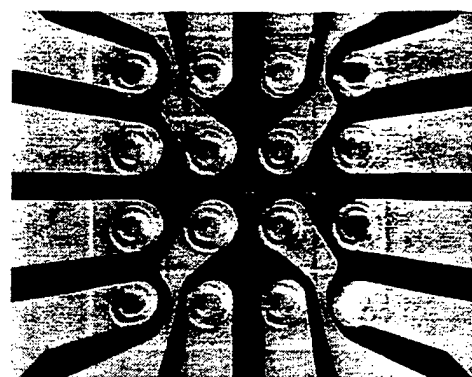


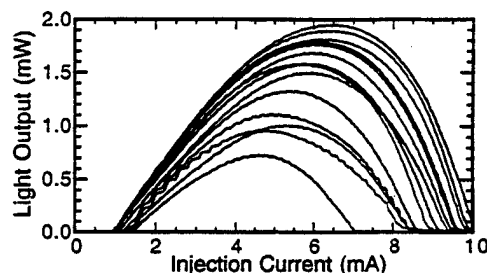
Fig. 6. The maximum lasing wavelength span and the required maximum threshold gain per well as a function of  $m$ , the position of the GaAs phase-tuning layer. The solid curves are for the design shown in Fig. 3 while the dotted curves and the experimental data (O) are for the special case when we increase the first GaAs layer below the  $1\text{-}\lambda$  cavity to  $1.25\text{-}\lambda$  to avoid exposing AlGaAs layers on the etched surface. Moreover, if the maximum achievable threshold gain is experimentally limited to  $2400\text{ cm}^{-1}$  per QW, the solid curve of the maximum wavelength span will be reduced to the dash-dotted curve.

The two modes, (b) and (c), have very similar threshold gains and will both appear in the emission spectrum of the device. As one can perceive, the observed systematic variation in threshold characteristics comes from the extending of optical field intensity from the central  $1\text{-}\lambda$  gain cavity into the GaAs phase-tuning layer when the cavity mode is detuned away from the Bragg wavelength of the DBR's. Another factor that also causes reduction in optical confinement factor is the shift of the optical standing-wave peak away from the InGaAs QW's. Consequently, threshold current will have its lowest value at the Bragg wavelength and goes up in either direction of the wavelength. In particular, when the tuning layer thickness is outside the  $(0.5\lambda, 1.0\lambda)$  range, the adjacent modes have lower threshold gains than the central mode and thus will dominate the lasing behavior. The variation of DBR mirror reflectivities versus wavelength also influences the threshold behavior (but not so much as we have thought of earlier [16]).

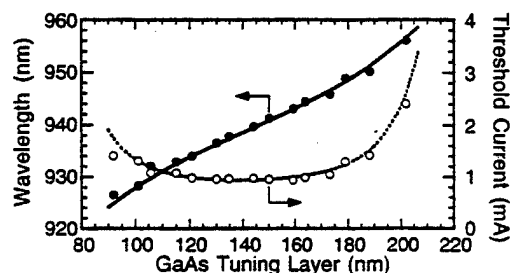
The mode splitting at the  $1.0\text{-}\lambda$  tuning layer thickness determines the maximum available wavelength span. Fig. 6 shows the maximum lasing wavelength span and the required maximum threshold gain per well as a function of  $m$ . The solid curves are for the design shown in Fig. 3 while the dotted curves and the experimental data (O) are for the special case when we increase the first GaAs layer below the  $1\text{-}\lambda$  cavity to  $1.25\text{-}\lambda$  to avoid exposing AlGaAs layers on the etched surface. In reality, however, devices will not lase if the required threshold gain is higher than what the active material can provide, especially when the tuning layer thickness is close to  $0.5\lambda$  or  $1.0\lambda$ . If the maximum lasing threshold gain is practically limited to  $2400\text{ cm}^{-1}$  per  $\text{In}_{0.2}\text{Ga}_{0.8}\text{As}$  QW [26], the solid curve of the maximum wavelength span has to be reduced to the dash-dotted curve by deducing those wavelength ranges where the required threshold gain is beyond  $2400\text{ cm}^{-1}$  per QW. It suggests that  $m = 2$  would be the optimal design for having the widest wavelength-tuning span but not too steep in wavelength-tuning characteristics. The latter is an important consideration for our processing control in anodic oxidation and also for electrically tuning control in tunable VCSEL's.



(a)



(b)



(c)

Fig. 7. Experimental demonstration of successful wavelength tuning control in a  $4 \times 4$  multiwavelength bottom-emitting VCSEL array with the layer design shown in Fig. 3 ( $m = 4$ ). Here we show (a) a photograph of a finished  $4 \times 4$  array, (b) the measured CW light-current characteristics, and (c) the measured (dots) and expected (curves) threshold characteristics as a function of the remaining thickness of the GaAs phase tuning layer.

Experimentally, we have fabricated several multiwavelength VCSEL arrays to verify our theoretical analysis. These VCSEL arrays are tested at room temperature under CW operation. Fig. 7(a) shows a photograph of a  $4 \times 4$  multiwavelength VCSEL array with the layer design shown in Fig. 3 ( $m = 4$ ). These VCSEL's are  $9\text{ }\mu\text{m}$  in pillar diameter and  $30\text{ }\mu\text{m}$  in pitch. The oxide aperture is about  $4\text{ }\mu\text{m}$  in diameter. This array is useful for free-space optical interconnections with the assistance of an integrated GaAs microlens on the output substrate side [12], [27]. Fig. 7(b) shows the measured CW light-current characteristics and Fig. 7(c) shows the measured (dots) and expected (curves) threshold characteristics as a function of the remaining thickness of the GaAs phase tuning layer. As one can see, the wavelength tuning control has been very successful. The achieved lasing wavelength span in this sample is about 30 nm. Furthermore, the variation in

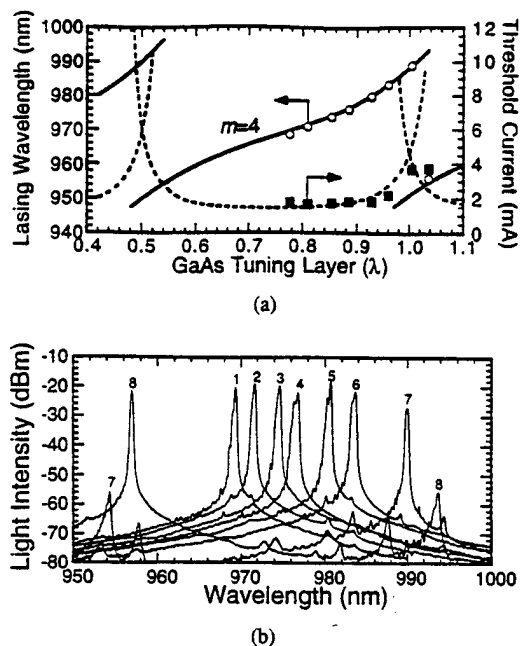


Fig. 8. (a) Experimental and theoretical threshold characteristics of an eight-element bottom-emitting VCSEL PIE array with the design shown in Fig. 3 ( $m = 4$ ) but also with a 1.25- $\lambda$  GaAs layer below the 1- $\lambda$  cavity for the reason described in the text. (b) The lasing spectra of the VCSEL PIE array measured at 5–6 mA.

threshold currents of this array has also been well explained by our theoretical modeling. For our  $m = 4$  design, a factor of two increasing in threshold current is expected from the central channel to either end of the working wavelength span. However, most of the increase in threshold current occurs near the two ends of the wavelength span. Therefore, it is possible to reduce the threshold variation by sacrificing some wavelength span to prevent the possible cost penalties in a more complicated biasing-circuit design. In Fig. 7(c), the second longest wavelength channel is missing due to improper device processing while the longest device died during the initial probing before we started recording the light-current curves shown in Fig. 7(b).

Fig. 8(a) shows the experimental and theoretical threshold characteristics of an eight-element bottom-emitting VCSEL PIE array with the design shown in Fig. 3 ( $m = 4$ ) but also with a 1.25- $\lambda$  GaAs layer below the 1- $\lambda$  cavity for the reason described earlier. Most devices lased at around 1.7 mA with a bias voltage of 2.4 V. If we number the devices according to the tuning layer thickness, channels 1–6 exhibit similar electrical and spectral characteristics when the output power is below 5 mW. Channel 4 has 7.3-mW maximum output power, 50.2% differential quantum efficiency, and 11.8% maximum wall-plug efficiency. The theoretical curves shown in Fig. 8(a) has included the observed growth-rate offset between the two MBE growths. As theoretically predicted, the device (channel 8) with a GaAs tuning layer over 1.0 $\lambda$  lases at the adjacent higher order mode. Fig. 8(b) shows the lasing spectra of this VCSEL PIE array measured at 5–6 mA. The achieved lasing wavelength span from this array is 32.9 nm but the maximum available wavelength span is about 36.7 nm. From Fig. 8(a) one can see that only half of the usable tuning range has

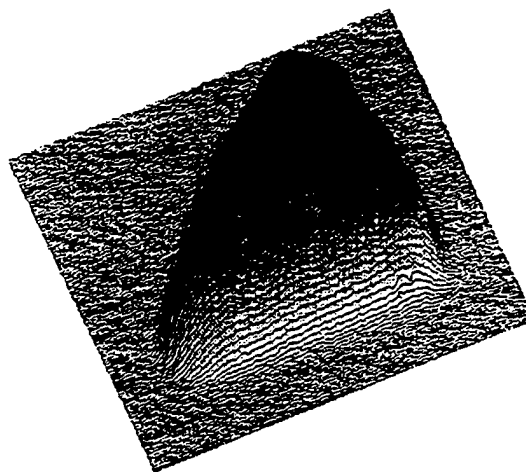


Fig. 9. The near-field intensity profile of our “pie”-shaped VCSEL taken at an injection current of 8.31 mA.

been used by this sample. It is possible to further optimize the channel allocation so that all eight channels can be located at the flat part of the threshold curve.

Modal noise is a well-known phenomenon for multimode fiber systems when a coherent light source is used [28]. For our multimode WDM links, if single-mode VCSEL's are used at the transmitter part, output intensity profile for each VCSEL channel at the other end of the fiber will be very likely centered in a few spots which are distributed over the 62.5- $\mu$ m-diameter core in an unpredictable manner. Moreover, these spots will move around the fiber core when the fiber is bent or vibrated somewhere. As a result, the insertion loss for each channel in our broadcast-type receiver design becomes completely uncontrollable because the photodetectors are made in a “pie”-like shape and will receive light signals only from a certain fixed area over the 62.5- $\mu$ m-diameter fiber core. This is why broad-bandwidth multimode VCSEL's are strongly required for those multimode WDM systems with their detector area smaller than the fiber core [24], [29]–[31]. For our VCSEL PIE devices, they are single-mode or nearly single-mode at low output power ( $<1$  mW), which is probably related to the special “pie”-shaped geometry. However, when the output power is raised to above 1.0 mW, all channels become more and more multimode-like. For example, Fig. 9 shows the near-field intensity profile of our “pie”-shaped VCSEL taken at an injection current of 8.31 mA. This measurement was performed by using an 80 $\times$  infrared microscope lens and a high-sensitivity infrared camera. The achieved 3-dB spectral bandwidth is around 1.7 nm at the peak power with four to five dominant lateral modes. The emission spectra of all PIE elements are preferentially polarized along the radial directions. To inspect the intensity profiles coming out of the multimode fiber, laser emission from one VCSEL element was coupled into a 300-m-long 62.5- $\mu$ m-core multimode fiber without using any coupling optics. No etched well as shown in Fig. 2(a) has been done to the substrate yet. This device was biased at 5 mA with  $\sim 1.8$  mW output and it lased at 980 nm. The light intensity profiles shown in Fig. 10 are the near-field images taken at the output facet of the fiber when the VCSEL

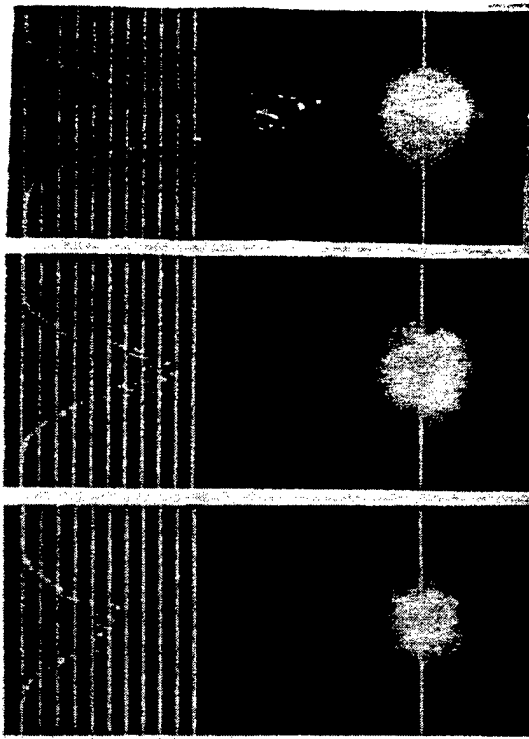


Fig. 10. Coupling of the VCSEL emission into a 300-m-long 62.5- $\mu\text{m}$ -core multimode fiber. The light intensity profiles shown are the near-field images taken at the output facet of the fiber when the VCSEL is (a) well-aligned to the fiber, (b) laterally shifted 20  $\mu\text{m}$ , and (c) laterally shifted 25  $\mu\text{m}$ .

is (a) well aligned to the fiber or laterally shifted (b) 20 and (c) 25  $\mu\text{m}$ , respectively, toward the center of the array. The case (b) is close to the situation where the fiber is aligned to the center of the VCSEL PIE array and the measured coupling loss is around 4–5 dB. As one can see, there are many intensity speckles across the fiber core which is very desirable because we need a large number of them to average out the modal interference effect of the individual speckles and to generate a much stable and more uniform intensity profile. A further optimization of our device geometry is still required to increase the spectral bandwidth at the lower injection current region.

Crosstalk is an important subject for densely packed laser arrays like our VCSEL PIE's. It is known that the overall crosstalk may consist of three major components: optical [32], [33], electrical [34], and thermal [35] crosstalk. We have found that spontaneous emission from one laser can change adjacent devices' thresholds [36] because our "pie"-shaped VCSEL's are only 3  $\mu\text{m}$  apart and the polyimide filling in between is transparent to the emission light. Fig. 11 shows the near-field intensity profile taken at an injection current of 0.05 mA which is far below the device's 2-mA threshold. As one can see, even though only one device (the higher intensity one) is probed, there is a significant amount of photocarriers generated in the adjacent devices which cause the observed spontaneous emission in the unprobed devices. In particular, the carrier concentration in the unprobed adjacent device is apparently nonuniform with its higher value at the probed device side. However, we can eliminate the crosstalk by prebiasing all devices to near threshold to clamp the spontaneous emission. As a result, rather low optical crosstalk ( $< -20$  dB) operation

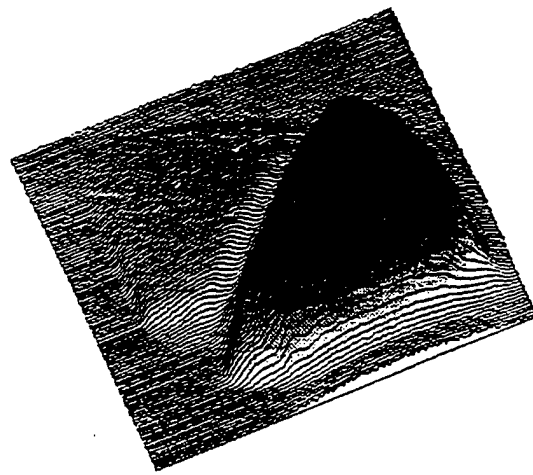


Fig. 11. The near-field intensity profile taken at an injection current of 0.05 mA.

has been demonstrated in our VCSEL PIE arrays [36]. In addition, we can block out this lateral spontaneous emission by depositing an absorptive but nonconductive film like silicon on the VCSEL sidewalls before filling the trench with polyimide or by adding some dummy walls between devices.

On the other hand, thermal crosstalk has also been measured in our planar-surface VCSEL PIE arrays. The measured thermal wavelength shift versus stage temperature is 0.43  $\text{\AA}/\text{K}$  and the thermal resistance is 0.96 K/mW which is close to the value reported in the literature [35]. The cross thermal resistances to the adjacent device, the next one, and so forth, are 0.24, 0.16, 0.10, and 0.063 K/mW, respectively. No thermal-related transient behavior was observed in the light output up to 20 MHz, the highest clock rate we used in the crosstalk measurement. Above this frequency, most of the crosstalk will be electrical crosstalk which can be suppressed by appropriate flip-chip bonding and packaging.

Preliminary on-chip high-speed testing of our bottom-emitting VCSEL PIE arrays has been performed by using a modified coaxial probe [37]. Laser output was collected by a 62.5- $\mu\text{m}$ -core graded-index fiber at the substrate side. Fig. 12(a) shows the typical modulation responses at various bias levels measured by a 20-GHz lightwave component analyzer. Fig. 12(b) shows the 3-dB modulation bandwidth,  $f_{3\text{dB}}$ , as a function of  $(I - I_{\text{th}})^{1/2}$ , where  $I$  is the bias current and  $I_{\text{th}}$  is the threshold current. The observed modulation current efficiency factor is 2.4 GHz/mA $^{1/2}$ , which is similar to the value reported earlier for a 15- $\mu\text{m}$ -diameter etched-post n-intracavity VCSEL [38]. The RC-limited bandwidth of our devices is estimated to be around 6.5 GHz, which is close to what we have obtained. Moreover, the maximum achievable modulation bandwidth for various devices in the array has been limited by the variation in maximum output power; otherwise, they behave quite similarly with respect to the same power level. An additional proton implantation under the probing pads will be very helpful to reduce the parasitic capacitance. Data transmission through a 300-m-long graded-index multimode fiber (with a 62.5- $\mu\text{m}$  core diameter) has been performed by using an O/E converter as the receiver.

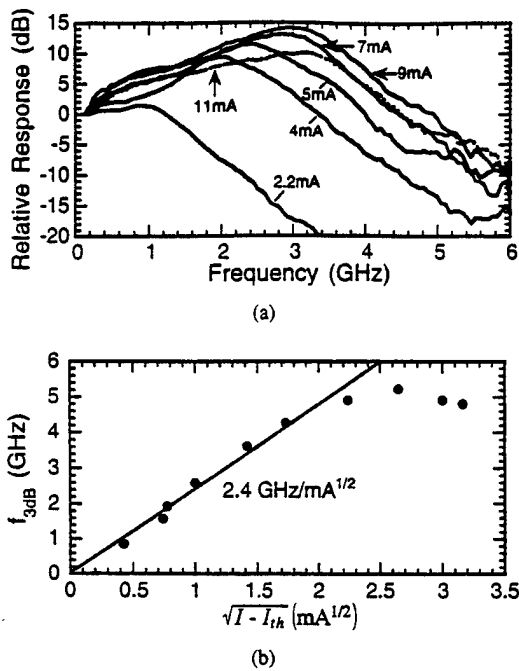


Fig. 12. (a) The modulation responses measured at various bias levels. (b) The 3-dB modulation bandwidth,  $f_{3dB}$ , as a function of  $(I - I_{th})^{1/2}$ , where  $I$  is the bias current and  $I_{th}$  is the threshold current. The observed modulation current efficiency factor is  $2.4 \text{ GHz/mA}^{1/2}$ .

The results show that these devices are capable of transmitting data up to  $1.5 \text{ Gb/s/channel}$  under a  $2^{23} - 1$  pseudorandom bit sequence (PRBS) without error ( $< 10^{-13}$  bit-error rate). Fig. 13 shows the eye diagrams observed at different data rates, from  $622 \text{ Mb/s}$  up to  $1.5 \text{ Gb/s}$ . The closing up of the eyes has been mainly limited by our receiver bandwidth.

### III. WDM RECEIVER DESIGN AND FABRICATION

In comparison to the maturity of laser technology, the monolithically integrated WDM receivers seem to be far less developed. Resonant-cavity-enhanced structures have been used to construct  $2 \times 2$  demultiplexing detector arrays at around  $900 \text{ nm}$  [39]. However, the channel spacing has been very large,  $15\text{--}20 \mu\text{m}$ , and the bandwidth is as wide as  $15 \text{ nm}$ . Recently, the authors have demonstrated the first narrow-band monolithically integrated  $1 \times 8$  resonant-cavity photodetector arrays for real-time spectroscopic analysis or parallel demultiplexing of wavelength-encoded channels at  $1.55 \mu\text{m}$  [40]. A novel double-absorber design was developed to avoid position sensitivity related to the cavity standing wave and eliminate the need for *in situ* cavity-mode adjustment. The idea is to set the center-to-center spacing of the two thin QW absorption layers at  $\lambda/4$  so that the field<sup>2</sup>-absorption integral is independent of the position of the absorbers relative to the cavity standing wave. This is especially important for our applications because the cavity modes in an array will be adjusted by post-growth processing over some  $30 \text{ nm}$ , and it is crucial to maintain a reasonable balance between mirror reflections and cavity losses over the whole range in order to obtain a uniform photoresponse. Moreover, in order to reduce crosstalk between channels, these devices were designed with a high- $Q$  cavity by minimizing cavity losses and increasing cavity length to

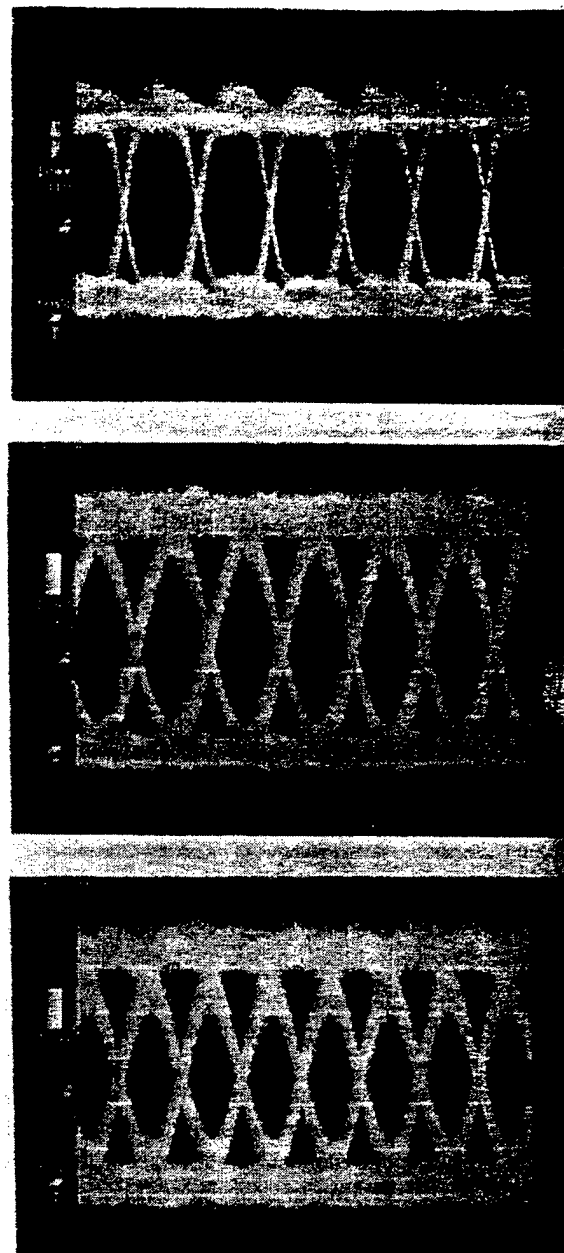


Fig. 13. Eye diagrams observed at different data rates, from  $622 \text{ Mb/s}$  up to  $1.5 \text{ Gb/s}$ .

obtain narrow-band photoresponse. An experimental channel rejection ratio of  $14.5 \text{ dB}$  at  $4 \text{ nm}$  away from the resonant peak has been achieved at  $1.55 \mu\text{m}$  in the lattice-matched  $\text{InGaAs-InAlGaAs-InP}$  material system.

At the same time, we have also demonstrated  $1.55\text{-}\mu\text{m}$  "pie"-shape photodetector arrays for direct-coupled WDM receivers [41]. These pie-shaped devices were arranged within a  $60\text{-}\mu\text{m}$ -diameter circle, just like our VCSEL PIE arrays. Therefore, when the fiber optics is aligned and slightly defocused to the center of the pie array, all eight elements will be equally illuminated with all input wavelengths, but each of them will only pick up the specific channel which lies within its absorption band. A splitting loss of  $13 \text{ dB}$  has been observed in this configuration, which is close to the  $11\text{-dB}$  theoretical value. Based on the same technology, we can construct a



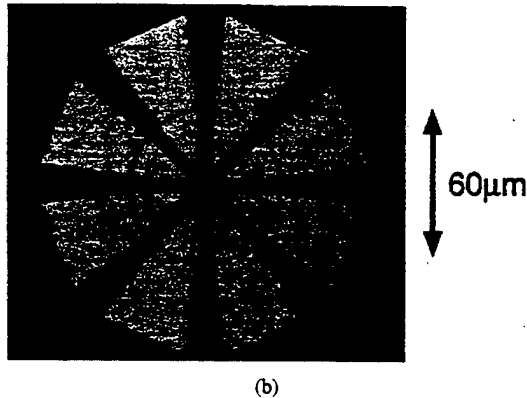
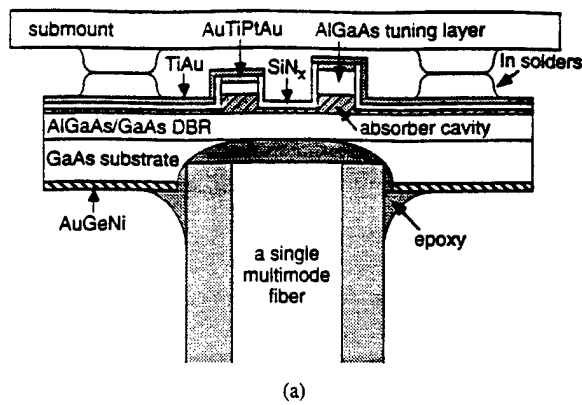


Fig. 14. (a) Schematic cross section of a bottom-illuminated multiple-channel resonant-cavity Schottky photodetector array with the Burrus-type packaging configuration. (b) A photograph of a finished eight-channel "pie"-shaped Schottky photodetector array.

"pie"-shape WDM photodetector arrays at  $0.98 \mu\text{m}$  in the InGaAs–AlGaAs–GaAs material system. Fig. 14(a) shows a schematic cross section of a bottom-illuminated multiple-channel resonant-cavity Schottky photodetector array with the Burrus-type packaging configuration. Fig. 14(b) is a photograph of a finished eight-channel "pie"-shaped photodetector array for  $0.98\text{-}\mu\text{m}$  WDM optical data links. These devices are narrow-band resonant-cavity Schottky photodiodes with the Schottky Au metal as the back mirror and the AlGaAs DBR as the front mirror. Cavity modes for the individual devices can be adjusted by performing anodic oxidation on the i-AlGaAs phase-tuning layers. A detailed description of the processing technique has been reported elsewhere [41]. In the following, we will focus on the various design aspects of narrow-band resonant-cavity photodetector arrays.

Schottky and p-i-n structures are the two common designs for high-performance photodiodes. Fig. 15 shows the refractive index profiles for bottom-illuminated (a) Schottky and (b) p-i-n structures to achieve narrow-band WDM resonant-cavity photodetectors. The phase-tuning layers are i- $\text{Al}_{0.32}\text{Ga}_{0.68}\text{As}$  and p-GaAs for these two cases, respectively. The  $\text{SiO}_2$  layer in the p-i-n design is to prevent Au spiking into the lattice during contact annealing and to increase the reflectivity. From the processing point of view, the Schottky structure is much simpler because the Schottky Au metal itself can be used as the back reflection mirror. However, the interface between the Au Schottky metal and the high Al-content semiconductor

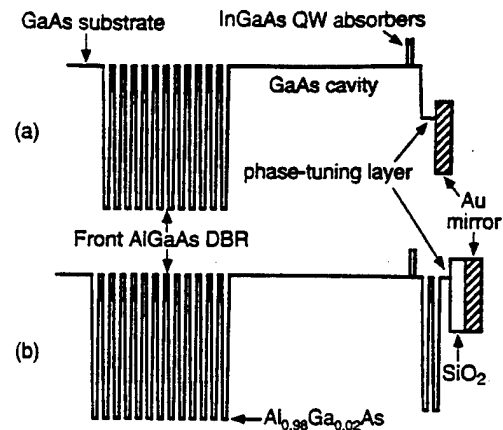


Fig. 15. Refractive index profiles for the bottom-illuminated narrow-band (a) Schottky and (b) p-i-n photodetector designs. The phase-tuning layers are i- $\text{Al}_{0.32}\text{Ga}_{0.68}\text{As}$  and p-GaAs for these two cases, respectively. The  $\text{Al}_{0.98}\text{Ga}_{0.02}\text{As}$  layers in the p-i-n design are for the antiresonant oxide aperture.

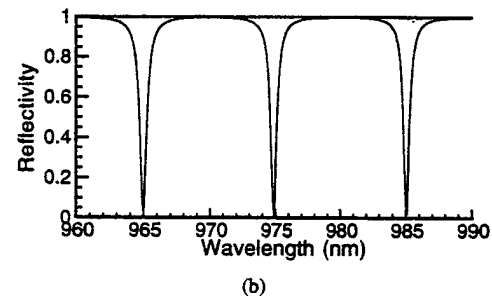
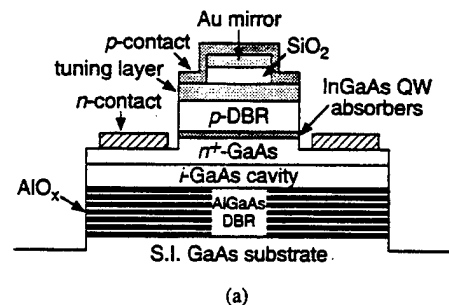


Fig. 16. (a) Schematic device cross section and (b) theoretical reflectivity spectra for the proposed P-i-N photodetector with an antiresonant oxide aperture underneath the ring p-contact to suppress undesired absorption which may cause linewidth broadening in photoresponses. The solid-curve reflection spectra shown from left to right are for positions under the Au back mirror with tuning layer thicknesses of  $0.40$ ,  $0.50$ , and  $0.62\lambda$ , respectively. The dashed curves are for positions under the ring p-contact with the above tuning layer thicknesses.

layer is not very stable. Degradation in photoresponse has been observed in our previous  $\text{In}_{0.52}\text{Al}_{0.48}\text{As}$ –Au devices. Moreover, the photoresponse bandwidth has also been limited by the finite absorption in Au. Therefore, the alternative p-i-n solution becomes much more attractive. In this work, we propose a novel p-i-n resonant-cavity photodetector design with an antiresonant oxide aperture. Fig. 16(a) shows a device schematic for the proposed p-i-n photodetector. Underneath the ring p-contact, the  $\text{Al}_{0.98}\text{Ga}_{0.02}\text{As}$  layers in the front DBR mirror will be oxidized after the mesa etching to increase the DBR reflectivity to almost one. As a result, the undesired

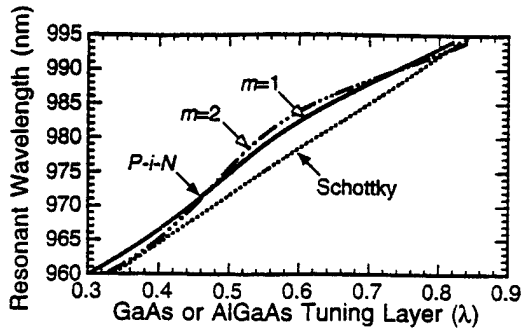


Fig. 17. Theoretical cavity-mode tuning characteristics for the bottom-illuminated Schottky and p-i-n photodetector designs shown in Fig. 15. In the calculation, the back DBR mirror for the p-i-n structure is assumed to be 0.5 period (solid curve,  $m = 1$ ) or 1.5 periods (dash-dotted curve,  $m = 2$ ) for comparison.

absorption underneath the ring p-contact which may cause linewidth broadening in photoresponses can be eliminated over the whole channel span ( $\sim 30$  nm). Fig. 16(b) shows the theoretical reflectivity spectra for positions under the Au back mirror with tuning layer thicknesses of (solid curves, from left to right)  $0.40$ ,  $0.50$ , and  $0.62\lambda$ , respectively. The dashed curves are for positions under the ring p-contact with the same tuning layer thicknesses. As one can see, the undesired absorption outside the central  $\text{SiO}_2$ -Au detection region has been significantly suppressed over the whole wavelength-tuning range we are interested in. However, the wavelength-tuning behavior for the P-i-N design is not linear, for the same reason described earlier in the VCSEL section. Fig. 17 compares theoretical cavity-mode tuning characteristics for the bottom-illuminated Schottky and p-i-n photodetector designs shown in Fig. 15. In this calculation, the back DBR mirror for the p-i-n structure is assumed to be 0.5 period (solid curve,  $m = 1$ ) or 1.5 periods (dash-dotted curve,  $m = 2$ ) and the  $\text{SiO}_2$  layer is 100 nm.

In terms of photoresponse characteristics, it is very desirable to have passbands with flat tops and steep sides. A novel coupled-cavity structure has been proposed earlier to implement this requirement [42]. The idea is to add a low-loss cavity that is optically coupled to the absorptive cavity via an intermediate mirror. Fig. 18(a) shows the refractive index profile of a coupled-cavity Schottky photodiode design. Preliminary experimental result clearly demonstrates the expected coupled-cavity effect. Modeling for an InGaAs-GaAs-AlGaAs design reveals that this new coupled-cavity structure will be able to show a 30-dB channel rejection ratio (in term of optical power) even when the optical channel spacing is as narrow as 1 nm. Fig. 18(b) shows a comparison of the theoretical reflectivity spectra for the single-cavity (both Schottky and p-i-n) and the coupled-cavity (Schottky) structures, where the absorption coefficient for InGaAs QW's is assumed to be  $1.0 \mu\text{m}^{-1}$ .

Contrary to the demand for a high numerical aperture in the transmitter design to reduce modal noise effects, a large numerical aperture in optical fiber will significantly deteriorate the photodetector performance. Fig. 19(a) shows the angular variation of optical power absorption for incident planar waves of different wavelengths for the Schottky design shown in Fig. 15(a) with a normally incident resonant wavelength of

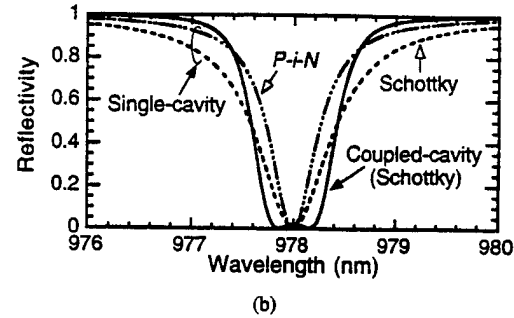
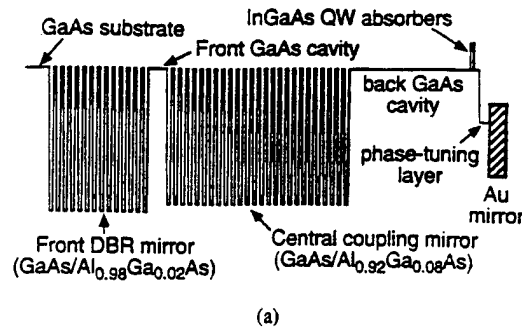


Fig. 18. A novel narrow-band coupled-cavity photodetector design proposed in our earlier work [42]. (a) Refractive index profile of a coupled-cavity Schottky photodiode design. (b) Comparison of the theoretical power reflectivity spectra for the single-cavity (both Schottky and p-i-n) and the coupled-cavity (Schottky) structures.

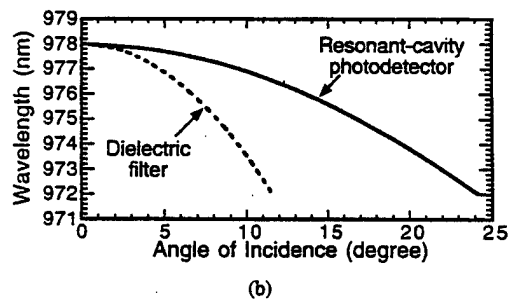
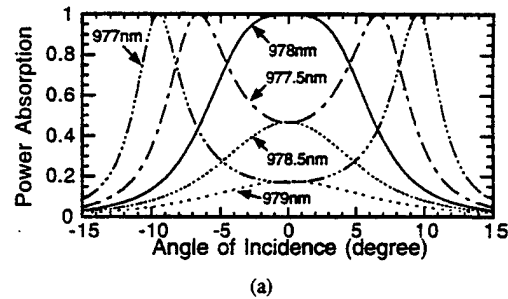


Fig. 19. Effects of numerical aperture of the optical fiber on the photodetector performance. (a) Angular variation of optical power absorption for planar waves of different wavelengths (the number beside each curve) for the Schottky design shown in Fig. 15(a) with the normally incident resonant wavelength of 978 nm. (b) Comparison of the angular variation of the resonant wavelength by using an integrated DBR/semiconductor (solid curve) or a discrete dielectric filter (dash curve).

978 nm. As one can see, the apparent resonant wavelength varies with the incident angle. This effect will broaden the photoresponse and thus limit the minimum channel spacing. Nevertheless, the problem is much more severe for the conventional discrete dielectric filter and photodetector approach.

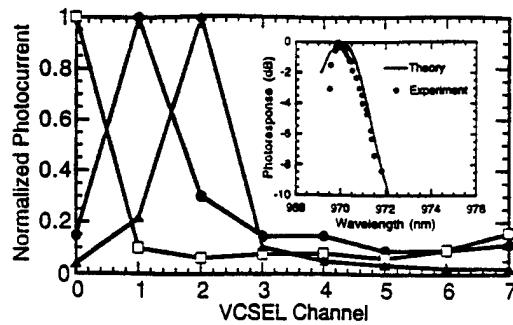


Fig. 20. The measured (normalized) photocurrents for three channels in the optical link built with our VCSEL PIE array and the "pie"-shaped photodetector array. The inset shows the measured data and theoretical photoresponse curves for one of the detector channels.

Fig. 19(b) shows a comparison of the angular variation of the resonant wavelength by using a resonant-cavity photodetector (solid curve) or a  $\text{SiO}_2\text{-SiN}_x$  dielectric filter (dashed curve) design. The resonant-cavity photodetector design can have either dielectric or semiconductor DBR's. As one can see, for the  $62.5\text{-}\mu\text{m}$ -core fiber with a numerical aperture of 0.275, the resonant-cavity photodetector design can allow a much narrower channel spacing than the discrete dielectric filter approach.

Preliminary measurements on an optical link built with our bottom-emitting multiple-wavelength VCSEL array and Schottky photodetector array have been performed. Fig. 20 shows the measured (normalized) photocurrents for three detector channels in the optical link under the illumination of each VCSEL channel. The achieved channel rejection ratio is about 7 dB in photocurrent. The insert shows the measured and theoretical photoresponse curves for one of the detector channels at 970 nm. These response data were taken by thermally tuning the VCSEL wavelength while the theoretical curve was calculated by using the experimental lasing spectrum incorporated with the numerical aperture effect of multimode fiber as discussed earlier. As one can see, the theory matches the data quite well. No high-speed testing has been performed in this link because these first-generation photodetector arrays are rather slow in speed. Further improvement in high-speed design is required for practical applications, such as using a semi-insulating substrate and proton implantation to reduce parasitic capacitance.

Lastly, it is worthwhile to pay attention to the recent progress in the development of monolithically integrated but still individually optimizable VCSEL and photodetector arrays for free-space interconnections [43]. Here, we propose a second approach to build our WDM optical link by using the newly developed multicore fibers [44]. Fig. 21(a) shows a schematic diagram of the proposed link in which a top-emitting multiple-wavelength VCSEL array [16] and a top-illuminated wavelength-selective p-i-n photodetector array are monolithically integrated on the same chip. Fig. 21(b) shows a SEM example of the top-emitting VCSEL PIE arrays. In this system, wavelength-encoded data are transmitted through a single dual-core  $62.5\text{-}\mu\text{m}$ -diameter multimode fiber. The reason to use the top-emitting VCSEL structure is because we can convert a top-emitting multiwavelength VCSEL array

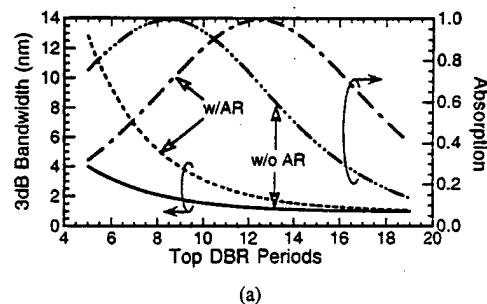
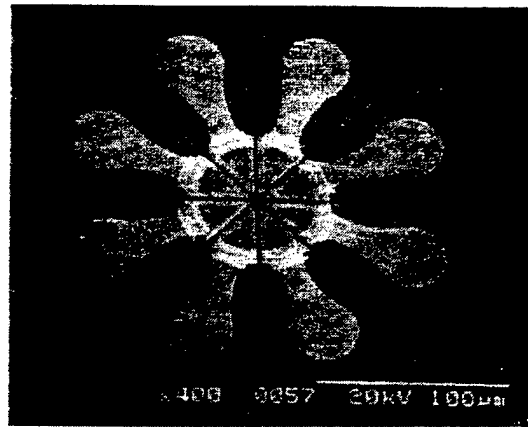
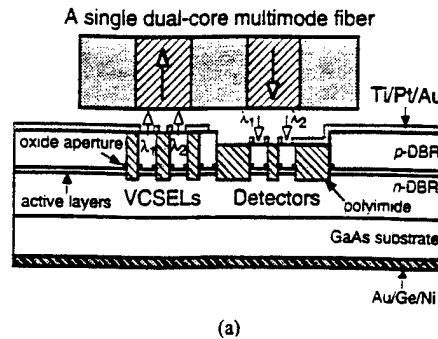


Fig. 21. (a) Schematic cross-section diagram of a proposed alternative WDM optical link in which top-emitting multiple-wavelength VCSEL array and top-illuminated wavelength-selective photodetector array are monolithically integrated on the same chip and butt-coupled to a single dual-core multimode fiber. (b) SEM example of the top-emitting VCSEL PIE arrays. (c) The 3-dB optical bandwidth and cavity absorption as a function of the remaining top DBR periods for the case with or without AR-coating on top of the photodetectors.

into a wavelength-matched WDM photodetector array simply by etching away a few DBR periods out of the top mirror to obtain the desired bandwidth and absorption. Therefore, VCSEL's and detectors can share the same epitaxial structure and even the same anodic oxidation process for wavelength tuning which thus provides "self-aligned" wavelength control. However, the VCSEL-converted photodetectors will have a broader photoresponse bandwidth than the previous described high-Q cavity design. Fig. 21(c) shows the predicted 3-dB optical bandwidth and cavity absorption as a function of the remaining top DBR periods for the case with or without antireflection (AR) coating on top of the photodetectors. The function of this AR coating is to reduce the number of DBR periods to be removed for the given bandwidth and absorption

design. For example, if  $\sim 100\%$  cavity absorption is chosen, six or ten DBR periods have to be removed for the with-AR and without-AR case, respectively. For both cases, the resultant bandwidth will be around 2 nm which is much wider than the 0.5-nm bandwidth in previous p-i-n designs, shown in Fig. 18(b).

Even though the proposed and demonstrated WDM links in this paper have been on the 980-nm wavelength design, it is possible to implement the whole concept onto other wavelengths, such as 850 nm. In this case, the main difficulty is to achieve high-quality epitaxial regrowth over the AlGaAs phase-tuning layers. Moreover, for both VCSEL's and photodetectors, the top-emitting [16] and top-illuminating configurations have to be used to avoid the substantial substrate absorption at 850 nm, which requires much more complicated processing steps. However, it is very helpful to use the transparent indium tin oxide films for the top p-contact electrodes to simplify device processing.

#### IV. CONCLUSION

We have introduced two novel WDM optical data links for low-cost LAN applications. These links utilize monolithically integrated multiple-wavelength VCSEL arrays and narrow-band resonant-cavity photodetector arrays to transmit multiple channels of information simultaneously via one single-core or dual-core multimode fiber. A detailed analysis on the physics and designs of multiple-wavelength VCSEL and narrow-band photodetector arrays has been presented. Preliminary measurement results on our optical link have also been demonstrated. We believe that these WDM optical data links will be powerful solutions for next-generation data communications.

#### ACKNOWLEDGMENT

The authors would like to thank O. Sjolund, E. M. Strzelecka, T. Wipiejewski, and S. Z. Zhang for their help in the device processing and measurement. They also thank K. L. Chen at Hewlett-Packard Company for his helpful and inspiring discussion.

#### REFERENCES

- [1] Y. Sugimoto and K. Kasahara, "Future prospects of VCSELs: Industrial view," in *Proc. IEEE LEOS Summer Top. Meeting-VCL's*, Montreal, PQ, Canada, Aug. 1997, paper MA3, pp. 7-8.
- [2] R. A. Nordin, D. B. Buchholz, R. F. Huisman, N. R. Basavanahally, and A. F. J. Levi, "High performance optical data link array technology," *IEEE Trans. Comp. Hybrids, Manufact. Technol.*, vol. 16, pp. 783-788, Dec. 1995.
- [3] T. Kurokawa, "Vertical-cavity surface-emitting lasers and smart pixels for optical interconnection systems," in *Proc. 9th IEEE LEOS Annu. Meeting*, Boston, MA, Nov. 1996, paper ThA1, vol. 2, pp. 269-270.
- [4] M. Lebby, C. A. Gaw, W. Jiang, P. A. Kiely, P. R. Claisse, and J. Grula, "Key challenges and results of VCSEL's in data links," in *Proc. 9th IEEE LEOS Annu. Meeting*, Boston, MA, Nov. 1996, paper WV2, vol. 2, pp. 167-168.
- [5] N. Tanaka, Y. Arai, H. Takahara, Y. Ando, K. Koyabu, S. Fujita, Y. Akahori, and J. Nishikido, "3.5 Gb/s \* 4 ch optical interconnection module for ATM switching system," in *Proc. 47th Elec. Comp. & Tech. Conf.*, San Jose, CA, May 1997, pp. 210-216.
- [6] K. H. Hahn and K. S. Giboney, R. E. Wilson, J. Stranznicky, E. G. Wong, M. R. Tan, R. T. Kaneshiro, D. W. Dolfi, E. H. Mueller, A. E. Plotts, D. D. Murray, J. E. Maregiano, B. L. Booth, B. J. Sano, B. Madhavan, B. Raghavan, and A. F. J. Levi, "Gigabyte/s data communications with the POLO parallel optical link," in *Proc. 46th Elec. Comp. & Tech. Conf.*, Orlando, FL, May 1996, pp. 301-307.
- [7] Y. Fukashiro, S. Kaneko, A. Oishi, and S. Hanatani, "800 Gbit/s/ch-10 channel fully-integrated low-skew optical modules for optical subsystem interconnections," in *Proc. 9th IEEE LEOS Annu. Meeting*, Boston, MA, Nov. 1996, paper W14, vol. 2, pp. 67-68.
- [8] R. Michalzik, P. Schnitzer, U. Fiedler, D. Wiedenmann, and K. J. Ebeling, "High-bit-rate data transmission with short-wavelength oxidized VCSEL's: Toward bias-free operation," *IEEE J. Select. Topic Quantum Electron.*, vol. 3, pp. 396-404, 1997.
- [9] A. Yuen, K. Giboney, E. Wong, L. Buckman, D. Haritos, P. Rosenberg, J. Stranznicky, and D. Dolfi, "Parallel optical interconnections development at HP Labs," in *Proc. 10th IEEE LEOS Annu. Meeting*, San Francisco, CA, Sept. 1997, paper WX2, vol. 2, pp. 191-192.
- [10] L. J. Norton, F. Carney, R. K. Denton, Jr., J. Faury, H. Geist, D. James, J. H. Knapp, S. Planer, G. Raskin, E. Reyes, J. E. Sauvageau, D. B. Schwartz, R. Stradling, and G. Westbrook, "OPTOBUSTM: A parallel interconnect solution," in *Proc. 10th IEEE LEOS Annu. Meet.*, San Francisco, CA, Nov. 1997, paper WX1, vol. 2, pp. 189-190.
- [11] T. Yoshikawa, S. Araki, K. Miyoshi, Y. Suemura, N. Henmi, T. Nagahori, H. Matsuoka, and T. Yokota, "Skewless optical data-link subsystem for massively parallel processors using 8 Gb/s  $\times$  1.1 Gb/s MMF array optical module," *IEEE Photon. Technol. Lett.*, vol. 9, pp. 1625-1627, 1997.
- [12] T. Wipiejewski, J. Ko, B. J. Thibeault, and L. A. Coldren, "Multiple wavelength vertical-cavity laser array employing molecular beam epitaxial regrowth," *Electron. Lett.*, vol. 32, pp. 340-342, 1996.
- [13] D. L. Huffaker and D. G. Deppe, "Multiwavelength, densely-packed 2  $\times$  2 vertical-cavity surface-emitting laser array fabricated using selective oxidation," *IEEE Photon. Technol. Lett.*, vol. 7, pp. 858-860, 1996.
- [14] A. Golshani, P. O. Kellerman, A. Kock, and E. Gornik, "5-wavelength surface emitting laser diode array based on post growth adjustment of surface mode emission," in *Proc. IEEE LEOS Summer Top. Meeting-WDM Comp. Tech.*, Montreal, Quebec, Canada, Aug. 1997, paper FA2, pp. 61-63.
- [15] B. Lemoff, L. B. Aronson, L. A. Buckman, and D. W. Dolfi, "Low-cost multimode WDM for the local area network," in *Proc. IEEE LEOS Summer Top. Meeting-WDM Comp. Tech.*, Montreal, PQ, Canada, Aug. 1997, paper WC3, pp. 15-16.
- [16] S. Y. Hu, E. R. Hegblom, and L. A. Coldren, "Multiple-wavelength top-emitting vertical-cavity photonic integrated emitter arrays for direct-coupled wavelength-division multiplexing applications," *Electron. Lett.*, vol. 34, pp. 189-190, 1998.
- [17] S. Y. Hu, J. Ko, and L. A. Coldren, "High-performance densely-packed vertical-cavity photonic integrated emitter arrays for direct-coupled WDM applications," *IEEE Photon. Technol. Lett.*, vol. 10, pp. 766-768, June 1998.
- [18] H. Yamada, "Future optical storage in multimedia environment and role of blue lasers," in *Proc. 2th Int. Conf. Nitride Semicond.*, Tokushima, Japan, Oct. 1997, pp. 2-4, planary paper M1-1.
- [19] E. C. Vail, G. S. Li, W. Yuen, and C. J. Chang-Hasnain, "High performance and novel effects of micromechanical tunable vertical-cavity lasers," *IEEE J. Select. Topics Quantum Electron.*, vol. 3, pp. 691-697, 1997.
- [20] W. Yuen, G. S. Li, and C. J. Chang-Hasnain, "Multiple-wavelength vertical-cavity surface-emitting laser arrays," *IEEE J. Select. Topics Quantum Electron.*, vol. 3, pp. 422-428, 1997.
- [21] H. Saito, I. Ogura, and Y. Sugimoto, "Uniform CW operation of multiple-wavelength vertical-cavity surface-emitting lasers fabricated by mask molecular beam epitaxy," *IEEE Photon. Technol. Lett.*, vol. 8, pp. 1118-1120, 1996.
- [22] J. Yoo, J. E. Leight, G. Giaretta, W. Yuen, A. E. Willner, and C. J. Chang-Hasnain, "Experimental demonstration of a four-plane 2-D multiple-wavelength optical interconnection using integrated VCSEL arrays and MQW/DBR detectors," *IEEE Photon. Technol. Lett.*, vol. 9, pp. 1646-1648, 1997.
- [23] G. G. Ortiz, S. Q. Luong, S. Z. Sun, J. Cheng, H. Q. Hou, G. A. Vawter, and B. E. Hammons, "Monolithic, multiple-wavelength vertical-cavity surface-emitting laser arrays by surface-controlled MOCVD growth rate enhancement and reduction," *IEEE Photon. Technol. Lett.*, vol. 9, pp. 1069-1071, 1997.
- [24] K. H. Hahn, M. R. T. Tan, Y. M. Houn, and S. Y. Wang, "Large area multitransverse-mode VCSEL's for modal noise reduction in multimode fiber systems," *Electron. Lett.*, vol. 29, pp. 1482-1483, 1993.
- [25] C. A. Burrus and B. I. Miller, "Small-area double heterostructure AlGaAs electroluminescent diode sources for optical fiber transmission lines," *Opt. Commun.*, vol. 4, pp. 307-309, 1971.

- [26] S. Y. Hu, D. B. Young, S. W. Corzine, A. C. Gossard, and L. A. Coldren, "High-efficiency and low-threshold InGaAs/AlGaAs quantum-well lasers," *J. Appl. Phys.*, vol. 76, pp. 3932-3934, Sept. 1994.
  - [27] E. M. Strzelecka, T. Wipiejewski, J. Ko, B. J. Thibeault, and L. A. Coldren, "Monolithic integration of an array of multiple-wavelength vertical-cavity laser with a refractive microlens for optical interconnections," in *Proc. 9th IEEE LEOS Annu. Meeting*, Boston, MA, Nov. 1996, paper ThA2, vol. 2, pp. 271-272.
  - [28] J. M. Senior, *Optical Fiber Communications—Principles and Practice*. New York: Prentice-Hall, 1985, pp. 98-100.
  - [29] M. R. T. Tan, K. H. Hahn, Y. M. Houng, S. Y. Wang, A. T. Yuen, T. Zhang, and C. Lei, "Design, characteristics and reliability of a large area surface emitting laser for multimode data link applications," in *Proc. 14th IEEE Int. Semicon. Laser Conf.*, Maui, HI, Sept. 1994, pp. 177-178.
  - [30] U. Fiedler, B. Weigl, G. Reiner, R. King, and K. J. Ebeling, "Modal noise in 2.5 Gbit/s data links with oxidized VCSEL's," in *Proc. 9th IEEE LEOS Annu. Meeting*, Boston, MA, Nov. 1996, vol. 2, pp. 71-72, paper W16.
  - [31] J. Heinrich, E. Zeeb, and K. J. Ebeling, "Butt-coupling efficiency of VCSEL's into multimode fibers," *IEEE Photon. Technol. Lett.*, vol. 9, pp. 1555-1557, 1997.
  - [32] N. K. Dutta, S. J. Wang, A. B. Piccirilli, and W. V. Werner, "Crosstalk measurements for a dual emitter laser," *Electron. Lett.*, vol. 26, pp. 1643-1644, 1990.
  - [33] T. Zhang, J. G. Wohlbiel, K. D. Choquette, and N. Tatabaie, "Micro-cavity vacuum-field configuration and the spontaneous emission power," *IEEE J. Select. Topics Quantum Electron.*, vol. 1, pp. 606-615, 1995.
  - [34] G. Heise, "Crosstalk investigation of laser-diode pair," *IEEE Photon. Technol. Lett.*, vol. 2, pp. 97-99, 1990.
  - [35] T. Wipiejewski, D. B. Young, B. J. Thibeault, and L. A. Coldren, "Thermal crosstalk in  $4 \times 4$  vertical-cavity surface-emitting laser arrays," *IEEE Photon. Technol. Lett.*, vol. 8, pp. 980-982, 1996.
  - [36] S. Y. Hu, J. Ko, O. Sjolund, and L. A. Coldren, "Optical crosstalk in monolithically-integrated multiple-wavelength vertical-cavity laser arrays for multimode WDM local-area networks," *Electron. Lett.*, vol. 34, no. 7, pp. 676-678, Apr. 1998.
  - [37] S. Y. Hu, S. Z. Zhang, J. Ko, J. E. Bowers, and L. A. Coldren, "1.5 Gb/s/channel operation of multiple-wavelength vertical-cavity photonic integrated emitter arrays for low-cost multimode wavelength-division multiplexing local-area networks," *Electron. Lett.*, vol. 34, no. 8, pp. 768-770, Apr. 1998.
  - [38] B. Thibeault, "High efficiency vertical-cavity lasers using low-optical loss intra-cavity dielectric apertures," Ph.D. dissertation, Univ. California, Santa Barbara, 1997, pp. 151-152.
  - [39] M. S. Unlu, K. Kishino, J. I. Chyi, L. Arsenault, J. Reed, and H. Morkoc, "Wavelength demultiplexing heterojunction phototransistors," *Electron. Lett.*, vol. 26, pp. 1857-1858, 1990.
  - [40] S. Y. Hu, J. Ko, and L. A. Coldren, "Resonant-cavity InGaAs/InAlGaAs/InP photodetector arrays for wavelength demultiplexing applications," *Appl. Phys. Lett.*, vol. 70, pp. 2347-2349, 1997.
  - [41] ———, "1.55  $\mu\text{m}$  pie-shaped resonant-cavity photodetector arrays for direct-coupled wavelength demultiplexing applications," *Electron. Lett.*, vol. 33, pp. 1486-1488, 1997.
  - [42] S. Y. Hu, E. R. Hegblom, and L. A. Coldren, "Coupled-cavity resonant photodetectors for high-performance wavelength demultiplexing applications," *Appl. Phys. Lett.*, vol. 71, pp. 178-180, 1997.
  - [43] G. G. Ortiz, C. P. Hains, J. Cheng, H. Q. Hou, and J. C. Zolper, "Monolithic integration of  $\text{In}_{0.2}\text{Ga}_{0.8}\text{As}$  vertical-cavity surface-emitting lasers with resonance-enhanced quantum well photodetectors," *Electron. Lett.*, vol. 32, pp. 1205-1207, 1996.
  - [44] B. Rosinski, J. Chi, P. Grosso, and J. L. Bihan, "Using VCSEL's and multicore fiber for multi-channel transmission," in *Proc. IEEE LEOS Summer Top. Meeting-VCL*, Montreal, PQ, Canada, Aug. 1997, pp. 59-60, paper WA4.
- Syn-Yem Hu, photograph and biography not available at the time of publication.
- Jack Ko, photograph and biography not available at the time of publication.
- Eric R. Hegblom, photograph and biography not available at the time of publication.
- Larry A. Coldren, photograph and biography not available at the time of publication.

## **Appendix 3**

# Postgrowth Tuning of Semiconductor Vertical Cavities for Multiple-Wavelength Laser Arrays

A. Fiore, Y. A. Akulova, J. Ko, E. R. Hegblom, and Larry A. Coldren, *Fellow, IEEE*

**Abstract**—Combined lateral-vertical oxidation of AlGaAs is investigated as a means of tuning the resonant wavelength of a semiconductor microcavity after the epitaxial growth. It is shown that this technique can provide arrays with a wavelength spread equal to the cavity's free spectral range with a single postgrowth processing step. Design issues for multiple-wavelength vertical-cavity laser arrays using this postgrowth tuning technique are discussed, comparing the performance of devices with all-semiconductor and partially or totally oxidized Bragg mirrors. Experimental results are presented on arrays with a 48-nm lasing span around 970 nm, using partially and totally oxidized mirrors.

**Index Terms**—Optical fiber devices, quantum-well lasers, semiconductor lasers, surfac-emitting lasers.

## I. INTRODUCTION

WAVELENGTH division multiplexing (WDM) has become a popular approach to increase the data rate in both long- and short-distance optical links. Multiple-wavelength arrays of lasers and detectors are required for WDM systems. Vertical-cavity surface-emitting lasers (VCSEL's) on GaAs substrates are ideally suited as sources in short-haul WDM systems, as densely-packed two-dimensional (2-D) arrays of surface emitters can be easily fabricated. Recently, a compact "pie-shaped" array of VCSEL's direct-coupled to a single multimode fiber has been demonstrated [1]. This opens the way to WDM communication between multiple-wavelength arrays of emitters and detectors coupled to the same fiber [1], [2], eliminating the need for external coupling optics. However, realization of these arrays requires good control of the lasing wavelength over small areas of the epitaxial wafer (typically the area of a multimode fiber,  $\approx \pi(30 \mu\text{m})^2$ ). The lasing wavelength in a VCSEL is determined by the resonant wavelength of the vertical cavity, since only one longitudinal mode exists within the gain bandwidth. A variation in the physical thickness of the cavity can be achieved by varying the growth conditions (e.g., the temperature) over the wafer [3], or by using masked molecular beam epitaxy [4]. However, these techniques are difficult to apply to densely packed arrays with arbitrary wavelength placement and also require unconventional growth techniques. On the other hand, the physical length of the cavity can be varied by anodic oxidation and etching of a controlled thickness of semiconductor [5]. This technique was used to

fabricate pie-shaped arrays [1] and requires an interruption of the epitaxial growth at the end of the cavity, a multistep etching, and then a regrowth of the top mirror, which makes it questionable for low-cost device production. Moreover, this technique is difficult to apply to arrays in the 850-nm band, for use with Si detectors, since regrowth over AlGaAs would be needed. Recently, it has been shown [6] that "over-oxidation" of GaAs-Al-oxide distributed Bragg reflectors (DBR's) results in a shift of the cavity wavelength. This is attributed to the change of phase shift upon reflection as more semiconductors are transformed into the low-index oxide. Independently, others [7] have demonstrated the use of lateral-vertical wet oxidation to obtain a tapered profile of an Al-oxide layer. Combining these two observations, we have proposed and demonstrated [8] the use of lateral-vertical oxidation to change the resonant wavelength of a semiconductor optical cavity. This principle is shown in Fig. 1(a). A high Al-composition AlGaAs layer (e.g., AlAs, "supply layer") is laterally oxidized from the etched side of a mesa in a water vapor atmosphere at 400 °C–500 °C [9]. This provides a path for a rapid lateral supply of the oxidizing species. An adjacent  $\text{Al}_x\text{Ga}_{1-x}\text{As}$  ( $x \approx 0.7\text{--}0.9$ ) "tuning layer" is then oxidized vertically, at a (slower) rate controlled by the Al composition and by the oxidation temperature. The change in the refractive index from semiconductor ( $n \approx 3.0\text{--}3.6$ ) to oxide ( $n \approx 1.6$ ) determines a variation of the optical thickness and, hence, of the cavity wavelength. Note that the role of the supply layer is essentially to provide a remote access to the cavity after the epitaxial growth of both DBR mirrors. The amount of tuning is controlled by the position of the tuning layer and its composition, by the temperature and duration of the oxidation, and by the distance of the device from the etched side. Since the combination of lateral and vertical oxidation naturally provides tapering of the oxidized profile, devices at different distances from the same etched side have different resonant wavelengths. Alternatively, oxidation mesas with varying size can be centered on the devices [Fig. 1(b)]. In this case, oxidation proceeds from the two sides, resulting in a faster supply of oxidant to the center and faster tuning. In both cases, multiple-wavelength arrays are realized in a single postgrowth processing step.

This paper is organized as follows. In Section II, we present measurements of the resonant wavelength shift for different oxidation conditions. The design of multiple-wavelength VCSEL structures is described in Section III. It is shown that the DBR mirror bandwidth determines the total tuning range and the uniformity of device characteristics. All-semiconductor

Manuscript received July 9, 1998; revised December 4, 1998. This work was supported by the Air Force Office of Scientific Research and by DARPA. The authors are with the Electrical and Computer Engineering Department, University of California at Santa Barbara, Santa Barbara, CA 93106 USA.  
Publisher Item Identifier S 0018-9197(99)02534-8.

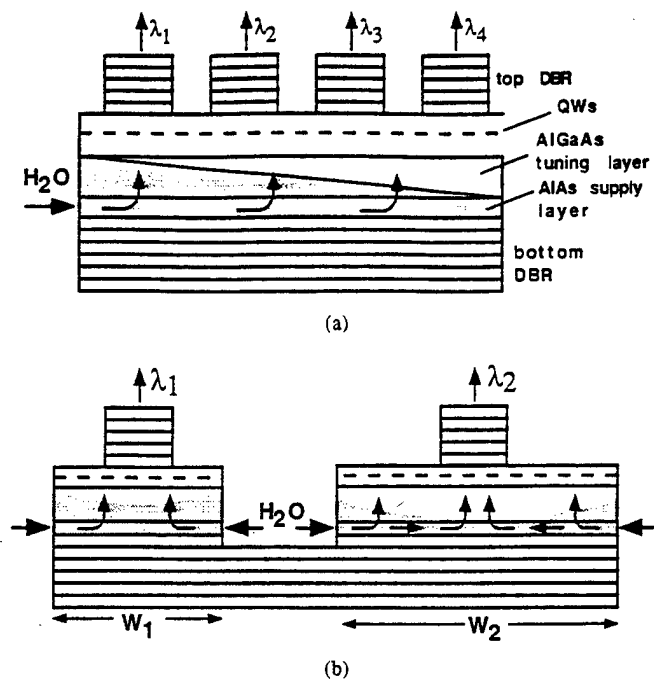


Fig. 1. Schematics (not to scale) of wavelength tuning in a VCSEL by using lateral-vertical oxidation. The water vapor is supplied to the tuning layer inside the cavity by the lateral oxidation of the supply layer. (a) Different devices in the array are positioned at varying distances from a common edge ( $\lambda_1 < \lambda_2 < \lambda_3 < \lambda_4$ ). (b) Each device is oxidized from the two sides of a stripe ( $\lambda_1 < \lambda_2$ ).

DBR's are compared to totally or partially oxidized DBR's. In Section IV, results on multiple-wavelength VCSEL arrays are presented. Problems related to the use of oxidized DBR's are also discussed.

## II. WAVELENGTH TUNING EXPERIMENTS

The sample used to measure the wavelength shift is a top-emitting VCSEL structure and consists of a 24.5-period GaAs- $\text{Al}_{0.9}\text{Ga}_{0.1}\text{As}$  bottom DBR, a  $4\lambda_0$ -cavity described below, and a top DBR composed of two periods of GaAs-AlAs and eight periods of GaAs- $\text{Al}_{0.9}\text{Ga}_{0.1}\text{As}$  Bragg pairs. The two AlAs layers are designed to be  $\lambda_0/4$  thick after oxidation of AlAs. The center wavelength of the DBR stopband is  $\lambda_0 = 980$  nm. The choice of the partially oxidized top mirror will be justified in Section III. The cavity is composed of, from the bottom to the top, an 86.1-nm-thick AlAs oxidant supply layer, a 243.9-nm-thick  $\text{Al}_{0.7}\text{Ga}_{0.3}\text{As}$  tuning layer, one GaAs- $\text{Al}_{0.9}\text{Ga}_{0.1}\text{As}$  Bragg pair, a  $3/4\lambda_0$  GaAs n-contact layer, a  $\lambda_0/4$   $\text{Al}_{0.9}\text{Ga}_{0.1}\text{As}$  layer, a  $1\lambda_0$  active region with three 80-nm  $\text{In}_{0.18}\text{Ga}_{0.82}\text{As}$ -GaAs quantum wells at the center, a 27-nm-thick  $\text{Al}_{0.98}\text{Ga}_{0.02}\text{As}$  layer (to be partially oxidized) for current aperturing, and a  $3/4\lambda_0$  p-GaAs contact layer (see Fig. 9 for schematics of the VCSEL structure). All interfaces between GaAs and a layer to be oxidized are linearly graded to improve the mechanical stability. The tuning layer is designed so that the  $\text{Al}_{0.7}\text{Ga}_{0.3}\text{As}$  and the oxide form  $\lambda_0/2$  and  $\lambda_0/4$  layers, respectively, when the  $\text{Al}_{0.7}\text{Ga}_{0.3}\text{As}$  is vertically oxidized by 80 nm. Fig. 2 shows the calculated resonant wavelength as a function of the vertically oxidized thickness  $T_{\text{oxide}}$ , with the two GaAs-AlAs pairs in the top DBR oxidized

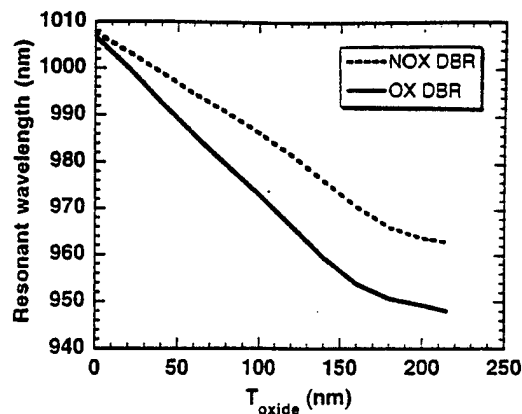


Fig. 2. Calculated resonant wavelength as a function of the vertically oxidized thickness in a VCSEL cavity with two oxidized (continuous line) and unoxidized (dashed line) DBR periods.

(continuous line) and unoxidized (dashed line). We assume  $n_{\text{oxide}} = 1.6$  and 12% linear contraction in the thickness of the oxidized layers [10]. The amount of tuning varies inversely with the cavity length. Oxidation of the two DBR pairs results in a shorter cavity length (due to the higher index contrast), hence, in larger tuning. However, in this experiment, in order to accurately measure the tuning due to the oxidation of the  $\text{Al}_{0.7}\text{Ga}_{0.3}\text{As}$  layer, we protect the top mirror and the aperture layer from oxidation. This is because we found that oxidation of the graded regions contiguous to these layers contributes additional tuning, as already shown in [6]. Therefore, the sample is prepared in the following way. First, stripes of varying widths are reactive-ion-etched down to the n-type GaAs contact. A 240-nm-thick  $\text{SiN}_x$  layer is then deposited in two steps to prevent oxidation of the exposed layers [11]. We found that plasma-enhanced chemical vapor deposition at high temperature (350 °C) provides a  $\text{SiN}_x$  which is impermeable to the water vapor in the oxidation furnace and can be used for protection against wet oxidation. A set of larger stripes, centered on the previous ones, is then etched down into the bottom DBR in order to expose the supply layer. Immediately before oxidation, a 30-s dip in  $\text{NH}_4\text{OH}:\text{H}_2\text{O}$  (1:10) is used to remove any native oxide formed by atmospheric hydrolysis. The sample is then oxidized at 465 °C, in a water-vapor atmosphere created by bubbling  $\text{N}_2$  at 1.7 l/min in water at 80 °C [9].

The resonant wavelength is measured by focusing a tunable Ti:sapphire beam to an  $\approx 4\text{-}\mu\text{m}$ -diameter spot and looking at the power transmitted through the cavity. Due to the spatial and angular extension of the probe beam, the spectral resolution (full-width at half-maximum (FWHM) of the transmission peak) is about 3 nm. Two different regimes are studied, depending on whether or not the stripes are completely oxidized laterally. When the lateral oxidation is incomplete, the oxidant supply for vertical oxidation comes from only one edge [see Fig. 1(a)]. Fig. 3 shows the wavelength shift measured in two samples oxidized for 35 min (squares) and 71 min (dots), as a function of the distance from the etched edge where the lateral oxidation starts. The resonant wavelength cannot be measured in the first tens of micrometers next to the etched edge, due to the unwanted lateral oxidation of the



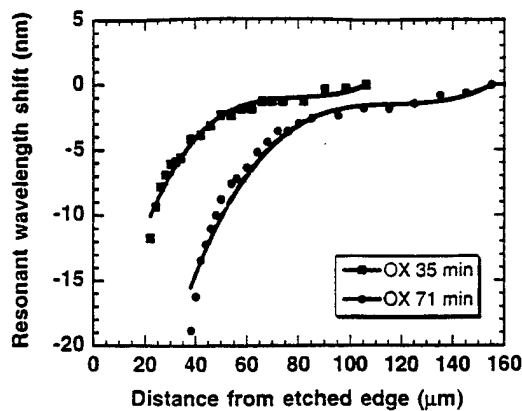


Fig. 3. Measured resonant wavelength shift as a function of the distance from the oxidation edge, for samples oxidized at 465 °C for 35 min (squares) and 71 min (dots). The shift is defined with respect to the resonance at the oxidation front. The continuous lines are third-order polynomial fits.

$\text{Al}_{0.9}\text{Ga}_{0.1}\text{As}$  layers in the bottom mirror, which changes the cavity resonance. The wavelength shift is defined with respect to the resonant wavelength at the oxidation front, where the vertical oxidation is negligible. Since, for  $\Delta\lambda < 30$  nm, the dependence of the wavelength shift on the oxidized thickness is approximately linear (Fig. 2), the profile shown in Fig. 3 also represents, with a change in sign, the tapering of the oxide layer inside the tuning layer. The oxidized profile is nonlinear and can be fitted by third-order polynomials (continuous lines in Fig. 3). Although we do not have a model able to predict this dependence, several factors contribute to the nonlinear tapering. First, lateral oxidation is strongly diffusion-limited for the oxidation times of interest. The measured lateral oxidation kinetics of the supply layer is well fitted by Deal and Grove-type kinetics [12]

$$x_0^2 + Ax_0 = Bt \quad (1)$$

where  $x_0$  is the laterally oxidized distance and  $t$  is the time, with  $A = 36 \mu\text{m}$  and  $B = 415 \mu\text{m}^2/\text{min}$ . On the other hand, we expect the vertical oxidation to be reaction-limited due to the very small reaction rate for the  $\text{Al}_{0.7}\text{Ga}_{0.3}\text{As}$ . The vertically oxidized thickness  $T_{\text{oxide}} = y(x, t)$  is equal to the vertical reaction rate integrated over the time the layer is exposed to the vertical oxidation

$$u(x, t) = \int_{t_0(x)}^t \frac{k_y}{N_1} C(x, t') dt' \quad (2)$$

where  $k_y$  is the vertical reaction rate [12],  $N_1$  is the number of oxidant molecules incorporated into a unit volume of the oxide layer,  $C(x, t)$  is the oxidant concentration at point  $x$ , and  $t_0(x)$  is the time necessary for the lateral oxidation to reach point  $x$ . However, since the lateral oxidation rate is limited by the transport of oxidant to the oxidation front, the vertical oxidation, acting as a trap for the oxidant moving laterally in the supply layer, will slow down the lateral oxidation and change the concentration profile  $C(x)$  from the linear dependence of the 1-D case. This nonlinear concentration profile, as determined by the interplay between lateral and vertical oxidation, produces, through (2), the oxidized thickness tapering shown in Fig. 3.

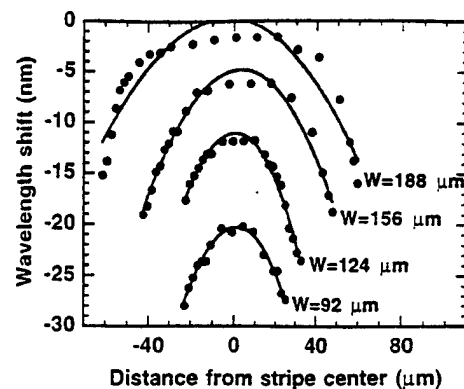


Fig. 4. Measured resonant wavelength shift in oxidized stripes of width  $W$ , as a function of the distance from the stripe center, for a sample oxidized 35 min at 465 °C. The continuous lines are parabolic fits.

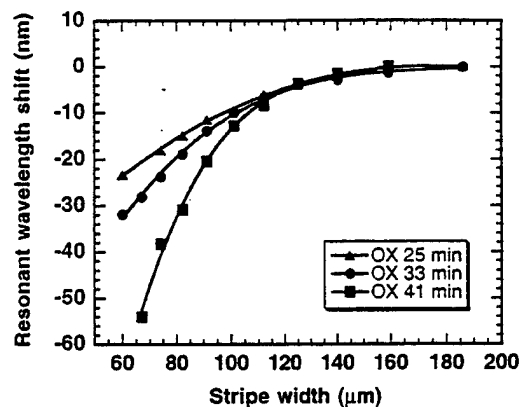


Fig. 5. Wavelength shift measured in the center of the stripe as a function of the stripe width  $W$  for different oxidation times. The oxidation temperature is 465 °C. The continuous lines are third-order polynomial fits.

A second regime is established when the oxidation fronts from the two sides of the stripes join in the center [see Fig. 1(b)]. From this point on, the oxidant concentration profile is determined uniquely by the vertical oxidation. Fig. 4 shows the wavelength shift measured as a function of the distance from the center of the stripe for different stripe widths  $W$ , in a sample oxidized for 35 min at 465 °C. The wavelength shift is defined with respect to the resonant wavelength measured at the oxidation front in a nearby incompletely oxidized stripe. The continuous lines are parabolic fits. As the stripe width gets much smaller than the laterally oxidized distance, the tapering profile becomes well represented by a parabolic law. This may be interesting in view of the realization of intracavity lenses [13], [14] using this lateral-vertical oxidation process. Also note that, for a given oxidation time and distance from the edge, much larger tuning can be achieved by supplying the oxidant from two sides instead of just one. Intuitively, this happens because, when the lateral oxidation is incomplete, a large part of the oxidant supply is consumed by the lateral oxidation instead of contributing to the tuning.

In view of device applications, it is particularly important to optimize the wavelength shift in the center of the stripes. Fig. 5 shows the wavelength shift measured in the center as a function of the stripe width  $W$  for different oxidation

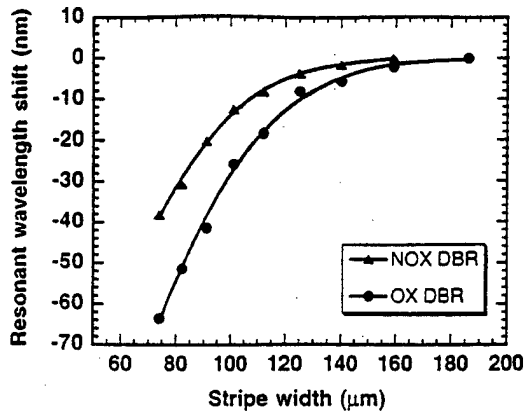


Fig. 6. Wavelength shift measured in the center of the stripes in a sample oxidized 41 min at 465 °C, before (triangles) and after (dots) oxidation of the two AlAs pairs in the top DBR.

times. The continuous lines are third-order polynomial fits. The maximum wavelength shift is 20% larger than the value predicted by the simulation (Fig. 2). This is probably due to more contraction in the oxidized thickness or lower refractive index than assumed. Note that, although the wavelength dependence on the stripe width is nonlinear, linearly spaced wavelengths can be obtained by choosing an appropriate stripe width sequence in the array.

Next, we analyze the effect of the oxidation of the two AlAs periods in the top DBR on the tuning characteristics. To do so, we use a separate process as a first step toward a complete VCSEL fabrication. Circular mesas, with diameters varying from 3 to 15  $\mu\text{m}$ , are first defined by etching down through the top DBR to the GaAs p-contact layer. Larger mesas, aligned with the existing ones, are then etched down to the n-contact layer.  $\text{SiN}_x$  is deposited as before and stripes, centered on the mesas, are defined by etching down into the bottom DBR. The sample is then oxidized for 41 min at 465 °C to provide the tuning.  $\text{SiN}_x$  is removed by  $\text{CF}_4$  plasma etching and a second oxidation is performed at 435 °C for 8 min. During this time, the Bragg periods are completely oxidized, whereas the aperture oxidation front does not reach inside the inner mesa (i.e., it does not influence the optical mode). Due to the shorter duration and lower temperature, this second oxidation should result in a negligible additional vertical oxidation of the tuning layer. Fig. 6 shows the wavelength shift measured before and after the second oxidation. As predicted by the simulations, the wavelength shift is enhanced by oxidizing the AlAs layers in the top DBR. This experiment demonstrates the effect of effective cavity length on tunability, which was theoretically pointed out in [15].

### III. MULTIPLE-WAVELENGTH VCSEL DESIGN

The goal in the design is to obtain characteristics as uniform as possible over the desired wavelength range. We will consider a general structure for a top-emitting double-intracavity contacted VCSEL. This is composed of a bottom DBR, an 86.1-nm-thick AlAs oxidant supply-layer, a 243.9-nm-thick  $\text{Al}_{0.7}\text{Ga}_{0.3}\text{As}$  tuning layer, a  $3/4\lambda_0$  GaAs n-contact layer, a  $\lambda_0/4$   $\text{Al}_{0.9}\text{Ga}_{0.1}\text{As}$  layer, a  $1\lambda_0$  active region with three 80-

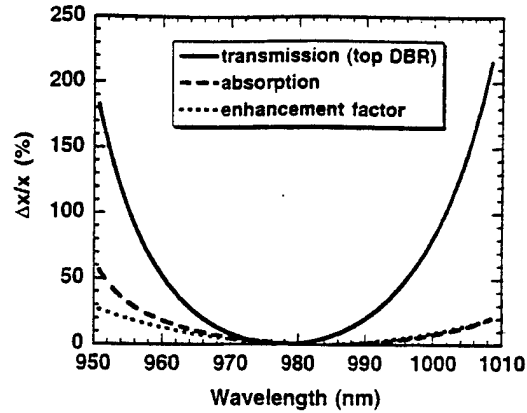


Fig. 7. Calculated relative change in top DBR transmission, absorption, and enhancement factor, as a function of wavelength, in a VCSEL with all-semiconductor DBR's.

nm  $\text{In}_{0.18}\text{Ga}_{0.82}\text{As}$ -GaAs quantum wells at the center, a  $\lambda_0/4$   $\text{Al}_{0.98}\text{Ga}_{0.02}\text{As}$  aperture layer, a  $3/4\lambda_0$  p-GaAs contact layer, and a top DBR. This structure is similar to the one used for the wavelength shift measurements, except that the separation Bragg pair between the tuning layer and the active region are absent. This separation period only reduces the tuning, which may be useful if a limited wavelength span is needed, but it does not affect performance at a given wavelength. The bottom DBR reflectivity is designed much to be higher than the top one over the wavelength range of interest. Let us first analyze the factors which limit uniformity of threshold gain in a VCSEL with all-semiconductor ( $\text{GaAs}-\text{Al}_{0.9}\text{Ga}_{0.1}\text{As}$ ) DBR mirrors. The threshold gain is proportional to the sum of transmission and absorption losses and inversely proportional to the enhancement factor. Its relative change with wavelength is therefore determined by the changes in these quantities. Fig. 7 shows the corresponding relative changes ( $\Delta x/x$ ) as a function of wavelength. We assume an absorption coefficient of  $22\text{ cm}^{-1}$  in the p-contact layer and in the aperture,  $10\text{ cm}^{-1}$  in the n-contact, and  $3\text{ cm}^{-1}$  in the undoped regions. The change in transmission through the unoxidized top (output) DBR dominates the other factors and hence limits the threshold gain uniformity. This also has an important consequence on the structure design. The reflection at the  $\text{Al}_{0.7}\text{Ga}_{0.3}\text{As}$ -oxide interface in the tuning layer is out of phase with the reflection from the bottom DBR for  $\lambda \neq \lambda_0$ . This strongly reduces the bottom DBR reflectivity out of resonance. Therefore, the mirror next to the tuning layer should never be chosen as the output mirror, which limits the threshold uniformity. Reversing the mirror order in the previous structure (i.e., making it bottom-emitting) results in a relative threshold variation 5 times higher in the same wavelength range.

In order to increase the mirror bandwidth, a GaAs-(Al oxide) DBR can be used [11], [16]. As already mentioned (Fig. 6), the use of an oxidized DBR presents the additional benefit of reducing the effective cavity length and thus results in a wider wavelength range. Fig. 8 shows the calculated percent change in threshold gain,  $\Delta g_{th}/g_{th}$ , for the reference VCSEL cavity, in the case of (a) all-semiconductor 18-period top and 35-period bottom DBR's (dotted line), (b) 8-period semiconductor+2-period oxidized top and 35-period

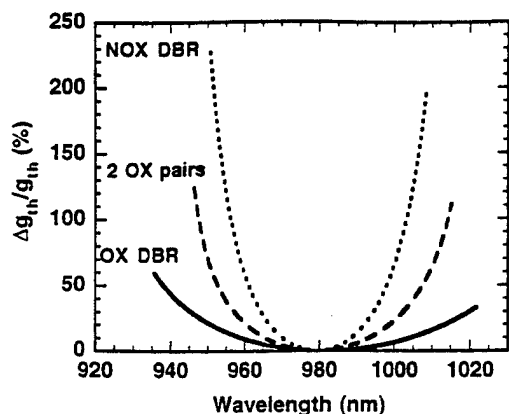


Fig. 8. Calculated relative change in threshold gain,  $\Delta g_{th}/g_{th}$ , for (a) all-semiconductor 18-periods top and 35-period bottom DBR's ("NOX DBR," dotted line), (b) 8-period semiconductor+2-period oxidized top and 35-period semiconductor bottom DBR's ("2 OX pairs," dashed line), and (c) all-oxidized 4-period top and 7-period bottom DBR's ("OX DBR," continuous line).

semiconductor bottom DBR's (dashed line), (c) all-oxidized 4-period top and 7-period bottom DBR's (continuous line). The number of periods is chosen to keep the peak reflectivity and the differential efficiency comparable for the different designs. Note that, for the structure with completely oxidized DBR's, the threshold uniformity is no longer limited by mirror transmission but rather by the variation in absorption losses. The advantage of using oxidized DBR's is apparent from Fig. 8. The choice will be determined by the desired total wavelength span. Since fully oxidized DBR's tend to suffer from mechanical and thermal instability, the use of a hybrid top DBR with only two oxidized periods may prove optimal if a wavelength range of 40–50 nm is sufficient. An alternative solution is, of course, the use of all-semiconductor chirped DBR's.

#### IV. DEVICE RESULTS

The results from two VCSEL structures are compared. One structure uses hybrid oxide–semiconductor mirrors, and the other uses all oxidized DBR's. Both use the standard cavity structure described above, with an  $\text{Al}_{0.7}\text{Ga}_{0.3}\text{As}$ – $\text{AlAs}$  tuning section, a bottom Si-doped ( $2 \times 10^{18} \text{ cm}^{-3}$ ) and a top Be-doped ( $2 \times 10^{18} \text{ cm}^{-3}$ ) contact layers, and a  $1\lambda_0$  active region with three 80-nm  $\text{In}_{0.18}\text{Ga}_{0.82}\text{As}$ – $\text{GaAs}$  QW's. The first structure, also used for the wavelength tuning experiments described in Section II, has one separation Bragg pair between the tuning layer and the bottom contact layer and uses a 24.5-period  $\text{GaAs}$ – $\text{Al}_{0.9}\text{Ga}_{0.1}\text{As}$  bottom DBR and a hybrid 8-period  $\text{GaAs}$ – $\text{Al}_{0.9}\text{Ga}_{0.1}\text{As}$  and 2-period (next to the cavity)  $\text{GaAs}$ –(Al oxide) top DBR. It has a calculated 58-nm wavelength range, a threshold gain varying from 560 to  $1770 \text{ cm}^{-1}$ , and a differential efficiency from 30% to 60% over this range. The photoluminescence peak is at 976 nm. Fabrication starts with etching of two concentric circular mesas to expose the p- and n-contact layers,  $\text{SiN}_x$  deposition as described above, and etching of stripes with varying widths for the tuning. The first oxidation is performed at  $465^\circ\text{C}$  for 40 min, then  $\text{SiN}_x$  is etched and the sample is oxidized again at  $435^\circ\text{C}$  for 16

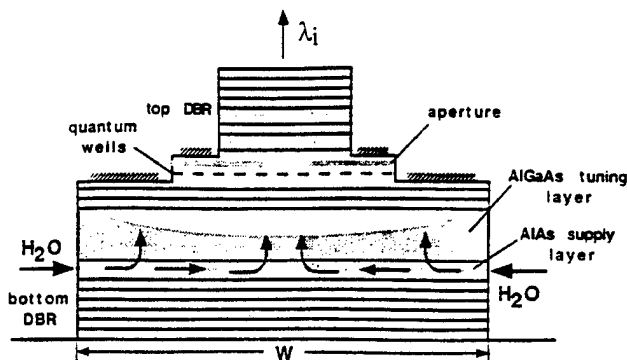


Fig. 9. Schematic of a processed VCSEL using two oxidized periods in the top DBR.

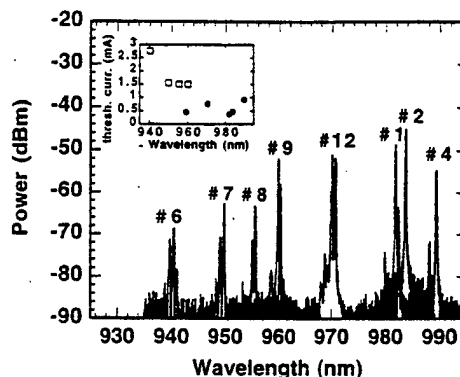


Fig. 10. Measured lasing spectra of VCSEL's with two oxidized periods in the top DBR. The peaks are numbered corresponding to the stripe width number, #1 being the smallest ( $W = 60 \mu\text{m}$ ) and #12 the largest ( $W = 200 \mu\text{m}$ ). Inset: threshold current as a function of wavelength. Output from some devices (empty squares) is taken from the bottom, due to a gold layer left on the top of the pillars.

min. This completely oxidizes the two  $\text{AlAs}$  layers in the top DBR and leaves an unoxidized channel (6–8  $\mu\text{m}$  diameter) in the aperture layer for current flow. P-metal ( $\text{Au-Zn-Au}$ ) and n-metal ( $\text{Ni-Ge-Au-Ni-Au}$ ) are then evaporated on the corresponding contact layers. In order to avoid thermal stress in thick oxide layers, the contacts were not annealed. Fig. 9 shows a schematic of the processed device.

The devices were tested at room temperature under dc electrical pumping. Fig. 10 shows lasing spectra from devices having different stripe widths. The peaks are numbered corresponding to the stripe width, #1 being the smallest ( $W = 60 \mu\text{m}$ ) and #12 the largest ( $W = 200 \mu\text{m}$ ). Since the devices were processed on a piece of the wafer away from the center, the wavelength of peak DBR reflectivity is shifted to  $\lambda_0 = 951 \text{ nm}$ . Fig. 11 shows the net wavelength shift (with respect to the largest stripe) as a function of the stripe width  $W$ . A small gradient in resonant wavelength (1 nm/device), due to growth, is subtracted to give the net tuning due to oxidation. As expected, the lasing wavelength decreases with decreasing stripe width. However, for  $W < 80 \mu\text{m}$ , the devices start lasing in the longer wavelength mode, which is closer to the gain peak. The mode hopping takes place in this case due to misalignment of the gain peak with the center of the tuning range. A net 48-nm span is obtained by exploiting the

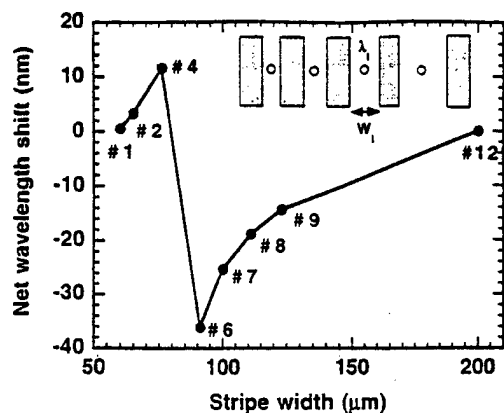


Fig. 11. Measured net wavelength shift as a function of stripe width. The peaks are numbered corresponding to the stripe width number. Inset: schematics of stripe patterning for wavelength tuning. Circles and gray regions represent lasers and etched stripes, respectively.

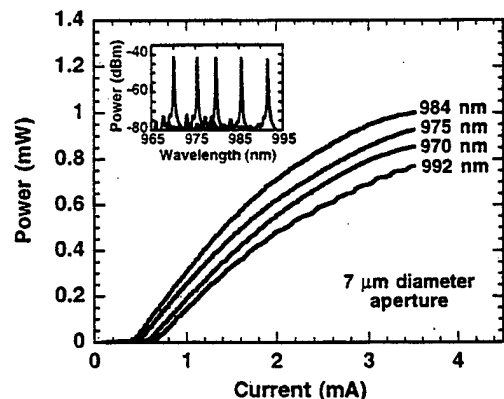


Fig. 12. Light-current characteristics of VCSEL's with two oxidized periods in the top DBR. Inset: corresponding lasing spectra. The spectra were taken at 1.5 times threshold.

two lasing modes. Note that the cavity's free spectral range is an upper limit to the total wavelength span. This further demonstrates the importance of minimizing the cavity effective length by using oxidized mirrors. The inset in Fig. 10 shows the threshold currents for 6–8-μm-diameter apertures. Due to a gold layer left on the top of the pillar, some of the devices present high threshold currents (empty squares). Differential efficiencies are correspondingly low.

In a second processing run, optimized processing and better alignment with the gain peak provided threshold currents <0.65 mA and differential efficiencies >30% over a 22-nm wavelength span. Fig. 12 shows dc light-to-current characteristics at room temperature. In the inset, the spectra for different stripe widths are shown. The threshold currents (dots) and differential efficiencies (squares) are plotted versus wavelength in Fig. 13 for a 7-μm-diameter aperture. The decrease in differential efficiency away from the center wavelength is due to an insufficient number of periods in the bottom DBR. Away from resonance, increased transmission through the all-semiconductor bottom DBR decreases the differential efficiency and increases the threshold gain. This can be solved by using a larger number of periods or an oxidized DBR.

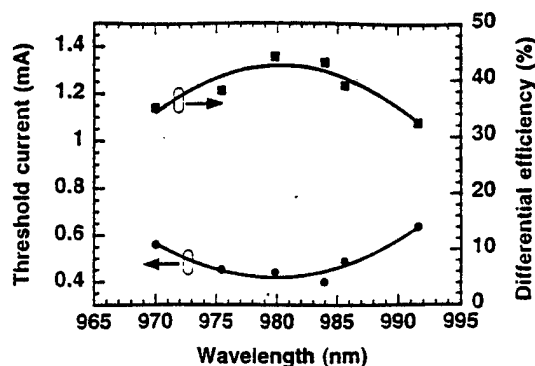


Fig. 13. Threshold current (dots, left axis) and differential efficiency (squares, right axis) as a function of wavelength. The continuous lines are guides to the eye.

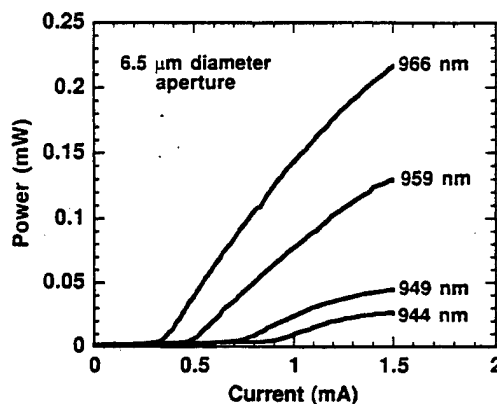


Fig. 14. Light-current characteristics of multiple-wavelength VCSEL's with totally oxidized DBR's.

A second structure uses all-oxidized four-period top- and seven-period bottom DBR's. Linear grading is used at each interface to improve mechanical stability. In order to maximize the total wavelength span, this structure has no separation period between the tuning layer and the cavity. This results in an 85-nm-calculated wavelength span, with the corresponding <60% threshold gain variation shown in Fig. 8. Processing is similar to the previous sample; however, the duration of the first (tuning) oxidation is reduced to 25 min. This is because, for longer times, the smallest stripes become unstable and peel off due to thermal stress during the second oxidation. This is consistent with previous reports [6]. In the same way as the tuning layer is vertically oxidized, oxidation also proceeds through the grading layers in the bottom DBR and eventually gets to the interface with GaAs. At this point, the layers become mechanically unstable [6]. This is probably due to the sharp interface between the oxides formed from AlAs and GaAs [17].

The devices lase over a 22-nm wavelength span around 955 nm. Fig. 14 shows light-current characteristics for 6.5-μm-diameter devices, taken at 16 °C under dc electrical bias. The corresponding threshold currents (dots) and differential efficiencies (squares) are plotted in Fig. 15. The differential efficiency strongly decreases toward shorter wavelengths, with a corresponding increase in threshold current. We attribute

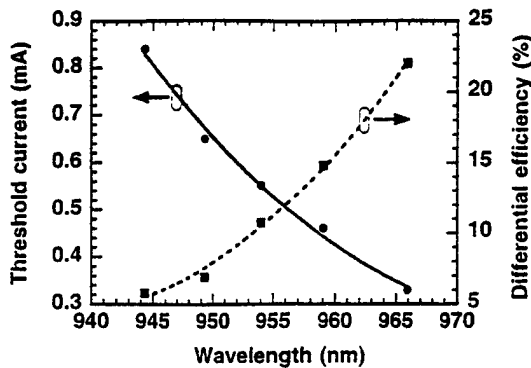


Fig. 15. Threshold current (dots, left axis) and differential efficiency (squares, right axis) as a function of wavelength, for a VCSEL with totally oxidized DBR's. The lines are guides to the eye.

this behavior to increasing losses in the over-oxidized bottom DBR. Losses in the near-infrared were already observed in oxidized multilayers [18] and attributed to mid-gap levels produced by As incorporation in (Al)GaAs. This effect may become more critical as the layers are subject to longer over-oxidation, as is the case with the smaller stripes. An additional source of high threshold current is the large misalignment with the gain peak, due to unoptimized growth.

These experiments show that, in order to get better performance from the all-oxidized DBR VCSEL array, over-oxidation of the bottom DBR should be avoided. This is possible by using a higher Al content in the AlGaAs tuning layer, which will result in a faster vertical oxidation rate and release the need for long oxidation times. Using lower oxidation temperatures was also observed [19] to reduce the optical loss.

## V. CONCLUSIONS

We have shown that lateral-vertical oxidation can be used to tune the resonant wavelength of a semiconductor cavity after the epitaxial growth. This allows the fabrication of mask-defined multiple-wavelength arrays of lasers and resonant detectors using a single epitaxial growth on a conventional substrate. We have studied the kinetics of this process and demonstrated a 64-nm shift in the resonant wavelength. The performance of multiple-wavelength arrays has been shown to be limited by the bandwidth of the output mirror, and the use of partially or totally oxidized DBR's has been analyzed. A VCSEL array with a 48-nm lasing span was demonstrated. Threshold currents were <0.65 mA and differential efficiencies >30% over a 22-nm span. A multiple-wavelength array with totally oxidized DBR's was also demonstrated, and the issues related to over-oxidation of the mirrors were discussed. Whereas this demonstrates the feasibility of WDM arrays using this technique, further work is needed to extend this approach to 2-D densely packed arrays. For instance, in order to fabricate "pie-shaped" arrays for monolithic coupling to a single multimode fiber, a more complex 2-D oxidation pattern must be used, capable of providing the right wavelength for each element in the array. Device reliability issues related to the presence of thick oxidized layers must also be addressed.

## ACKNOWLEDGMENT

The authors wish to thank Dr. O. Buchinsky, Dr. S.-Y. Hu, and Dr. O. Sjölund for useful discussion.

## REFERENCES

- [1] S. Y. Hu, E. R. Hegblom, and L. A. Coldren, "Multiple-wavelength top-emitting vertical-cavity photonic integrated emitter arrays for direct-coupled wavelength-division multiplexing applications," *Electron. Lett.*, vol. 34, pp. 189–190, 1998.
- [2] S. Y. Hu, J. Ko, and L. A. Coldren, "1.55  $\mu\text{m}$  pie-shaped resonant-cavity photodetector arrays for direct-coupled wavelength demultiplexing applications," *Electron. Lett.*, vol. 33, pp. 1486–1487, 1997.
- [3] W. Yuen, G. S. Li, and C. J. Chang-Hasnain, "Multiple-wavelength vertical-cavity surface-emitting laser arrays with a record wavelength span," *IEEE Photon. Technol. Lett.*, vol. 8, pp. 4–6, 1996.
- [4] H. Saito, I. Ogura, and Y. Sugimoto, "Uniform CW operation of multiple-wavelength vertical-cavity surface-emitting lasers fabricated by mask molecular beam epitaxy," *IEEE Photon. Technol. Lett.*, vol. 8, pp. 1118–1120, 1996.
- [5] T. Wipiejewski, J. Ko, B. J. Thibeault, and L. A. Coldren, "Multiple wavelength vertical-cavity laser array employing molecular beam epitaxy regrowth," *Electron. Lett.*, vol. 32, pp. 340–341, 1996.
- [6] M. H. MacDougall and P. D. Dapkus, "Wavelength shift of selectively oxidized  $\text{Al}_x\text{O}_y$ -AlGaAs-GaAs Distributed Bragg Reflectors," *IEEE Photon. Technol. Lett.*, vol. 9, pp. 884–886, 1997.
- [7] R. L. Naone, E. R. Hegblom, B. J. Thibeault, and L. A. Coldren, "Oxidation of AlGaAs layers for tapered apertures in vertical-cavity lasers," *Electron. Lett.*, vol. 33, pp. 300–302, 1997.
- [8] A. Fiore, Y. A. Akulova, J. Ko, E. H. Hegblom, and L. A. Coldren, "Multiple-wavelength vertical-cavity laser arrays based on postgrowth lateral-vertical oxidation of AlGaAs," *Appl. Phys. Lett.*, vol. 73, pp. 282–284, 1998.
- [9] J. M. Dallesasse, J. N. Holonyak, A. R. Sugg, T. A. Richard, and N. El-Zein, "Hydrolyzation oxidation of AlGaAs-AlAs-GaAs quantum well heterostructures and superlattices," *Appl. Phys. Lett.*, vol. 57, pp. 2844–2846, 1990.
- [10] K. D. Choquette, K. M. Geib, H. C. Chui, B. E. Hammons, H. Q. Hou, and T. J. Drummond, "Selective oxidation of buried AlGaAs versus AlAs layers," *Appl. Phys. Lett.*, vol. 69, pp. 1385–1387, 1996.
- [11] M. H. MacDougall, G. M. Yang, A. E. Bond, C.-K. Lin, D. Tishinin, and P. D. Dapkus, "Electrically-pumped vertical-cavity lasers with  $\text{Al}_x\text{O}_y$ -GaAs reflectors," *IEEE Photon. Technol. Lett.*, vol. 8, pp. 310–312, 1996.
- [12] B. E. Deal and A. S. Grove, "General relationship for the thermal oxidation of silicon," *J. Appl. Phys.*, vol. 36, pp. 3770–3778, 1965.
- [13] E. R. Hegblom, D. I. Babic, B. J. Thibeault, and L. A. Coldren, "Scattering losses from dielectric apertures in vertical-cavity lasers," *IEEE J. Select. Topics Quantum Electron.*, vol. 3, pp. 379–389, 1997.
- [14] O. Blum, C. I. H. Ashby, and H. Q. Hou, "Barrier-layer-thickness control of selective wet oxidation of AlGaAs for embedded optical elements," *Appl. Phys. Lett.*, vol. 70, pp. 2870–2872, 1997.
- [15] D. L. Huffaker, "Dependence of wavelength control on dielectric structure for vertical-cavity surface-emitting lasers," *J. Appl. Phys.*, vol. 81, pp. 1598–1600, 1997.
- [16] M. H. MacDougall, H. Zhao, P. D. Dapkus, M. Ziari, and W. H. Steier, "Wide-bandwidth distributed Bragg reflectors using oxide/GaAs multilayers," *Electron. Lett.*, vol. 30, pp. 1147–1149, 1994.
- [17] K. D. Choquette, private communication.
- [18] A. Fiore, S. Janz, L. Delobel, P. v. d. Meer, P. Bravetti, V. Berger, E. Rosencher, and J. Nagle, "Second-harmonic generation at  $\lambda = 1.6 \mu\text{m}$  in AlGaAs/ $\text{Al}_2\text{O}_3$  waveguides using birefringence phase matching," *Appl. Phys. Lett.*, vol. 72, pp. 1998.
- [19] A. Fiore, V. Berger, E. Rosencher, and J. Nagle, unpublished.

A. Fiore, photograph and biography not available at the time of publication.

Y. A. Akulova, photograph and biography not available at the time of publication.

J. Ko, photograph and biography not available at the time of publication.

E. R. Hegblom, photograph and biography not available at the time of publication.

Larry A. Coldren (S'67-M'72-SM'77-F'82) received the Ph.D. degree in electrical engineering from Stanford University, Stanford, CA, in 1972.

After 13 years in the research area at Bell Laboratories, he was appointed Professor of Electrical and Computer Engineering at the University of California at Santa Barbara (UCSB), in 1984. In 1986, he assumed a joint appointment with Materials and Electrical and Computer Engineering. At UCSB, his efforts included work on novel guided-wave and vertical-cavity modulators and lasers as well as the underlying materials growth and dry-etching technology. He is now investigating the integration of various optoelectronic devices, including optical amplifiers and switches, tunable lasers, receivers, and surface-emitting lasers. He is also heavily involved in new materials growth and fabrication technology essential to the fabrication of such integrated optoelectronic components. He has authored or co-authored more than 300 papers, 3 book chapters, and 1 textbook, and has been active in technical meetings. He is currently Director of the multicampus DARPA-supported Heterogeneous Optoelectronics Technology Center.

## **Appendix 4**

# RF Crosstalk in Multiple-Wavelength Vertical-Cavity Surface-Emitting Laser Arrays

Shigeru Nakagawa, Syn-Yem Hu, Duane Louderback, and Larry A. Coldren

Department of Electrical and Computer Engineering,

University of California

Santa Barbara, CA 93106 USA

Tel: (805) 893-8465

e-mail: nakagawa@engineering.ucsb.edu

## *Abstract*

We present the crosstalk measured in multiple-wavelength vertical-cavity surface-emitting laser (VCSEL) arrays under RF modulation. The array consists of eight bottom-emitting VCSELs arranged with a “pie”-like configuration within a 60- $\mu\text{m}$ -diameter circle with a 3- $\mu\text{m}$  spacing for coupling into a multimode fibre. The crosstalk is investigated by measuring a cross-modulation response of two VCSELs in the array using a monochromator in an optical spectrum analyzer as a receiver. Excess crosstalk is minimized by flip-chip mounting the array and introducing a proper bias condition. The crosstalk observed in the adjacent VCSELs is less than  $-40$  dB at the modulation frequency below 700 MHz and it increases at 20dB/decade above this frequency when both VCSELs are biased at 5.0mA.



### *Index Terms*

Integrated optoelectronics, optical interconnections, laser arrays, vertical-cavity surface-emitting lasers, wavelength-division multiplexing, crosstalk.

## I. INTRODUCTION

The revolution of microprocessors has drastically increased the capability of data processing, and now it gives rise to more severe requirements for computer interconnects and local area networks. The networks have to transmit the data much faster while it should cost less to build, manage, or reconfigure them. Recent advancements in multimode fibre (MMF) links have proven that they are one of the promising candidates to satisfy those demands [1]. These needs now attract increasing interest in wavelength-division-multiplexing (WDM) configurations for the short-haul networks [2], [3]. WDM not only increases data capacity in the networks, but it also makes their construction and reconfiguration easier and cheaper.

We have demonstrated multiple-wavelength vertical-cavity surface-emitting laser (VCSEL) arrays for the WDM transmitters of the MMF networks [4], [5]. The array is designed to be coupled directly into a single MMF without any additional optics, so that in each array eight VCSELs are arranged within a 60- $\mu\text{m}$  circle with a 3- $\mu\text{m}$  spacing. In such a densely-packed array, crosstalk among the VCSELs is an important criteria to be investigated because each VCSEL has to be operated independently in order to increase the aggregate transmission rate of one array or to provide eight independent channels in a WDM network. Three sources of crosstalk have to be considered in the VCSEL arrays: thermal, electrical, and optical sources. The crosstalk in VCSEL arrays with 3- $\mu\text{m}$  pitches has been reported regarding the thermal crosstalk at DC [6], [7]. RF-crosstalk measurement has been performed between VCSELs separated by 1.6 mm in 16-

wavelength VCSEL arrays at a frequency up to 10 GHz [8]. The observed crosstalk is less than -35 dB below 1 GHz, and between -10 and -30 dB at 5GHz. We have investigated the optical as well as thermal crosstalks in our VCSEL arrays in a frequency range from 1 Hz to 10 MHz [9]. The optical crosstalk between the adjacent VCSELs was reduced to less than -20 dB by biasing both of them near or above threshold, while the thermal crosstalk was not found to be significant in our array.

In this paper, we investigate the crosstalk in our multiple-wavelength VCSEL array under higher frequency RF modulation. The array is flip-chip bonded onto a GaAs submount with 50- $\Omega$  coplanar lines. This bonding scheme reduces excess electrical and thermal crosstalk. The crosstalk is investigated by detecting the optical signal from one VCSEL when another VCSEL is modulated with RF signals while the optical signal from the RF-modulated VCSEL is cut off by a monochromator in an optical spectrum analyzer (OSA). Both VCSELs are biased above the threshold in order to minimize the optical crosstalk. The crosstalk measured through the optical signal includes all the possible crosstalks, and this data is the most meaningful in practice.

## II. MEASUREMENT SETUP

The multiple-wavelength VCSEL array [4] is flip-chip bonded on a semi-insulating GaAs submount with 50- $\Omega$  coplanar lines. The GaAs submount is put on an AlN submount which also has 50- $\Omega$  coplanar lines, and their coplanar lines are wire bonded together. The GaAs submount is used to make exchanging the VCSEL arrays easier. The flip-chip bonding eliminates series inductance due to bonding wires between the p-contacts of the

VCSELs and the coplanar lines, and minimizes external electrical crosstalk [10], [11]. It also provides good heat-sinking, which reduces thermal crosstalk. The AlN submount is set on a test fixture which has eight SMA connectors. Figure 1 shows a photograph of the test fixture with the VCSEL array mounted on the submounts.

Figure 2 shows a measurement setup employed in our experiment. The crosstalk measurement is performed by detecting the optical signals from VCSEL A when either VCSEL A or B is modulated. Both VCSELs are biased near or above threshold in order to minimize their optical crosstalk due to modulated spontaneous emission [9], and they are modulated with RF signals from a network analyzer (HP 8510C). The optical signals are collected with a microscope objective lens, and coupled into a MMF. The MMF is connected to an optical spectrum analyzer (HP 70951A), which has the capability to output the optical signal through its monochromator. This provides the optical signal from only VCSEL A and cuts off the other. A lasing-wavelength spacing of the VCSELs is 3.0 nm in average, and with a 0.5-nm bandwidth of the monochromator an isolation between the adjacent wavelengths is better than -50 dB in optical power.

The optical signal coming out of the OSA is detected with a high-speed photoreceiver and an amplifier, and is measured by the network analyzer. The photoreceiver (New Focus 1534) with high conversion gain (250 V/W) and the amplifier (New Focus 1422) with low noise figure (8 dB) are employed, and the measured noise floor of the network analyzer with the photoreceiver and the amplifier connected is equal to or less than -70

dBm below 2 GHz, and  $-100$  dBm above that frequency. Another measurement was performed using a microwave spectrum analyzer (HP 8566B) to increase a dynamic range, especially in the frequency range below 2 GHz, while the network analyzer is still used as an RF signal source. The spectrum analyzer has a variable resolution bandwidth, and the noise floor can be reduced by narrowing it. With its minimum bandwidth, that is 10 Hz,  $-110$  dBm noise floor was achieved in the whole frequency range.

### III. RESULTS

The light output versus current characteristics, lasing spectra, and RF-modulation responses are measured for all the VCSELs in the mounted array. Compared with the results for the unmounted array [4], [5], no significant change is observed for the mounted one. The crosstalk measurement is performed with two VCSELs, which are referred to as VCSELs #4 and #5 in [4]. They are neighboring both in geometry and in wavelength, which are 976 nm and 980 nm for VCSELs #4 and #5, respectively. The threshold current is 2.0 mA for both VCSELs #4 and #5, and the 3-dB bandwidth and resonant frequency are 3.8 GHz and 2.4 GHz for VCSEL #4, and 3.1 GHz and 2.0 GHz for VCSEL #5 at the bias current of 5.0 mA.

Both VCSELs #4 and #5 are biased at 5.0 mA to achieve a 3-dB bandwidth higher than 3.0 GHz. The RF power is +2dBm, which provides the modulation depth of 6%. The wavelength of the monochromator is set to the lasing wavelength of VCSEL #5, which is 979.9 nm. Figure 3(a) shows two modulation responses of VCSEL #5 in the frequency

range from 50 MHz to 6 GHz: one is the response when VCSEL #5 is modulated (labeled as #5), and the other one is that when VCSEL #4 is modulated (labeled as #4). Their difference is the crosstalk from VCSEL #4 to VCSEL #5, which is shown in Figure 3(b). It is less than -40 dB below 700 MHz and it increases with frequency at 20dB/decade above this frequency. It is -25 dB at the 3-dB bandwidth of VCSEL #5. This increase of the crosstalk indicates that the dominant path of the crosstalk is an inductive coupling between the VCLs which is independent of modulation depth [10], [11]. It has been already confirmed that the thermal crosstalk is not significant even without any heat-sinking [9]. The optical crosstalk is reduced to less than -20dB by biasing both VCSELs above threshold [9].

Figure 4 shows the crosstalk measured at the various bias currents of VCSEL #4 when VCSEL #5 is biased at 5mA. The crosstalk is decreased, not increased, by increasing the bias current from 0mA to 1mA. This indicates that the main source of the crosstalk is not the optical coupling between the VCSELs. The increase of the crosstalk with the decrease of the bias current attributes to a decrease of the differential resistance of VCSEL #4, which makes larger part of the current injected into VCSEL #4 flow into VCSEL #5 through the electrical coupling. The measured value is comparable with the crosstalk observed in the array in [8], which has much larger spacing. The VCSELs studied in this paper are isolated with each other by deep trenches etched through the active region, whereas the VCSELs reported in [8] are isolated by proton implantation. The trenches prevent resistive coupling in the densely-packed array. The further reduction of the electrical coupling can be expected by fabricating the VCSEL array on a semi-insulating

substrate and isolating the VCSELs with trenches etched down through n-DBRs, which prevents the VCSELs from coupling to each other through a common n-layer.

#### IV. SUMMARY

We have measured the crosstalk in multiple-wavelength VCSEL arrays with a 3- $\mu$ m spacing which are designed to be coupled into a single MMF. In the densely-packed VCSEL arrays, the crosstalk between the adjacent VCSELs is better than -25 dB up to the 3-dB bandwidth of the VCSELs. This means every VCSEL in each array can be operated independently up to its 3-dB bandwidth in relatively low-dynamic-range applications. Digital communication is one example, and the multiple-wavelength VCSEL array studied here can increase the data capacity or provide other benefits of WDM networks. The dominant source of the crosstalk is resistive coupling below 700MHz and electromagnetic coupling for higher frequency, and it can be further improved by completely isolating the VCSELs using semi-insulating substrates and deep trenches etched through n-DBRs.

#### ACKNOWLEDGEMENTS

This work was supported by the Defense Advanced Research Projects Agency (DARPA) via the Heterogeneous Optoelectronics Technology Center (HOTC). The authors would like to thank Dr. D. Cohen for helpful suggestions on performing the crosstalk measurements.

## REFERENCES

- [1] L. Raddatz, D. Hardacre, I. H. White, R. V. Penty, D. G. Cunningham, M. R. T. Tan and S. Y. Wang, "High bandwidth data transmission in multimode fibre links using subcarrier multiplexing with VCSELs," *Electron Lett.*, vol. 34, pp. 686-688, 1998.
- [2] L. B. Aronson, B. E. Lemoff, L. A. Buckman, and D. W. Dolfi, "Low-cost multimode WDM for local area networks up to 10 Gb/s," *IEEE Photon. Technol. Lett.*, vol. 10, pp. 1489-1491, 1998.
- [3] J. J. Yoo, J. E. Leight, C. Kim, G. Giaretta, W. Yuen, A. E. Willner, and C. J. Chang-Hasnain, "Experimental demonstration of a multihop shuffle network using WDM multiple-plane optical interconnection with VCSEL and MQW/DBR detector arrays," *IEEE Photon. Technol. Lett.*, vol. 10, pp. 1507-1509, 1998.
- [4] S. Y. Hu, J. Ko, and L. A. Coldren, "High-performance densely packed vertical-cavity photonic integrated emitter arrays for direct-coupled WDM applications," *IEEE Photon. Technol. Lett.*, vol. 10, pp. 766-768, 1998.
- [5] S. Y. Hu, S. Z. Zhang, J. Ko, J. E. Bowers, and L. A. Coldren, "1.5 Gbit/s/channel operation of multiple-wavelength vertical-cavity photonic integrated emitter arrays for low-cost multimode WDM local-area networks," *Electron. Lett.*, vol. 34, pp. 768-769, 1998.
- [6] D. L. Huffaker and D. G. Deppe, "Multiwavelength, densely-packed 2 x 2 vertical-cavity surface-emitting laser array fabricated using selective oxidation," *IEEE Photon. Technol. Lett.*, vol. 8, pp. 858-860, 1996.
- [7] C. L. Chua, R. L. Thornton, D. W. Treat, and R. M. Donaldson, "Independently addressable VCSEL arrays on 3- $\mu$ m pitch," *IEEE Photon. Technol. Lett.*, vol. 10, pp. 917-920, 1998.



- [8] M. W. Maeda, C. J. Chang-Hasnain, A. C. Von Lehmen, H. Izadpanah, C. Lin, M. Z. Iqbal, L. Florez, and J. Harbison, "Multigigabit/s operation of 16-wavelength vertical-cavity surface-emitting laser array," *IEEE Photon. Technol. Lett.*, vol. 10, pp. 863-865, 1991.
- [9] S. Y. Hu, J. Ko, O. Sjolund, and L. A. Coldren, "Optical crosstalk in monolithically-integrated multiple-wavelength vertical-cavity laser arrays for multimode WDM local-area networks," *Electron. Lett.*, vol. 34, pp. 676-677, 1998.
- [10] G. Heise, "Crosstalk investigation of laser-diode pairs," *IEEE Photon. Technol. Lett.*, vol. 2, pp. 97-99, 1990.
- [11] T. C. Banwell, A. C. Von Lehmen, and R. R. Cordell, "VCSE laser transmitters for parallel data links," *IEEE J. Quantum Electron.*, vol. 29, pp. 635-644, 1993.

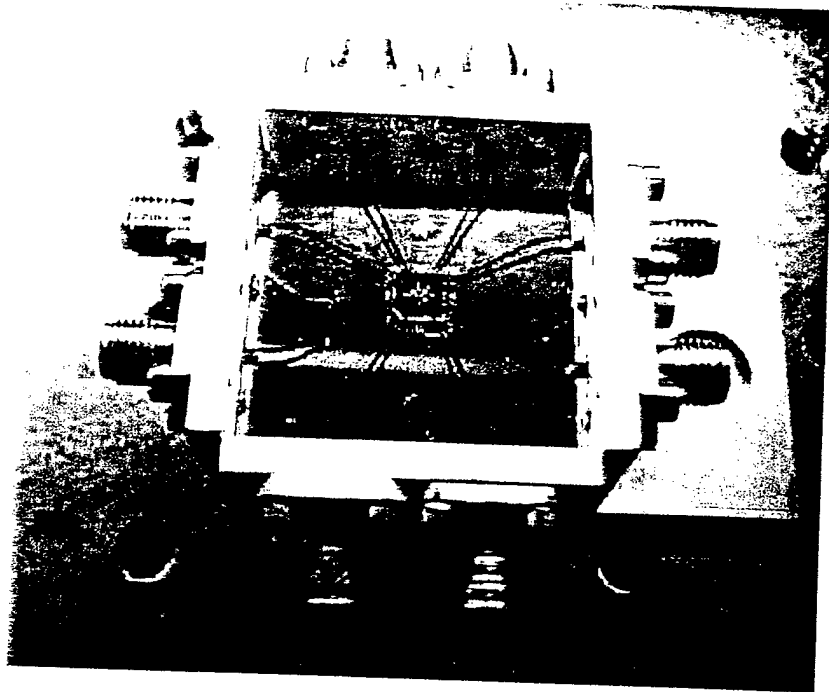
### *Figure captions*

Fig. 1. Photograph of a test fixture for RF crosstalk measurement. In the test fixture, a multiple-wavelength VCSEL array is flip-chip bonded onto a GaAs submount, which is put on an AlN submount.

Fig. 2. Schematic of a RF crosstalk measurement setup. An RF signal from a network analyzer modulates either VCSEL A or VCSEL B, both of which are biased near or above threshold.

Fig. 3. (a) Modulation responses of VCSEL #5 when it is modulated (labeled as #5) and when VCSEL #4 is modulated (labeled as #4). (b) Crosstalk from VCSEL #4 to VCSEL #5 which is derived from the results shown in (a).

Fig. 4. Crosstalk measured as the bias current of VCSEL #4 is 0mA, 1mA, and 5mA. VCSEL #5 is biased at 5mA

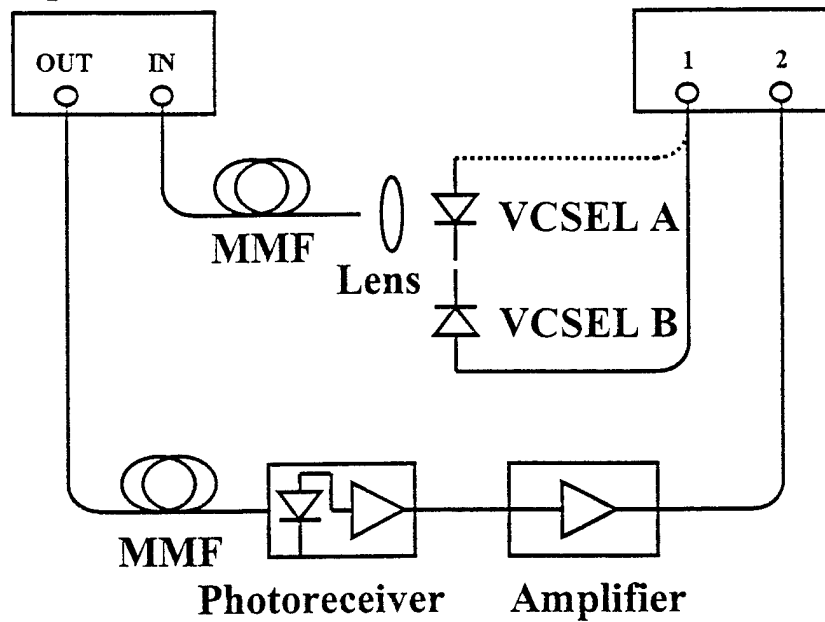


Nakagawa, et. al

Fig. 1

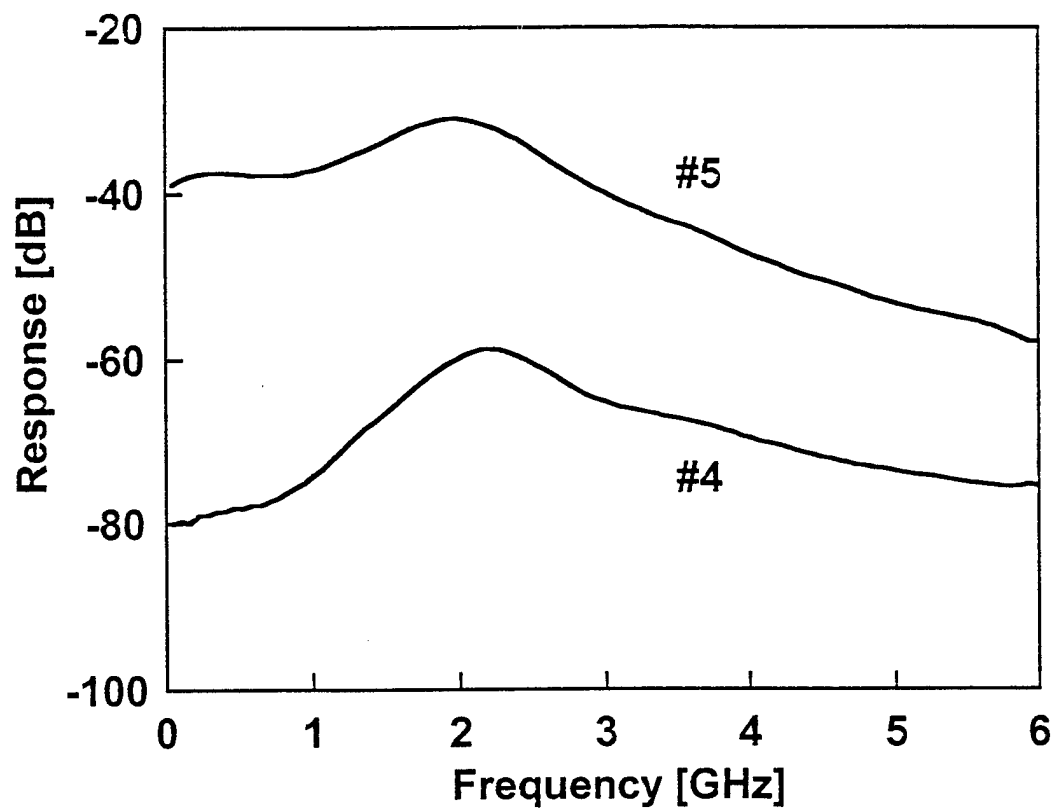
**Optical Spectrum Analyzer**

**Network Analyzer**



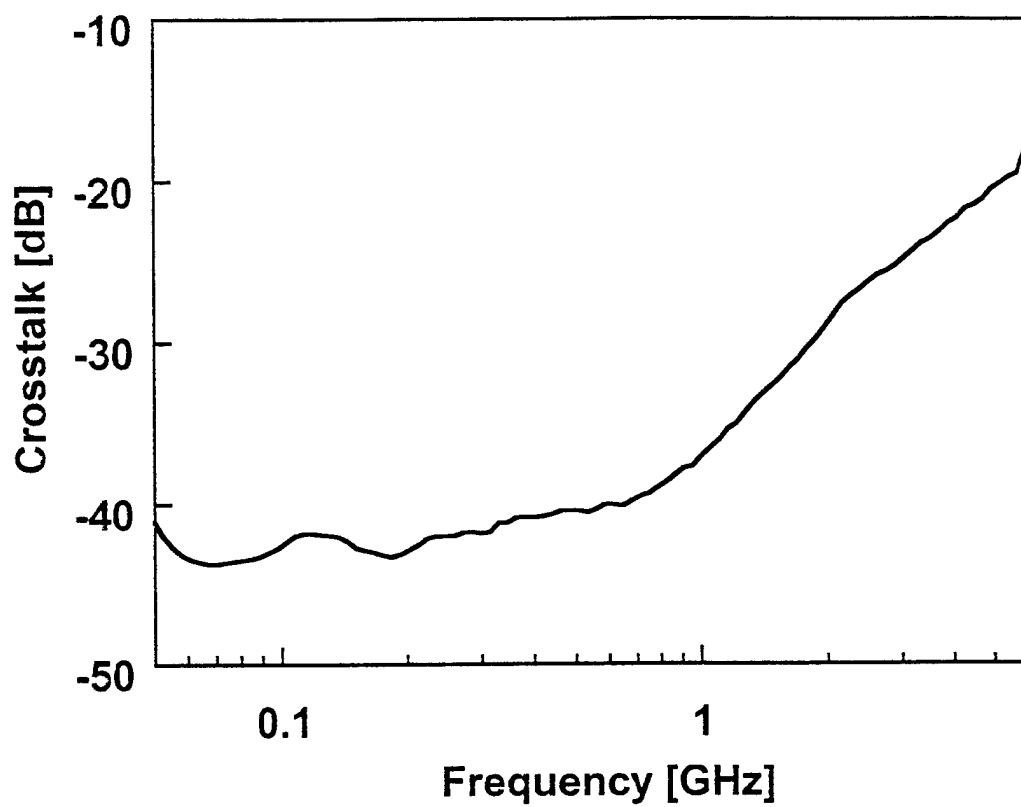
Nakagawa, et. al

**Fig. 2**



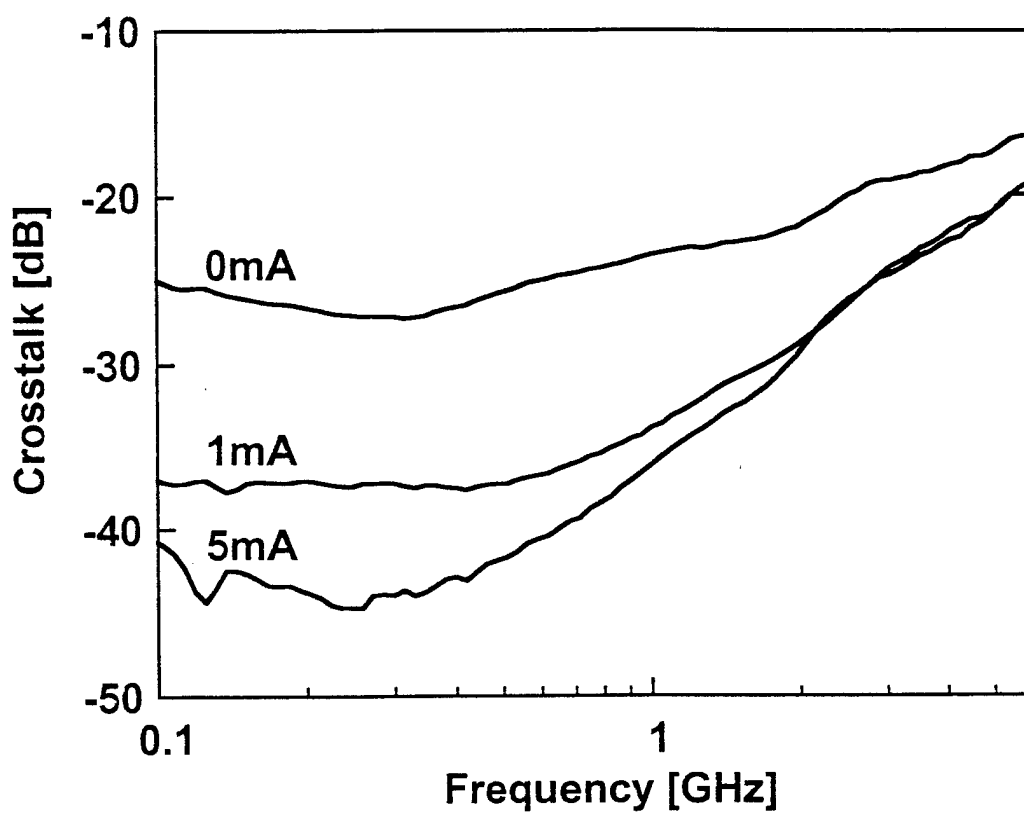
Nakagawa, et. al

Fig. 3(a)



Nakagawa, et. al

Fig. 3(b)



Nakagawa, et. al

Fig. 4